Extending attosecond techniques to X-ray free-electron lasers

Dissertation
zur Erlangung des Doktorgrades
an der Fakultät für Mathematik, Informatik und Naturwissenschaften
Fachbereich Physik
der Universität Hamburg

vorgelegt von

Daniel Charles Haynes

Hamburg

2022

Gutachter/innen der Dissertation:	Prof. Dr. Adrian L. Cavalieri Prof. Dr. Tais Gorkhover
Zusammensetzung der Prüfungskomission:	Prof. Dr. Adrian L. Cavalieri Prof. Dr. Tais Gorkhover Prof. Dr. Franz X. Kärtner Prof. Dr. Ludwig Mathey Dr. Andreas R. Maier
Vorsitzender der Prüfungskomission:	Prof. Dr. Ludwig Mathey
Datum der Disputation:	21.10.2022
Vorsitzender Fach-Promotionsausschuss PHYSIK:	Prof. Dr. Wolfgang J. Parak
Leiter des Fachbereichs PHYSIK:	Prof. Dr. Günter H. W. Sigl
Dekan der Fakultät MIN:	Prof. Dr. Heinrich Graener

Abstract

X-ray free-electron lasers (XFELs) stand at the forefront of cutting-edge research across almost all disciplines of physical science. In the few years for which they have been available, XFEL pulse durations have become increasingly short, and at the time of writing these machines are beginning to access X-ray pulses with durations in the attosecond range (1 attosecond = 10^{-18} s). Meanwhile, the burgeoning field of attosecond metrology has undergone contemporaneous and equally rapid progress this century, including in the measurement and control of attosecond dynamics via attosecond streaking spectroscopy. As XFELs cross the attosecond frontier, this thesis presents a technique termed *self-referenced attosecond streaking*, which unites the unparalleled time resolution of attosecond streaking with the unique and favourable properties of XFELs.

The concepts and principles of XFELs are briefly described, with particular focus given to background information relevant to the developments presented here. The thesis also contains an introduction to attosecond streaking spectroscopy, a powerful time-resolved technique that uses laser fields to induce and record a time-dependent modulation of electrons' momenta. Results of an attosecond streaking investigation of a few-attosecond photoemission delay in neon are presented and discussed. Building upon the core concepts of attosecond streaking, self-referenced streaking is introduced, bringing attosecond precision to XFEL facilities that have traditionally been restricted to femtosecond (1 fs = 10^{-15} s) time resolution. This is achieved by "self-referencing" the data - that is, by examining a single measurement's energy-domain properties relative to those of thousands of other measurements and hence deducing its temporal properties. The final chapters discuss the first successful proof-of-principle experiments employing self-referenced attosecond streaking, including demonstrations of its potential for sub-femtosecond time resolution, and a look ahead to what the future may hold for the technique.

Kurzbeschreibung

X-ray Freie-Elektronen Laser (XFELs) stehen an der Spitze der Forschung in fast allen Disziplinen der physikalischen Wissenschaften. In den wenigen Jahren, seit die ersten XFELs den Betrieb aufgenommen haben, konnte die kürzeste erreichbare Photonenpulsdauer immer weiter verringert werden, sodass zum gegenwärtigen Zeitpunkt bereits Röntgenpulse mit einer Dauer im Attosekundenbereich (1 Attosekunde = 10^{-18} s) möglich sind. In der Zwischenzeit hat das aufkeimende Gebiet der Attosekunden-Metrologie in diesem Jahrhundert ebenso rasche Fortschritte gemacht, unter anderem bei der Messung und Kontrolle der Attosekunden-Dynamik durch Attosekunden-Streaking. Da nun XFELs den für den Bereich der Attosekundenphysik relevant werden, wird in dieser Arbeit eine Technik vorgestellt, die als *self-referenced attosecond streaking* bezeichnet wird und die die unvergleichliche Auflösung des Attosekunden-Streakings mit den einzigartigen und vorteilhaften Eigenschaften von XFELs vereint.

Die Konzepte und Prinzipien von XFELs werden kurz beschrieben, wobei ein besonderer Schwerpunkt auf Hintergrundinformationen gelegt wird, die für die hier vorgestellten Entwicklungen relevant sind. Die Arbeit enthält außerdem eine Einführung zu Attosekunden-Streaking, eine leistungsstarke zeitaufgelöste Technik, die mittels optischer Laserfelder eine zeitabhängige Modulation der Energieverteilung frei fliegender Elektronenpakete bewirkt, wodurch deren zeitliche Struktur in einem Spektrometer messbar wird. Die Ergebnisse einer Studie mittels Attosekunden-Streaking zur Untersuchung einer Photoemissionsverzögerung von wenigen Attosekunden in Neon werden vorgestellt und diskutiert. Aufbauend auf den Kernkonzepten des Attosekunden-Streakings wird das selbstreferenzierte Streaking vorgestellt, das den XFEL-Anlagen, die traditionell auf eine Femtosekunden-Zeitauflösung beschränkt waren (1 Femtosekunde = 10^{-15} s), eine Attosekunden-Präzision verleiht. Erreicht wird dies durch "Selbstreferenzierung" der Daten, d.h. durch die Untersuchung der Eigenschaften einer einzelnen Messung im Energiebereich im Vergleich zu denen tausender anderer Messungen und die daraus resultierende Ableitung ihrer zeitlichen Eigenschaften. In den letzten Kapiteln werden die ersten erfolgreichen Proof-of-Principle-Experimente mit selbstreferenziertem Attosekunden-Streaking erörtert, einschließlich der Demonstration des Potenzials für zeitliche Auflösung im Sub-Femtosekundenbereich, und es wird ein Ausblick auf die Zukunft dieser Technik gegeben.

Contents

Chapter 1

Introduction

In a few short decades, the world of ultrafast science has undergone a period of unprecedented progress. As available laser pulses have become ever shorter, so too has the duration of the processes that can be explored by cutting-edge spectroscopic techniques. The dawn of the 21st century saw pioneering experiments that first probed events on few-femtosecond atomic timescales, and eventually shattered the attosecond frontier to clock the motion of electrons within and outside atoms [1–4].

Much of these pioneering high-time-resolution experiments have utilised high-harmonic generation (HHG) sources, sometimes termed *table-top sources* because of their small size. At the opposite end of the apparatus scale, this era has also seen the realisation of X-ray free-electron lasers (XFELs), starting with the Free-electron Laser in Hamburg (FLASH) in 2005 [5]. XFELs can access much shorter pulse durations than conventional synchrotrons, produce far shorter wavelengths of light than table-top sources, and have much higher brilliance than any other contemporary light source [6–10]. Though their initial impact on the field was dramatic, no less important has been the progress made since then to produce the shortest possible XFEL pulses, enabling ever faster phenomena to be studied. Thanks to these continued advances, it is now possible to perform experiments with XFEL pulses shorter than one femtosecond [10, 11].

However, the attosecond time resolution that might be intimated by these pulse durations has largely been restricted to table-top sources. Despite being tremendously powerful tools, XFELs remain hampered by effects such as timing and phase jitter, which inhibit the most precise time-resolved experiments. These difficulties have historically restricted XFELs to time-resolved

studies on atomic, femtosecond length and time scales, with attosecond-duration electron dynamics just out of reach. Only extremely recently has this changed.

This thesis aims to delineate the journey towards and realisation of feasible, generalised techniques to facilitate attosecond-resolution time-resolved experiments at XFELs. The next chapter will introduce the basic concepts and background of XFEL physics which will contextualise the problems to overcome. Chapter 3 will discuss existing attosecond-resolution techniques, hitherto restricted to table-top HHG sources, and the results of a table-top attosecond streaking experiment that was performed during this thesis. The fourth chapter builds upon this by describing the core restrictions that have thus far forbidden the highest time resolution techniques from application at XFELs, before introducing a new method, *self-referenced attosecond streaking* (SRAS), which can be used to surmount them. The chapter includes the major results that were obtained from the first demonstration of this technique, wherein it was used to measure the Auger-Meitner decay lifetime in neon gas. Chapter 5 will proceed with the final step in the development of SRAS: a full generalisation of the technique that will enable it to be applied to an arbitrarily large array of systems at all XFELs. Finally, Chapter 6 will discuss the expected ramifications of this work and the future of the field.

1.1 Attosecond experiments

Typically, we are limited in the events we can observe by the speed with which we can illuminate them. Pulsed light sources provide a window into dynamics taking place over ultrafast durations and ultrashort distances, and laser pulses attained ever-shorter durations and higher precision throughout the 20th century. From the 1960s onwards, mode-locked laser systems [12–14] provided access to few- and eventually sub-picosecond light pulses. Continued refinement of mode-locked lasers [10, 15] led eventually to few-femtosecond pulses, inaugurating entirely new fields such as femtochemistry [16, 17]; taking place over mere femtoseconds, sub-molecular dynamics were observable for the first time with these ultrashort light pulses. Faster still are intra-atomic electron dynamics, whose observation necessitates attosecond resolution. Only with the advent of HHG sources at the turn of the millennium would attosecond pulses become available, and with that, the field of attoscience was born [10, 18–20].

Much of this thesis will include discussion of an attosecond-resolution methodology that has been used for a multitude of milestone measurements in recent years: attosecond streaking spectroscopy. Chapter 3 will describe this technique, and discuss an experiment applying it to measure few-attosecond delays in photoemission. The subsequent chapters will investigate why attosecond streaking has yet to be widely adopted at XFELs, and discuss the recent advances we have made to make this feasible.

1.2 X-ray science

X-ray radiation has been instrumental in the physical sciences from the moment it was first described by Wilhelm Röntgen in 1895 [21]. From entomology [22] to astronomy [23], X-rays have proven to be a potent tool for studying objects and phenomena invisible to the naked eye.

When performing diffraction experiments, the wavelength of the incident light must be similar to the size of the object being studied [24]. X-rays, therefore, with their few- or sub-nanometre wavelengths, are ideal for the study of atomic and molecular systems. To capture a high-quality image, a large cross-section is desirable, which can be achieved in two ways: increasing the photon flux on the target, or employing a crystalline sample which consists of many molecules arranged periodically. X-ray crystallography is a leading technique by which the structure of proteins [25] and drug molecules [26] can be elucidated.

It is not always possible to form large crystals from biomolecules, warranting increasingly intense X-ray pulses for efficient imaging. In the 20th century, the first three generations of synchrotron sources granted high-brilliance X-ray pulses with which single-crystal imaging is possible [27]. Synchrotron radiation is produced when fast-moving charged particles experience acceleration perpendicular to their direction of motion: synchrotron sources typically produce short and intense X-ray pulses by accelerating electrons around a ring several kilometres in diameter.

The dynamical processes that occur at molecular length scales do so on correspondingly small time scales. However, with their X-ray pulses typically having durations of tens of picoseconds, conventional ring-based synchrotron sources struggle to capture ultrafast processes [28]. To study, for example, a chemical reaction involving a cell and a drug molecule - not just in terms of its reagents and products, but to observe *how* it occurs - calls for temporal

resolution in the femtosecond range. Only then can a "movie" of the dynamics be recorded and observed. In the past two decades, a new type of light source has emerged, one which combines the short wavelength of synchrotrons with vastly increased brilliance and shorter pulse durations: the X-ray free-electron laser (XFEL).

XFELs meet a number of vital criteria for ultrafast science: they produce extreme-brilliance light, they can be tuned over a wide range of wavelengths, and their light pulses can have ultrashort durations. Across physics, chemistry, and beyond, numerous new experiments have become possible in the two decades that XFELs have been available. As will be discussed in later chapters, however, there is potential yet untapped within these machines - especially now that attosecond XFEL pulses are attainable [11]. In spite of techniques such as electro-optic sampling that can improve stability, it is not yet feasible to synchronise an XFEL pulse with an external probe with attosecond precision, which is a prerequisite for attosecond streaking spectroscopy. HHG and XFEL sources therefore complement one another's strengths and weaknesses - with HHG sources being orders of magnitude less expensive and having exclusive access to attosecond resolution, and XFELs able to produce higher-frequency light with far higher brightness.

The next chapter will describe the background and some applications of XFELs, and Chapters 4 and 5 will detail new techniques that unleash their full capability for attosecond research in the future.

Chapter 2

X-ray free-electron lasers

In 1971 John Madey outlined the concept of a free-electron laser (FEL) [29], and he would later be part of the group that built the first operational FEL [30, 31]. Whilst early FELs were restricted to the production of optical wavelengths, the first X-ray FEL would begin operation in Hamburg in 2005 [5], producing 25-fs pulses in the soft X-ray and extreme ultra-violet (XUV) regime, and would herald the arrival of a new era for FELs and the wider field of ultrafast science. By the end of the decade, the Linac Coherent Light Source (LCLS) was operational [32], and few-femtosecond hard X-ray FEL pulses were available for the first time. Time-resolved studies of molecular, atomic, and even electronic dynamics are now within reach.

XFELs are fourth-generation synchrotron sources, employing the synchrotron radiation emitted when relativistic electrons undergo perpendicular acceleration. However, the phenomenon by which XFEL pulses are typically produced, self-amplified spontaneous emission (SASE), is unique to them. It is SASE that gives XFEL pulses their laser-like properties and makes them so distinct from other synchrotron sources.

The remainder of this chapter will outline the principles of SASE XFELs that inform the research results in later chapters, along with some discussion of other related synchrotron sources. This abridged description is necessary and sufficient to expound the research results later in this thesis; more comprehensive explanations and derivations of all the equations presented in this chapter can be found in the 2007 article *"Review of x-ray free-electron laser theory"* [33] and the 2014 book *"Free-Electron Lasers in the Ultraviolet and X-Ray Regime"* [8].

2.1 Synchrotron radiation

Modern synchrotron sources employ insertion devices, usually situated in a straight section of an electron accelerator, to induce X-ray emission from a beam of high-speed electrons. The electron beam consists of short bursts of electrons called *electron bunches*; each bunch might contain up to 10^{10} electrons. The two main types of insertion devices are undulators and wigglers, and they operate using similar principles. Undulators consist of two sets of alternating dipole magnets arranged on opposite sides of the electron beam and with equal poles separated by a fixed distance λ_u, called the undulator period. If we define the y-direction to be that of the undulator poles' magnetic field and the z-direction to be the electrons' direction of motion through the undulator, the magnetic field through which the beam travels is given by

$$B_y(z) = B_0 \sin\left(\frac{2\pi z}{\lambda_u}\right) \tag{2.1}$$

for a peak field B_0. This alternating magnetic field causes the electrons to follow a sinusoidal trajectory and emit synchrotron radiation in a forward-facing cone centred on the electron's instantaneous direction of motion. Figure 2.1 depicts a schematic view of an undulator.

For an electron travelling through the undulator with speed v and corresponding Lorentz factor

$$\gamma = \frac{1}{\sqrt{1 - \left(\frac{v}{c}\right)^2}}, \tag{2.2}$$

where c is the speed of light, the radiation cone's opening angle is approximately equal to

$$\theta_{cone} \approx \frac{1}{\gamma}. \tag{2.3}$$

The central direction in which the radiation is emitted varies up to an angle of around

$$\theta_{max} \approx \frac{K}{\gamma} \tag{2.4}$$

from the z-axis, where K is a dimensionless undulator parameter defined as

$$K = \frac{eB_0\lambda_u}{2\pi m_e c}, \tag{2.5}$$

where e is the electron charge and m_e its mass.

If $K \leq 1$, then $\theta_{max} \leq \theta_{cone}$, so the overall forward-facing radiation comprises many overlapping components, and these interfere with one another. At specific wavelengths, these components interfere constructively. This is the primary difference between a wiggler and an undulator: the latter restricts the bending radius to meet these conditions, and its spectrum consists of narrow peaks of radiation with much higher intensity than the broad spectrum produced by a wiggler.

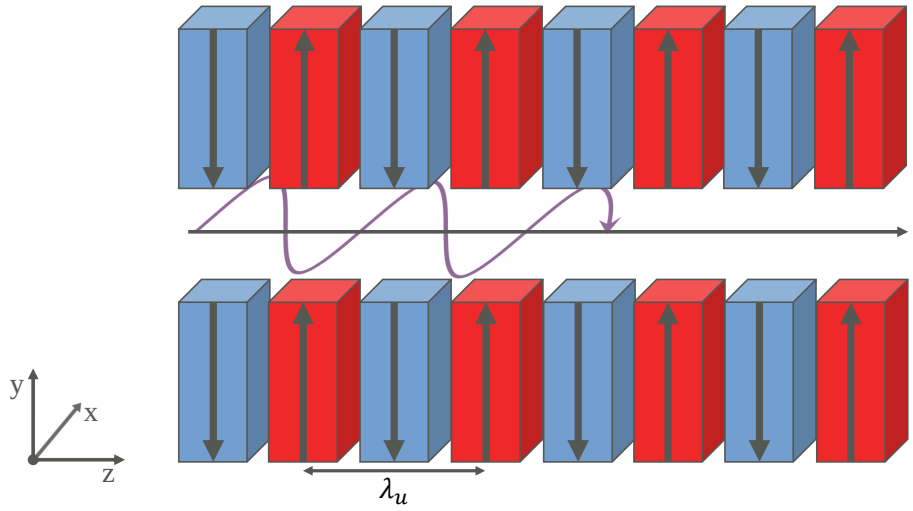

Figure 2.1: **Undulator radiation.** Sketch of an undulator that might be used in a typical XFEL. The purple sine curve represents the trajectory of the relativistic electrons as they pass in the z-direction between the magnets (red and blue). The alternating polarity of the magnets induces a transverse (x-direction) acceleration in the electron bunch. The distance between each two equal poles is the undulator period λ_u.

2.1.1 Relativistic electron beams

The appearance of γ in equations (2.3) and (2.4) indicates that as an electron bunch approaches the speed of light, it will produce synchrotron radiation in a narrower cone, and hence with higher brilliance. In fact, this is not the only radiation parameter that is favourably modified by increasing the electrons' velocity.

In classical physics, an accelerating charged particle emits radiation with a total power [34] of

$$P = \frac{q^2 a^2}{6\pi\varepsilon_0 c^3}, \tag{2.6}$$

where q is its charge and a its acceleration, and ε_0 is the permittivity of free space. Equation (2.6) is known as the Larmor formula, and shows that a larger acceleration will result in a quadratic increase in radiation power. If this formula is adapted to describe the conditions in an undulator - namely, a relativistic particle experiencing acceleration that is orthogonal to its direction of motion - the emitted radiation power is instead proportional to γ^2 [8].

Furthermore, in the frame of reference of a relativistic electron bunch, the undulator magnets are separated not by λ_u but by $\frac{\lambda_u}{\gamma}$ due to Lorentz contraction, reducing the wavelength of the emitted synchrotron radiation. In the laboratory frame, this radiation is further modified by the relativistic Doppler effect, which reduces the wavelength by an additional factor of $\frac{1}{2\gamma}$. Overall, therefore, the wavelength of the emitted radiation is proportional to $\frac{\lambda_u}{2\gamma^2}$ [8]. In summary, electrons accelerated to highly relativistic speeds will emit shorter-wavelength radiation, in a narrower cone, and with higher total power.

2.2 Self-amplified spontaneous emission

Analogous to a conventional laser, a free-electron laser utilises a gain medium and an energy pump; in FELs, the both of these functions are performed by the electron bunch. The early FELs of the 20th century operated in what is termed the *low-gain regime*, because the energy gained on each pass through the undulator is small enough that the field amplitude of the emitted light can be approximated to be constant. In these machines, which produce light in the mid-IR or visible spectrum, mirrors at either end of the undulator confine the radiation therein [31], forming an optical resonator through which multiple electron bunches pass (or a single bunch multiple times). When dealing with wavelengths in the X-ray regime, this is no longer feasible because mirrors with the requisite reflectivity are unavailable. Instead, X-ray FELs employ much longer undulators, with typical lengths on the order of 100 metres, so that all the gain occurs as the electron bunch makes a single

pass through the undulator. During this pass, the intensity of the emitted light field increases exponentially [33]: XFELs operate in the *high-gain regime*. If a low-gain optical FEL can be thought of as a laser oscillator, a high-gain X-ray FEL is a laser amplifier.

As described by Ayvazyan *et al.*, the electron bunches in use at XFELs must have "high peak current, small emittance, small momentum spread and short bunch length" [5]. Electron beams that meet these demands can only be produced by linear accelerators, unlike the circular accelerators employed at conventional synchrotrons. These stringent conditions are essential to facilitate the unique laser-like process by which XFEL pulses are produced: self-amplified spontaneous emission (SASE).

2.2.1 Radiation slippage

As an electron bunch enters an XFEL undulator, it begins to move sinusoidally in the x-plane and emit undulator radiation, as shown in Figure 2.1. Initially, the electrons are randomly distributed within the bunch. As in a conventional laser, the total energy carried by the light must be increased, and this energy will be provided by the electrons. The exact mechanism by which this occurs is thoroughly described by *"Free-Electron Lasers in the Ultraviolet and X-Ray Regime"* [8], with the salient points outlined below.

Each electron has charge $-e$ and some time-dependent velocity $v_x(t)$ in the x-direction, because of its sinusoidal trajectory. Moving within the emitted light's field $E_x(t)$, the electron experiences a Lorentz force in the x-direction given by $F_x = -eE_x(t)$. Energy is transferred to the electron by the field at a rate of

$$\frac{dW}{dt} = -ev_x(t)E_x(t). \tag{2.7}$$

If v_x and E_x have the same sign, $\frac{dW}{dt}$ is negative, representing a transfer from the electron to the light wave: amplification.

This condition will not necessarily be sustainable. Not only is the radiation moving faster than the electrons, but the electrons observe a longer, sinusoidal trajectory. The light wave, therefore, will move forward with respect to the electron bunch within the undulator. This is referred to as *slippage* of the light. In order to maintain the transfer of energy from the electrons to the light field, keeping equation (2.7) negative, the transverse

direction of the electron bunch and the sign of the electric field must change sign simultaneously even as the light slips ahead, as shown in Figure 2.2.

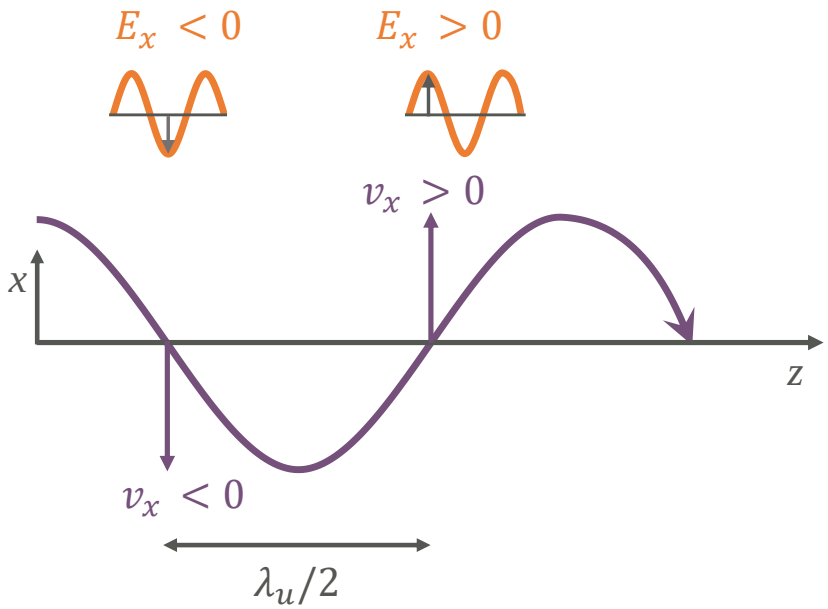

Figure 2.2: **Energy transfer in an XFEL undulator.** Sketch displaying the electron trajectory (purple), which oscillates in the (vertical) x-direction, where the electron bunch has velocity v_x. At two points, half an undulator period apart, the electric field E_x of the emitted light is shown (orange). The signs of v_x and E_x change simultaneously.

In the z-direction, the light has speed c, whilst the electrons' average speed is [8]

$$\bar{v_z} = c\left(1 - \frac{2 + K^2}{4\gamma^2}\right). \tag{2.8}$$

The electrons' sinusoidal trajectory is caused by the alternating undulator magnets; their x-direction reverses each time the bunch traverses half an undulator period λ_u in the z-direction. On average, the time taken to do so is

$$t_e = \frac{\frac{1}{2}\lambda_u}{\bar{v_z}}, \tag{2.9}$$

whilst the time for the light to travel the same distance is

$$t_l = \frac{\frac{1}{2}\lambda_u}{c}. \tag{2.10}$$

Sustained energy transfer demands that the light slips ahead by half of its own wavelength λ_l each time the bunch traverses one undulator half-period, so that v_x and E_x flip sign simultaneously. The light will travel one undulator period in time t_l, and the electrons will arrive at the end of the undulator period after some delay

$$\Delta t = t_e - t_l = \frac{\lambda_u}{2}\left(\frac{1}{\bar{v_z}} - \frac{1}{c}\right). \tag{2.11}$$

If we require that E_x flips sign at the same time as the electrons, the distance travelled by the light during Δt must equal half of its own wavelength λ_l:

$$\Delta t \cdot c = \frac{\lambda_l}{2} \tag{2.12}$$

$$\implies \lambda_l = \lambda_u c\left(\frac{1}{\bar{v_z}} - \frac{1}{c}\right) \tag{2.13}$$

$$\implies \lambda_l = \lambda_u\left(\frac{c - \bar{v_z}}{\bar{v_z}}\right). \tag{2.14}$$

At extremely relativistic electron bunch velocities, the denominator of the right-hand side of equation (2.14) becomes very close to c. Therefore,

$$\lambda_l \approx \lambda_u\left(\frac{c - \bar{v_z}}{c}\right), \tag{2.15}$$

to a good approximation [7, 35]. Inserting $\bar{v_z}$ as defined by equation (2.8) leads to

$$\lambda_l = \lambda_u\left(\frac{c - c\left(1 - \frac{2+K^2}{4\gamma^2}\right)}{c}\right) \tag{2.16}$$

$$\implies \lambda_l = \frac{\lambda_u}{2\gamma^2}\left(1 + \frac{K^2}{2}\right), \tag{2.17}$$

which is the wavelength required for stable, sustained XFEL emission [8, 36]. Equation (2.17) is therefore known as the *resonance condition* of the undulator.

2.2.2 Microbunching

The transfer of energy from the electron bunch to the XFEL, along with the acceleration caused by the light's electric field, affect the momentum of each electron. Continuing through the undulator, these changes in momenta accumulate. Those electrons that gained or lost transverse momentum will have their bending radii increased or decreased, respectively. Overall, the electrons will begin to align into individual smaller clusters at the nodes of the X-ray field, as sketched in Figures 2.3 and 2.4. These smaller clusters, called microbunches, are separated by a distance equal to the wavelength of the X-rays λ_l. This process of microbunching, and the consequent emission of light, is what is meant by self-amplified spontaneous emission.

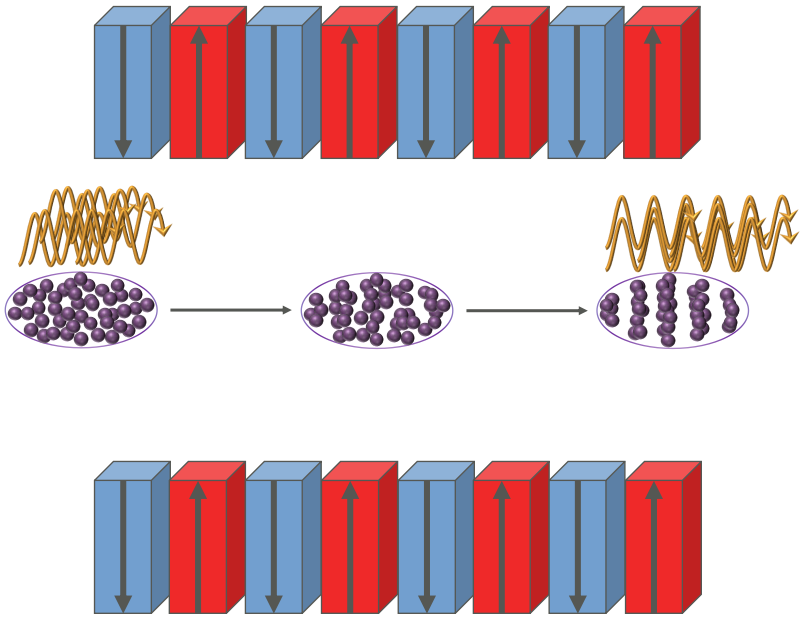

Figure 2.3: **Microbunching in an FEL undulator.** Sketch of the electron bunch (purple spheres, not to scale) at different positions along the undulator. Initially, both the configuration of electrons and the onset of X-ray emission are random, so the X-rays (orange curves) are incoherent. As they progress along the undulator, they self-organise into microbunches separated by the X-ray wavelength λ_l, so that the X-rays emitted by different microbunches interfere constructively.

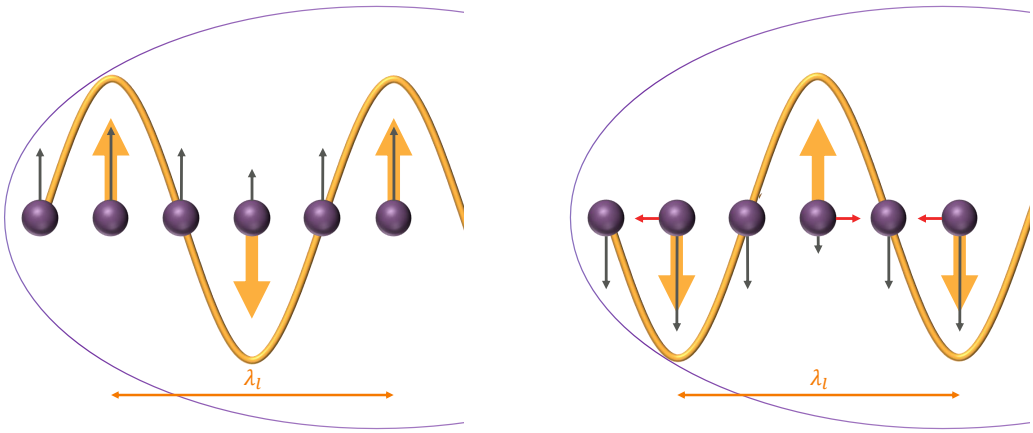

Figure 2.4: **Self-organisation of electrons within the bunch.** Sketch of individual electrons (purple spheres) and their motion relative to one another within the bunch (purple line). The bunch, oscillating in the x (vertical) direction, emits forward-moving synchrotron radiation (orange curve) which changes the momentum of the electrons it overtakes, dispersing them forwards or backwards depending on whether they lose or gain transverse momentum. The left-hand panel represents the early part of the undulator, whilst the right-hand panel shows the bunch after accruing some changes in momentum and beginning to self-organise. The grey arrows represent the instantaneous transverse momentum of each electron and the red arrows represent movement of electrons with respect to one another, whilst the wider orange arrows show the electric field E_x of the X-rays with wavelength λ_l. Every time the bunch traverses half of an undulator period along the z-axis, E_x and the transverse electron velocity v_x change sign simultaneously.

Once SASE is underway in a high-gain XFEL, emitted power increases exponentially along the undulator. The *power gain length* is defined [33, 36] as

$$L_G = \frac{\lambda_u}{4\sqrt{3}\pi\rho}, \tag{2.18}$$

where ρ is the dimensionless Pierce parameter [37]. For a transverse electron beam width (r.m.s) of σ_x and peak electron current I_e, the Pierce parameter equals

$$\rho = \frac{1}{2\gamma}\left(\frac{K\lambda_u}{2\pi\sigma_x}\left[J_0\left(\frac{K^2}{4+2K^2}\right) - J_1\left(\frac{K^2}{4+2K^2}\right)\right]\right)^{\frac{2}{3}}\left(\frac{I_e}{I_A}\right)^{\frac{1}{3}}, \tag{2.19}$$

where J_0 and J_1 are Bessel functions and I_A is the Alfvén current - approximately 17 kA for electrons [33, 36]. The power emitted evolves as a function of distance z along the undulator according to [33]

$$P(z) \propto \exp\left(\frac{z}{L_G}\right). \tag{2.20}$$

This rapid increase in power cannot last indefinitely. Ultimately, the electron beam loses enough energy to the radiation that γ is reduced, equation (2.17) is no longer satisfied, and the FEL pulse energy plateaus [7, 38], as illustrated in Figure 2.5. At this point the FEL is said to be in saturation, since no more power can be drawn from the electron beam. The peak power in saturation is given by [9]

$$P_{sat} \approx \frac{\rho\gamma m_e c^2 I_e}{e}. \tag{2.21}$$

Not all microbunches in the bunch are completely aligned with one another. Since the spontaneously-emitted radiation propagates at a finite speed, the microbunches will not all be moved and aligned by the same wavetrain. Recall from section 2.2.1 that the X-rays slip ahead of the relativistic electron bunch; typically, the light waves will not traverse the entire electron bunch during the journey through the undulator, and so there generally exist several consecutive sets of aligned microbunches within the bunch, with each set emitting coherently. The resultant pulse therefore comprises multiple short 'spikes' both in the XFEL spectrum and the time domain [8, 39, 40].

SASE XFEL pulses have good spatial coherence and limited temporal coherence: the coherence length L_c is determined by the length of each wavetrain and the corresponding coherence time $\tau_c = \frac{L_c}{c}$ is given by

$$\tau_c \approx \frac{1}{\rho\,\omega_l}, \tag{2.22}$$

where ω_l is the angular frequency of the XFEL radiation [7, 35].

The intensity of radiation produced by a conventional undulator scales approximately proportionally to the number of electrons N in the bunch -

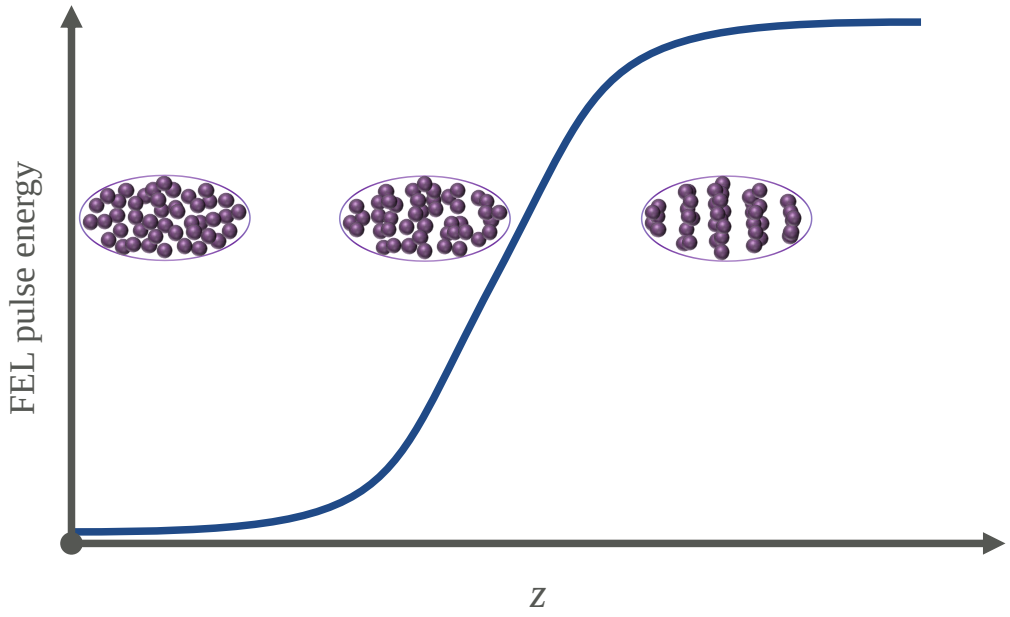

Figure 2.5: **Energy gain in an XFEL undulator.** Sketch of the evolution of XFEL pulse energy (blue curve) as an electron bunch travels in the z-direction through the undulator. The logarithmic y-axis indicates the pulse energy, which initially increases exponentially before reaching a plateau as the FEL enters saturation. The electron bunch is sketched in purple at three positions along the undulator, showing increasing microbunching from left to right.

the radiation emitted by each electron is given by equation (2.6), and the total is proportional to Ne^2. Conversely, in a SASE XFEL, each spike is emitted by many coherently-contributing microbunches that can be treated as single, highly-charged particles. Consequently, the total emitted power satisfies

$$P_{SASE} \propto \frac{N^2}{n_S}, \tag{2.23}$$

where n_S is the number of coherent spikes that make up the XFEL pulse. For a typical XFEL, the coherence time τ_c is of a similar order of magnitude to the pulse duration, such that $n_s \ll N$, and therefore P_{SASE} is approximately

proportional to N^2. Considering that the number of electrons in the entire bunch N is typically on the order of hundreds of millions, it is clear how the XFEL intensity so drastically eclipses that of other synchrotron sources [9].

2.3 XFEL applications

SASE XFELs produce extreme-brilliance, partially-coherent X-ray pulses with several orders of magnitude higher brightness than other X-ray sources [9]. When compared to conventional undulator sources, XFELs also provide greater flexibility, with wavelengths tunable by modifying the electron bunch velocity according to equation (2.17), so XFEL photon energies extend well into the hard X-ray spectrum [32, 41]. The uniquely high intensity these machines provide facilitates the creation and exploitation of highly-excited states of matter that are dependent upon multiple-photon ionisation. For example, double-core-hole spectroscopy [42–48] takes advantage of the increased spectral sensitivity exhibited by doubly-ionised molecules, uncovering deeper insights into molecular structures.

XFEL pulse durations can now be below one femtosecond [11], opening other unique avenues for research. A well-known example is the *"diffraction-before-destruction"* concept [49], which exploits the fact that XFELs have not only the wavelength and brightness to probe small biomolecular samples, but also short enough pulses that structural information can be extracted before the radiation destroys the sample.

In addition to unravelling static molecular structures, XFELs are powerful tools for time-resolved experiments. Some studies have employed pump-probe spectroscopy - using external laser pulses to initiate dynamical processes that are then probed by the XFEL pulse - to make measurements with time resolution on the hundred-femtosecond scale [50, 51]. Similar techniques have also been applied to pulse characterisation at FELs, with some measurements attaining even higher precision [52, 53]. Yet, as will be discussed in detail in the forthcoming chapters, there are innate obstacles to making time-resolved measurements at XFELs with the attosecond resolution available to HHG sources.

Chapter 3

Attosecond streaking spectroscopy

Electron streaking is a technique that has been used for decades across the physical sciences to make time-resolved measurements with high precision. Fundamentally, all streaking experiments involve mapping between temporal properties and spatial variations; by measuring the latter, the former can be calculated. This mapping between time and space can be achieved by modulating electrons' momenta in the continuum. Conventional streak cameras [54] employ photocathodes, which emit electrons when struck by a light pulse. These electrons can be accelerated using a capacitor with a time-dependent electric voltage, and their final positions recorded using a phosphor screen. They are accelerated in a direction perpendicular to their direction of motion, so that they are spread out transversely when they hit the detector - painting the eponymous 'streak' across the screen. The initial burst of electron emission has a temporal profile matching that of the incident light pulse, and this profile can be deduced from the time-dependent spatial distortion induced by the voltage.

Conventional streaking devices can attain time resolution as fine as hundreds of femtoseconds [55], yet an attosecond streaking experiment demands significantly higher precision. This can be achieved by inducing photoemission in a sample with an attosecond light pulse, and then accelerating the photoelectrons with the electric field of a longer optical or infrared laser pulse, which has a higher frequency and hence higher temporal sensitivity than can be achieved with capacitors. Unlike in conventional streaking, attosecond streaking imparts a change in the electrons' momenta that is parallel to their

direction of motion, increasing or decreasing the speed and kinetic energy with which they enter the detector. The typical experimental procedure involves varying the relative arrival time between the two pulses - the pump-probe delay - and measuring the resultant distribution of the electrons' final kinetic energies. As a result of interaction with the streaking field, this distribution will change as a function of delay, and it is these changes that will provide clues to the temporal properties of the system.

This technique, dubbed the attosecond streak camera, was presented in 2002 [1], and it has since been used for myriad measurements of ultrafast processes, including the oscillation of light waves [56], duration of core-hole decay lifetimes [2], and even the photoelectric effect itself [4, 57]. It remains one of the most precise techniques currently available for time-resolved measurements, granting time resolution below 100 attoseconds [1].

3.1 Foundations of attosecond streaking

Attosecond experiments are extremely challenging, placing many demands upon the experimental apparatus. Typical attosecond streaking experiments employ a relatively low-intensity ionising pump pulse, meaning that the signal for a single pump-probe pair is weak, and measurements must be repeated at each pump-probe delay many times so that a strong average signal can be obtained. It is therefore paramount that the streaking conditions can be strictly regulated, so that many individual measurements can all be made under identical conditions.

Controlling the relative arrival time of the two light pulses is essential so that dynamic effects can be precisely measured and distinguished from timing fluctuations in the apparatus; the streaking laser phase, meanwhile, must also be fixed, so that the probe is consistent for each of the many streaking events in an experiment. If these two parameters can be regulated with sufficient precision, we can use attosecond streaking spectroscopy to measure ultrafast dynamics directly in the time domain.

3.1.1 Carrier-envelope phase

If we are to map between kinetic energy and time t, we must be able to relate each pump-probe delay step to a unique part of the streaking pulse. The pulse's electric field strength $E(t)$ is proportional to a sinusoidally-oscillating

term with a characteristic angular frequency ω. However, there is an additional term ϕ_{CEP} in the argument of the sine function, so that

$$E(t) = E_0(t)\cos(\omega t + \phi_{CEP}), \tag{3.1}$$

where $E_0(t)$ is the time-dependent amplitude of the pulse envelope - typically a Gaussian curve. The extra term ϕ_{CEP} is the phase of the streaking field with respect to its pulse envelope: the *carrier-envelope phase* (CEP). In general, any two pulses produced by a laser will have different values of ϕ_{CEP}, as illustrated in Figure 3.1. When the laser pulses have a duration of just a few cycles, an unstable CEP can cause the electric field to differ significantly for each laser pulse, making the pulses an inconsistent and unsuitable probe of ultrashort dynamics.

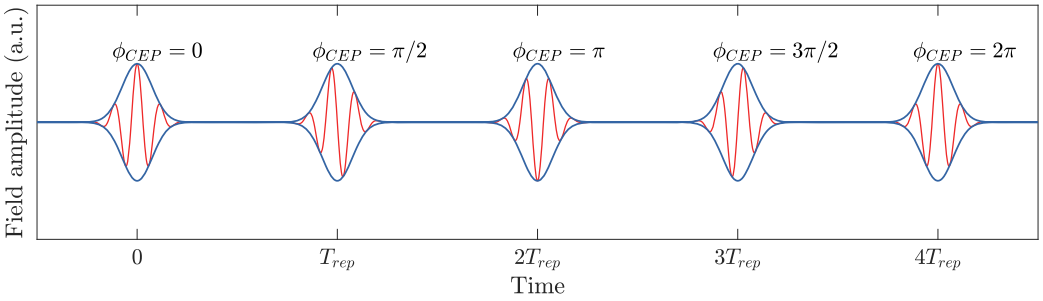

Figure 3.1: **Carrier envelope phase.** Sketch of the amplitude (blue curve) and electric field strength (red curve) of a train of laser pulses with a laser repetition rate $f_{rep} = \frac{1}{T_{rep}}$. The CEP of each pulse is $\pi/2$ radians larger than the previous pulse, meaning that the CEP frequency $f_{CEP} = \frac{f_{rep}}{4}$.

CEP-stable laser pulses became available at the start of the millennium [58–62], and paved the way for modern attosecond streaking spectroscopy. The CEP can be stabilised using an f-to-2f interferometer scheme: with an octave-spanning spectrum, the low-frequency region can be frequency-doubled and compared to the highest frequencies, and the beat note between them measured. This beat note is equal to the CEP frequency f_{CEP}, which is the fractional phase change from one pulse to the next; if f_{CEP} equals half the laser's repetition rate, the CEP is shifting by half a cycle (π radians) between consecutive pulses. Once f_{CEP} is known, only the pulses with the same CEP can be selected for amplification. The electric field is therefore

kept consistent across the time domain and can be used as a high-resolution temporal probe.

3.1.2 High-harmonic generation

In attosecond streaking spectroscopy, two light pulses are used - one ultrashort pulse to induce photoemission in the target, and the longer CEP-stable pulse which accelerates those electrons after their emission. A typical laboratory set-up might employ attosecond XUV pulses alongside optical or mid-infrared (MIR) streaking pulses. It is essential that the two light pulses be well synchronised; the pump pulse arrival time must be precisely controlled in order to probe the system at each desired time delay.

Ultrashort XUV pulses can be reliably produced by HHG, which is a powerful method of nonlinear frequency conversion: a phenomenon by which light can be converted to a different wavelength. In the case of HHG, the output light comprises high harmonics of the input light pulse.

HHG in a noble gas medium can be understood by means of a semi-classical three-step model [63], which is sketched in Figure 3.2. In the first step, the extreme intensity of the laser field modifies the potential well in which an electron is trapped, making it more likely to tunnel through the barrier and escape. Tunnel ionisation is a quantum-mechanical effect, but the electron is treated as a classical particle after tunnelling in this model. Initially stationary in the continuum, the free electron is accelerated away from its parent ion by the pulse's oscillating electric field $E(t)$. When the sign of this field changes, so too does the direction in which the electron is accelerated, bringing it back to the ion. If the electron and ion recombine, the electron must release the excess energy it acquired accelerating in the laser field, which it does via emission of high-energy XUV photons.

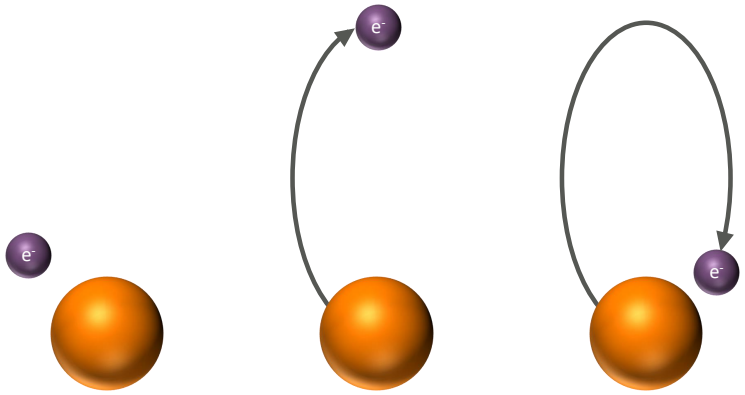

(a) (b) (c)

Figure 3.2: **Three-step model of high-harmonic generation.** Sketch of the semi-classical three-step model of HHG, with the parent ion (orange) and electron (purple) shown at three times from earliest (left) to latest (right). (a) An electron tunnels through the potential barrier and is ejected from the atom due to the driving laser pulse. (b) The electron is accelerated by the laser field and follows a trajectory (grey arrow) that is dependent upon its time of emission. (c) When the field changes sign, the electron is drawn back towards the parent ion and recombines therewith, emitting high harmonics of the driving laser field as a result.

Unlike harmonic generation, which is currently only feasible up to fourth harmonics [64, 65], HHG can produce light with many times the photon energy of the input pulse. The energy of the photon produced by a specific three-step electron recombination event depends on the kinetic energy acquired by the electron while it is accelerated by the driving laser field. This in turn is dependent on the moment at which the electron is stripped from the atom, which determines the evolution of the oscillating laser field while the electron is in the continuum. Since many electron recombination and HHG events will happen throughout the duration of the laser pulse, a wide range of output photon energies are produced by each pulse. A selection of possible electron trajectories are shown in Figure 3.3a and 3.3b. Electrons emitted at different times with respect to the driving laser pulse will follow

different trajectories, and might not return to the parent ion at all.

The fundamental limit on the photon energy that can be produced is determined by the maximum kinetic energy that the electron can gain before returning to its parent ion. The intensity of the harmonics produced by HHG rapidly falls for the first few orders before reaching a plateau that spans a wide spectral range, and then rapidly falls to zero at photon energies around a characteristic *cut-off energy* E_{cutoff} [61, 66, 67]. The cut-off energy is given by

$$E_{cutoff} <= 3.17U_P + E_I, \tag{3.2}$$

where

$$U_p = \frac{e^2 E_0^2}{4m_e\omega^2} \tag{3.3}$$

is the *ponderomotive potential* of the laser field with amplitude $E_0(t)$, and E_I is the ionisation energy, sometimes called the ionisation potential. Also referred to as ponderomotive energy, U_p is equal to the average kinetic energy gained by a free electron in an electric field during one cycle. The maximum energy gain of $3.17U_p$ occurs when electrons recombine while the oscillating field is close to zero; these points in time are referred to as *zero-crossings* of the field.

Figure 3.3c shows, for cases where the electron does recombine, the relationship between its final kinetic energy and its emission time. The electron trajectory that results in the highest kinetic energy of $3.17U_p$ is highlighted in purple in Figure 3.3a.

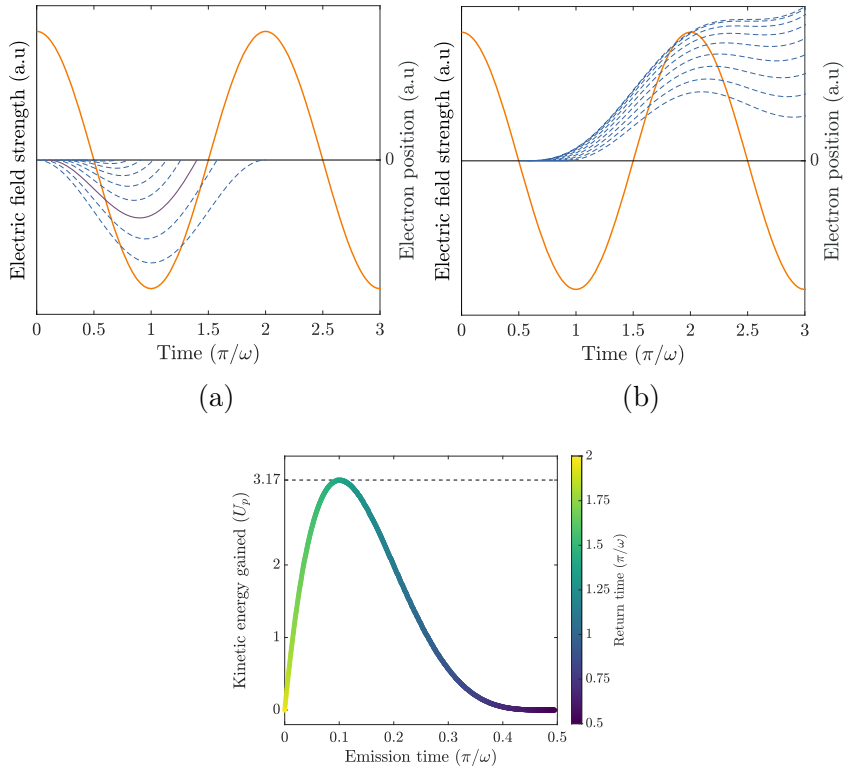

Figure 3.3: **High-harmonic generation.** (a) and (b): Trajectories of electrons (blue dashed lines) emitted at different phases of the optical drive laser (orange line). The purple line shows the trajectory that results in the emission of harmonics up to E_{cutoff}. (c): Kinetic energy gained by an electron before returning to its parent ion, as a function of emission time. The colourmap shows corresponding return time, and the black dashed line shows the maximum possible kinetic energy gain, achieved when an electron recombines near a zero-crossing of the electric field.

In the case of a few- or sub-cycle laser pulse, one might infer from Figure 3.3 that the timing of a particular electron trajectory - and hence of the emitted light - is highly dependent on the CEP of the driving laser pulse. Indeed, with a single-cycle CEP-stable driving pulse, the CEP can be set so that there is only one zero-crossing recombination time that results in emission of harmonics up to E_{cutoff}, and the highest-energy part of the XUV

spectrum corresponds to a single region in time [61]. Being highly localised in time, this emitted light's energy spectrum is spread over a continuous range of frequencies [67]. If we can 'slice' out a small part of the frequency spectrum near E_{cutoff} - with an appropriate optic, for example - the resultant XUV pulse will have an ultrashort duration, consisting as it does of light emitted in a very short duration near a zero-crossing of the laser field. This concept will be revisited later, in section 3.2.1.2, and will allow us to consistently produce attosecond XUV pulses.

Another of the great advantages of HHG is that the same laser used to induce HHG and produce the XUV pulses can be used to streak the photoelectrons ejected by the XUV light. Consequently, such apparatuses have near-flawless synchronisation between the pair of pulses as they approach the target. An adjustable delay stage placed between the HHG chamber and sample increases the path length of one of the two pulses, and can be used to set the relative arrival times as desired.

3.1.3 Mathematical treatment of streaking spectroscopy

The following description of electron acceleration in streaking experiments is based on a derivation first presented by Itatini *et al.* [1] and will be used to relate the electrons' final kinetic energies, which are a measurable quantity, to the temporal properties of the system.

When the XUV pulse hits the sample, it induces photoemission. The emitted photoelectron has an initial kinetic energy

$$W_0 = \hbar\omega_X - E_I, \tag{3.4}$$

where ω_X is the angular frequency of the XUV light, E_I is the ionisation energy as in section 3.1.2, and $\hbar = \frac{h}{2\pi}$ is the reduced Planck constant. As in section 3.1.1, the electric field of the linearly polarised streaking laser pulse is given by

$$E_L(t) = E_0(t)\cos(\omega_L t + \phi_{CEP}), \tag{3.5}$$

where t represents time, $E_0(t)$ the time-dependent amplitude of the streaking pulse, and ω_L the laser's angular frequency. The vector potential of the field $A_L(t)$ satisfies $E_L(t) = -\frac{\partial A}{\partial t}$ and is given by

$$A_L(t) = \frac{-E_0(t)}{\omega_L}\sin(\omega_L t + \phi_{CEP}). \tag{3.6}$$

After the laser pulse ends, the electron is left with a final velocity

$$\vec{v}_f = \vec{v}_0 + \frac{e}{m_e}\vec{A}(t_i), \tag{3.7}$$

where $\vec{v}_0$ is its initial velocity at the instant of ionisation t_i.

For a linearly polarised laser field with ponderomotive potential U_p, the final kinetic energy of the electron is given by

$$K = W_0 + 2U_P \cos(2\theta)\sin^2(\phi_i) \pm \alpha\sqrt{8W_0U_p}\cos(\theta)\sin(\phi_i), \tag{3.8}$$

where $\phi_i = \omega_L t_i + \phi_{CEP}$ is the phase of the streaking laser at the time t_i, θ is the angle from the x-axis at which the electrons are being detected, and $\alpha = \sqrt{1 - \left(\frac{2U_P}{W_0}\right)\sin^2(\theta)\sin^2(\phi_i)}$ is a correction term that can be set to 1 under the typical conditions that $U_P \ll W_0$.

The final term in equation (3.8) is positive except in the case that $U_P > \frac{W_0}{2}$, where some electrons may be accelerated such that their final direction is opposite to $\vec{v}_0$, resulting in an additional peak in the electron energy spectrum.

Under the condition that $U_P \ll W_0$, we can neglect the second term in equation (3.8), leaving us with the approximation

$$K \approx W_0 + \sqrt{8W_0U_p}\cos(\theta)\sin(\phi_i). \tag{3.9}$$

Restricting our consideration to electrons travelling in the x-direction such that $\theta = 0$, we are left with a second term in equation (3.9) that is proportional to the streaking laser's vector potential in equation (3.6). Recalling the definition of the ponderomotive potential

$$U_p = \frac{e^2E_0^2}{4m_e\omega^2}$$

from equation (3.3) in section 3.1.2, the change $\Delta K(t_i) = K - W_0$ in the kinetic energy of an electron emitted at time t_i can therefore be expressed as

$$\Delta K(t_i) \approx -\sqrt{\frac{2W_0}{m_e}}eA(t_i), \tag{3.10}$$

so that

$$\Delta K(t_i) \propto -A(t_i). \tag{3.11}$$

Understanding that the magnitude of the change in kinetic energy felt by an electron is proportional to the streaking field's vector potential and field amplitude at the time of ionisation is crucial for the execution and interpretation of attosecond streaking experiments. Provided that the dynamics of interest occur in less than half of a streaking laser period, each ΔK can correspond to a single moment in time. This allows the measured kinetic energies to be directly mapped to time-domain events and processes within the system being studied, and will be instrumental in the interpretation of the data presented in sections 3.2, 4.3, and 5.2.

3.1.4 Energy calibration

In order to analyse the data from attosecond streaking experiments, the change in kinetic energy felt by the electrons must be known. Electron time-of-flight (TOF) detectors measure the electrons' arrival times, which can be used to infer their kinetic energy. A TOF consists of a drift tube, typically a few tens of millimetres long, with a micro-channel plate (MCP) at one end. An MCP acts as an electron multiplier, producing millions of electrons for each one that hits it [68], and thereby generating a signal. In an attosecond streaking experiment, synchronising the signal with the repetition rate of the laser enables the time a photoelectron takes to reach the MCP to be measured with nano- or picosecond precision [68]. This flight time - typically tens or hundreds of nanoseconds - is dependent on the electrons' kinetic energy, which itself depends upon their initial momentum and the acceleration they experienced due to the streaking laser, as described in section 3.1.3. A schematic diagram of a TOF is shown in Figure 3.4.

The *working distance* d_w of the TOF is defined as the space over which the electron travels between the sample and the entrance to the TOF. A typical working distance might be a few tens of millimetres. The difference in arrival time between two electrons with different, known kinetic energies - such as two types of Auger-Meitner electron - can be used to precisely calculate the working distance.

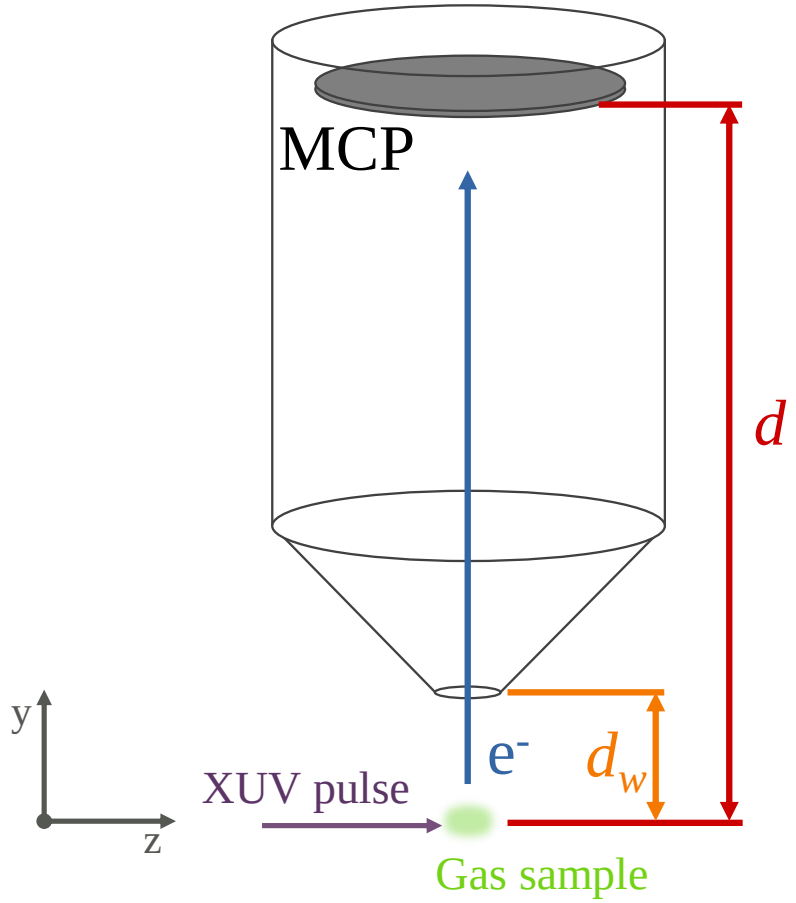

Figure 3.4: **Time-of-flight detector.** Sketch of the basic concept and components of an electron time-of-flight (TOF) detector used in an attosecond streaking experiment. An XUV pulse (purple arrow) is focused into a suitable target, such as a noble gas (green). Photoelectrons (blue) are emitted and travel a distance d through the TOF drift tube until they hit the MCP, generating a signal that can be used to infer their kinetic energy.

If the working distance is known, the distribution of electron flight times t can be mapped directly to a distribution of kinetic energies. Let the former be $f(t)$ and the latter be $g(E)$. According to classical mechanics,

$$E = \frac{m_e d_w^2}{2t^2}, \tag{3.12}$$

where m_e is the mass of the electron. This simple formula allows each time-domain value to be associated with a corresponding value in the energy domain. However, equation (3.12) alone is not sufficient to calculate the energy distribution of electrons $g(E)$ from $f(t)$.

In the time domain, the data are collected at evenly-separated intervals - typically a few nanoseconds - but it is clear from equation (3.12) that these fixed-width temporal bins will not be mapped to evenly-spaced spectral intervals. Nevertheless, the total number of electrons recorded over some range ΔE corresponding to the temporal range Δt must be conserved. Formally,

$$\int_{t_0}^{t_1} f(t)dt = \int_{E_0}^{E_1} g(E)dE, \tag{3.13}$$

where E_i and t_i are related by equation (3.12). Equation (3.13) implies that

$$g(E) = f(t)\left|\frac{dt}{dE}\right|. \tag{3.14}$$

Using equation (3.12), we find that the magnitude of the derivative

$$\left|\frac{dt}{dE}\right| = \frac{t^3}{m_e d^2}, \tag{3.15}$$

and thus we can scale the energy-domain spectrum appropriately using equation (3.14). This procedure allows recorded time-of-flight spectra to be swiftly converted to energy-domain spectra. Changes in the energy spectrum as a function of pump-probe delay will grant insight into the atomic and electronic dynamics at play.

3.2 Measuring photoemission delays in neon

With the extreme time resolution provided by attosecond streaking spectroscopy, it is possible to witness and probe events which occur on electronic - sub-femtosecond - timescales [1, 3, 4, 18, 69, 70]. One such process is utterly fundamental to modern ultrafast science: the photoelectric effect [71]. The emission of photoelectrons due to interaction with light pulses underpins all modern X-ray spectroscopic techniques, and happens on a few-attosecond timescale so short that it can often be approximated to be instantaneous. Now, as XUV pulse durations and corresponding time resolutions approach

the few-attosecond range, the duration over which photoemission takes place is within our grasp. Measuring this delay is now not only possible, but may be imperative, because streaking measurements of other attosecond processes must account for systematic delays in photoemission itself. Attosecond streaking spectroscopy cannot directly measure the time between the impact of a light pulse and emission of a photoelectron; rather, it can be used to measure differences in emission times of electrons with different binding energies, and theoretical models can be used to infer the corresponding absolute delay in photoemission [57, 72–74].

In the first application of attosecond streaking spectroscopy to the study of solid-state samples, Cavalieri *et al.* [4] measured a 100-attosecond delay between the emission of conduction band and 4f electrons in crystalline tungsten. Another powerful technique known as the attoclock - using a single, circularly-polarised light pulse as a pump and probe - has been used to study tunnelling ionisation times in helium [75, 76] and argon [77], finding delays on the order of tens of attoseconds. The RABBIT (reconstruction of attosecond beating by interference of two-photon transitions) technique, which employs a train of consecutive attosecond HHG pulses, is another route to measuring photoemission delays that has been applied in various systems [78–80].

The first direct measurements of photoemission delays in a gas-phase sample were published in 2010 [57]. Applying attosecond streaking spectroscopy with a neon gas sample and a 106-eV XUV pump, this group examined the time that elapses between emission of 2p and 2s electrons; they uncovered a delay of 21 attoseconds. However, it has not been possible to reconcile this measurement with established theoretical models, which have generally predicted 2s-2p delays as short as 5 or 10 attoseconds at that photon energy [57, 81–85]. Since this pioneering result, other attosecond streaking experiments have measured photoemission delays in helium, which is more amenable to theoretical modelling owing to a much simpler electronic structure [72–74, 86].

In 2017, another experiment used RABBIT to measure the 2s-2p delay in neon for ionising photon energies between 65 and 100 eV, and their results showed good agreement with theoretical predictions [80]. This group posited that the discrepancy between theory and experiment observed previously may have been due to the 2010 experiment not accounting for *shake-up processes*: as they are emitted, photoelectrons can lose some energy to other electrons in their parent ion, which accordingly move to different orbitals [87]. The decelerated photoelectrons form lower-energy 'satellite' peaks in the re-

covered spectrum, which can obfuscate the measurement of photoemission delays. The 2017 experiment had access to higher spectral resolution and was able to distinguish satellite peaks from the standard 2s photoemission peak, showing that the time delay between shake-up and 2p photoemission is longer than that between 2s and 2p emission. However, some theoretical work has found that accounting for these shake-up effects leads to an even larger discrepancy with the 2010 experiment [85].

Further research into the neon 2s-2p delay, in particular its dependence on photon energy, is becoming increasingly important as available pulse durations continue to improve, so that photoemission delays can be accounted for in all attosecond experiments. Additional measurements may also help to establish greater agreement between theory and experiment. The remainder of this chapter will detail the results from a new investigation into photoemission delays.

3.2.1 Experimental apparatus

The laboratory used in the present work is equipped with a state-of-the-art attosecond streaking setup, and is specifically designed to make measurements of few-attosecond dynamics. Its design and operation are described in this section.

3.2.1.1 Optical-laser-driven high-harmonic generation

The generation of isolated attosecond XUV pulses via HHG places stringent requirements on the properties of the laser pulse used to generate them; it must be sufficiently intense and have a few-femtosecond duration. These laser pulses are produced as follows.

Firstly, CEP-stable oscillator pulses are used to seed a Ti:sapphire amplifier. The power of the oscillator pulses is increased by chirped pulse amplification (CPA) [88], which enables significantly higher peak power. By stretching the oscillator pulses in time, they can be more easily amplified without damaging the experimental apparatus. Temporal broadening is achieved using dispersive glass and chirped mirrors, giving the pulse a longer duration. This also gives the pulse a large *chirp*, meaning that the different-wavelength components of the pulse are separated in time. Positive and negative chirp refers to pulses where the frequency increases or decreases over time, respectively.

The longer pulse can be safely amplified without its intensity becoming high enough to induce undesirable nonlinear effects. The amplified pulse, which at this point is positively chirped, is recompressed using a prism compressor wherein group-delay dispersion gives the pulse a negative chirp.

In a typical implementation of such a scheme, the pulse undergoes self-phase modulation (SPM) in the final prism of the compressor. SPM is a result of the optical Kerr effect - the phenomenon whereby a medium's refractive index changes due an applied electric field [89, 90] - and here manifests due to the electric field of the laser pulse as it propagates through the prism. This can change the frequency spectrum of the pulse [91–93], and with negatively chirped pulses would result in spectral narrowing [94].

The experiments described here employ a modified compression scheme similar to that described by Cavalieri *et al.* in 2007 [95]. Here, the pulse retains a negative chirp after exiting the prism compressor, whereupon it is further compressed by a positive-dispersion mirror compressor. At this stage the pulse has a full width at half-maximum (FWHM) duration of 22 fs and an energy of 1 mJ.

The pulse then passes through a hollow-core fibre (HCF) filled with neon gas, wherein it undergoes spectral broadening due to SPM. It is also temporally stretched by linear dispersion in the HCF. The increased bandwidth enables further reduction of the pulse duration in a negative-dispersion chirped mirror compressor. This final step results in pulses with a FWHM duration of 3.3 fs, a wavelength around 600 nm, and up to 600 µJ pulse energy. These optical pulses are focused into a neon gas target with over 10^{15} W/cm^2 laser intensity, inducing HHG with cutoff photon energy above 250 eV.

3.2.1.2 XUV multilayer optics

In order to produce an isolated attosecond pulse, a small fraction of the XUV spectrum must be selected. The laboratory used in this work is equipped with unique flexibility in the wavelength of its XUV pump, allowing the properties of the pulse to be adapted as required. This is achieved through the use of specially-designed multilayer mirrors that reflect only the desired portion of the XUV light, enabling the bandwidth and duration of the XUV pulse to be tuned and optimised [96, 97].

The multilayer coatings applied to the mirrors are composed of alternating layers of two different materials [96–99]. A periodic multilayer comprises repeated identical pairs of layers, whilst each layer in an aperiodic multilayer

can differ in thickness. The design of these optics is informed by Bragg's Law. In the case of a periodic crystal lattice comprising evenly-spaced planes, the Law states that

$$n\lambda = 2d \sin\theta, \tag{3.16}$$

where n is an integer corresponding to the diffraction order, λ and θ are the wavelength and angle of incidence of the incoming light respectively, and d is the distance between each lattice plane.

The layers in a multilayer optic have a thickness d comparable to λ. Each layer scatters a portion of the incident light and, with the correct design, ensures that the desired wavelengths at the desired angle of incidence θ interfere constructively. The fact that the resultant mirror's reflectivity is strongly dependent on the incident light's wavelength makes these optics a powerful tool for tailoring XUV pulses in attosecond experiments. The correct multilayer structure reflects XUV light in a desired narrow band of wavelengths, tuning the time and energy resolution of the system. It is not possible to fully optimise both of these parameters: the shorter a pulse is in the time domain, the wider its bandwidth in the frequency domain. This *time-bandwidth limit* is reached when a pulse's spectral phase is constant across all frequencies - all its frequency components interfere constructively around its central frequency and destructively elsewhere. For a Gaussian pulse, the minimum possible time-bandwidth product is 0.441, so that

$$\sigma_t \sigma_f \geq 0.441 \tag{3.17}$$

for a pulse duration σ_t and frequency bandwidth σ_f. A pulse that satisfies the equality in equation (3.17) is called *transform-limited*, *bandwidth-limited* or *Fourier-limited*.

Several candidate multilayer structures were designed and fabricated in collaboration with Saša Bajt's group at Deutsches Elektronen-Synchrotron for the experiments described here. The reflectivity curve of the mirror used to collect the data presented in this chapter is shown in Figure 3.5. It is centred at 161 eV and has a FWHM of 3.8 eV for light at a 2.5-degree angle of incidence. The peak reflectivity is around 9%. The relatively broad spectral bandwidth facilitates the extreme time resolution required for these experiments at the expense of some spectral fidelity; according to equation (3.17), the minimum possible Gaussian pulse duration with this bandwidth is 480 attoseconds.

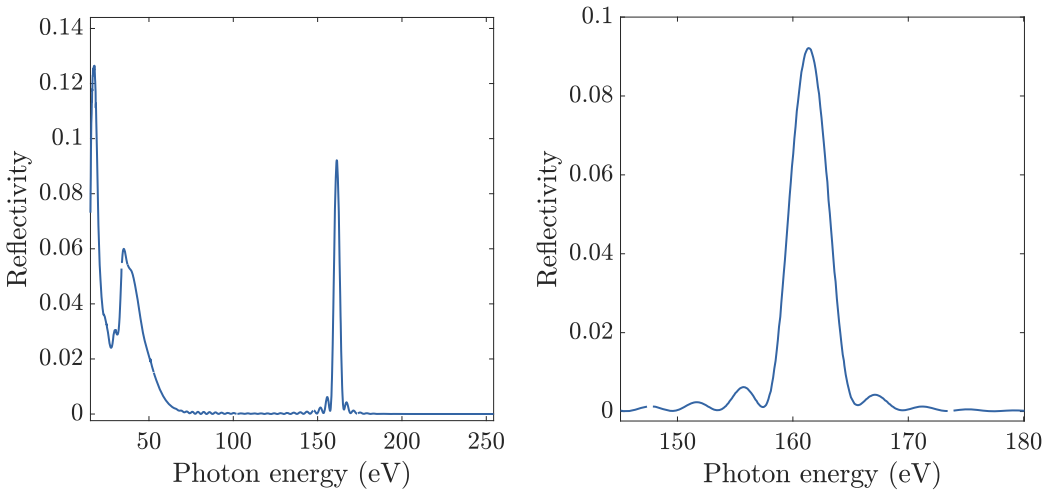

Figure 3.5: **Multilayer reflectivity curve.** Reflectivity of the multilayer mirror as a function of photon energy, measured at Berliner Elektronenspeicherring-Gesellschaft für Synchrotronstrahlung. The left- and right-hand panels show the full reflectivity curve and the region of interest respectively. The mirror has a peak reflectivity of 0.09 at a central energy of 161.4 eV, and its FWHM bandwidth is 3.8 eV.

3.2.1.3 Photoelectron streaking

The final steps in the experimental apparatus are illustrated in Figure 3.6. The 161-eV attosecond XUV pulses reflected by the multilayer mirror are used as a pump to induce photoemission in a neon gas target, resulting in a 2p electron peak centred around 140 eV and a 2s peak at 112 eV. These are among the highest-frequency XUV pulses yet applied in attosecond streaking spectroscopy. The few-cycle optical laser pulse used to produce those XUV pulses via HHG is also used as a probe in the experiment, interacting with the photoelectrons and imprinting upon them a time-dependent change in kinetic energy, which can be measured using a time-of-flight detector. This procedure is performed for a range of pump-probe delays to study the difference in behaviour for each of the two photoelectron peaks - since they are expected to be emitted at different times, they will interact with different parts of the streaking pulse for a given pump-probe delay.

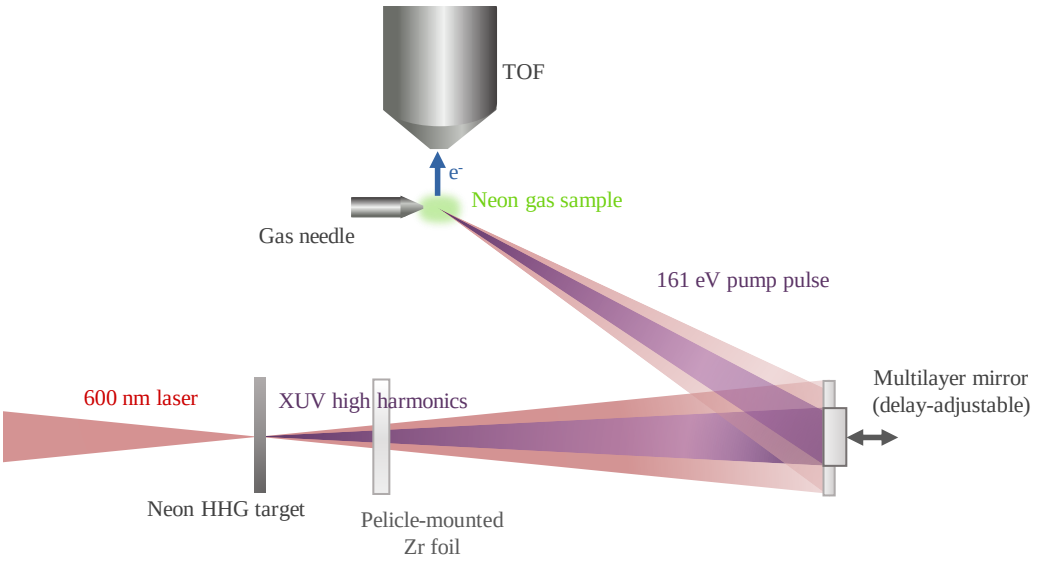

Figure 3.6: **Experimental setup for measuring photoemission delays.** The CEP-stabilised, 3.3 fs, 600 nm drive laser is focused into a thin tube filled with neon gas, puncturing the tube and producing high-harmonic XUV radiation. The optical and XUV light, now collinear, pass onto a circular zirconium foil - which transmits XUV but not optical light - suspended in the centre of the beams using a pelicle filter. Thus, the centre of the 600 nm laser is blocked, and only the XUV radiation falls upon the multilayer mirror discussed in section 3.2.1.2. The ring-shaped optical laser instead hits a larger silver mirror behind the multilayer optic. Both mirrors focus the two beams onto a neon gas sample, which is injected into the chamber using an adjustable gas needle. The multilayer optic is mounted upon a delay stage that can move backwards and forwards along the beam's direction of propagation, thereby varying the relative arrival times of the two pulses at the sample. Photoelectrons, ejected by the XUV pulse and streaked by the optical probe, are collected by a time-of-flight (TOF) detector placed above the interaction region.

3.2.2 Results

Once a spectrum has been acquired for each pump-probe delay, all spectra are plotted as a function of time to form a spectrogram as shown in Figure

3.7. The 2p and 2s peaks (at 140 and 112 eV respectively) are clearly visible, along with the sinusoidal oscillation whose period corresponds to that of the streaking pulse.

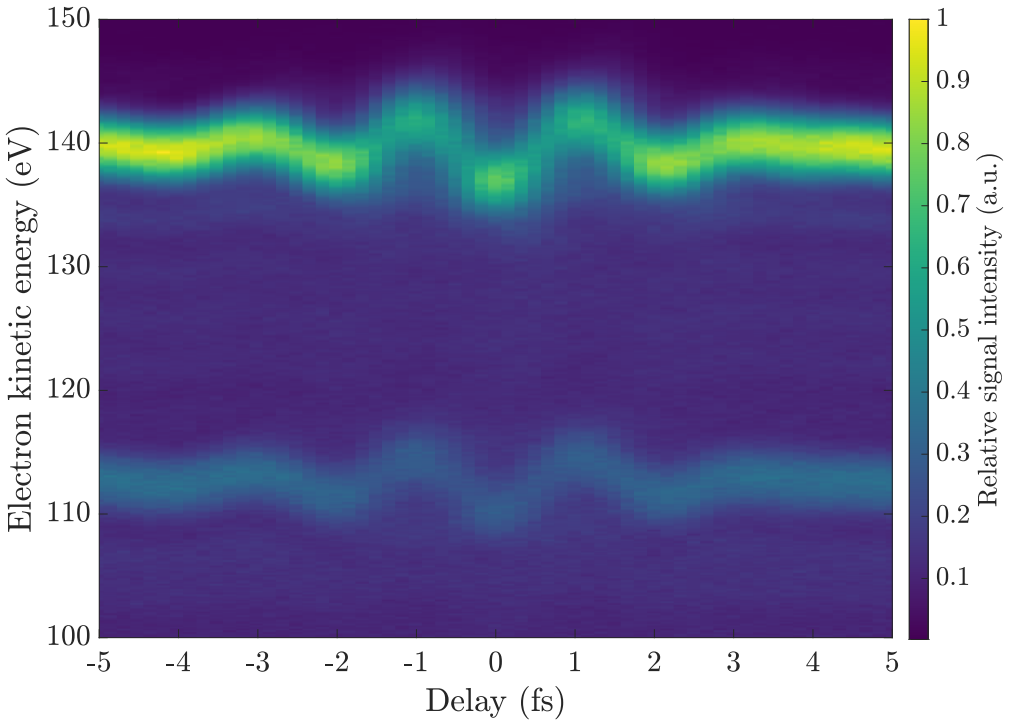

Figure 3.7: **Attosecond streaking in neon.** 2-D spectrogram of data acquired from an attosecond streaking experiment in neon gas. The 161-eV XUV pulses induce emission of 2p and 2s photoelectrons with 140 and 112 eV kinetic energy respectively. The photoelectrons are streaked by an optical laser pulse and then recorded by a time-of-flight detector. Each horizontal slice of the spectrogram corresponds to a position of the pump-probe delay stage, which controls the relative arrival time of the two pulses.

The TOF detector is tuned so as to optimise the collection efficiency of the scarcer 2s electrons. As a result, good resolution is attained on 2p and 2s peaks simultaneously, though the 2p peak remains stronger. The goal of our analysis will be to ascertain whether, and to what extent, the two sinusoidal curves are temporally displaced. Since the 2s-2p delay is expected

to be on the order of a few attoseconds [57, 81, 82], advanced analysis tools are required to discern it. The retrieval algorithm used in this work was developed by Stefan Neppl and has been applied to similar data in the past [57, 67, 72, 100].

3.2.2.1 Delay retrieval

With the delay between emission of 2p and 2s peaks on the order of a few attoseconds, it is challenging to directly measure it from spectrograms such as the one in Figure 3.7. In some investigations of photoemission delays, the measurement has been possible by calculating the centre of mass of each peak at each delay step [4]. These centres of mass can be plotted as a function of pump-probe delay, and the resultant sinusoidal curves will be out of phase with one another, with the time offset between the two curves equal to the delay between the corresponding electron emissions. Similar methods will be explored in subsequent chapters of this thesis, but are infeasible for the present experiment, since the 2s-2p emission delay is commensurate with the XUV-streaking delay step size. Instead, it can be determined with the aid of a simulation, comparing the measured spectrogram with that obtained from an established quantum-mechanical description of streaking experiments rooted in the strong-field approximation. In this model, the energy spectrum of the emitted photoelectrons is given as a function of their momentum p and the pump-probe delay Δt by the following equation [72]:

$$S(p,\Delta t) \propto \left| \int_{\infty}^{\infty} dt \tilde{E}_{XUV}(t+\Delta t)\tilde{D}(p+A(t)) \right. \\ \left. * \exp\left[i\phi_V(p,t)\right] \exp\left[it\left(\frac{p^2}{2}+E_I\right)\right] \right|^2 . \tag{3.18}$$

In equation (3.18), $\tilde{E}_{XUV}$ represents the attosecond pulse envelope, obtained via Fourier transform of its spectrum, $\tilde{D}(p+A(t))$ is the dipole matrix element corresponding to the transition from the ground state to the continuum, A is the streaking laser's vector potential, and E_I is the ionisation energy of the initial state. The Volkov phase

$$\phi_V(p,t) = -\int_t^{\infty} dt' \left[pA\left(t'\right) + \frac{1}{2}A^2\left(t'\right) \right] \tag{3.19}$$

is an additional phase accrued by the electron due to its movement within the streaking laser's electric field [101]. A least-squares fitting procedure using equation (3.18) is possible, but computationally expensive. It can be made more feasible by applying the central momentum approximation (CMA) [72, 100], in which the photoemission transition matrix element $\tilde{D}(p + A(t))$ is treated as a constant equal to its average value. The Volkov phase term $\exp[i\phi_V(p,t)]$ in equation (3.18) is approximated as $\exp[i\phi_V(p_0,t)]$, where p_0 is the central momentum of the field-free photoelectron distribution. This enables the streaked spectrum $S(p_0, \Delta t)$ to be calculated via fast Fourier transform for each delay step Δt.

The retrieval algorithm follows a least-squares optimisation procedure upon the parameters summarised in the table below. The parameters in bold are those for which we can already make a good estimate, and can thus set initial values that will be close to the final values.

Sample	*XUV pulse*	*Streaking pulse*
2p binding energy	**Photon energy**	**Wavelength**
2s binding energy	FWHM duration	FWHM duration
2p cross-section	Chirp	Chirp
2s cross-section		**Carrier-envelope phase**
Photoemission delay		Vector potential amplitude

Operating iteratively, the algorithm introduces small variations in each parameter and calculates a spectrum for each delay step using equations (3.18) and (3.19) and the CMA. Once a spectrum has been calculated for every delay step, it is compared to the recorded data. The algorithm optimises each parameter such that the full calculated spectrogram closely matches the measurement, whereupon the final parameters - including the photoemission delay - are recorded.

3.2.2.2 Discussion

Over the course of the experiment, a total of 51 scans were performed, each resulting in a spectrogram like that shown in Figure 3.7. Subsequently, each spectrogram was analysed using the quantum-mechanical retrieval algorithm and the photoelectric delay was identified as described in section 3.2.2.1. These delays and their uncertainties are shown in Figure 3.8. The average XUV pulse duration was 490 ± 40 attoseconds (FWHM), extremely close to the transform limit for its spectral bandwidth. The average linear chirp in

the XUV pulse was 0.16 ± 0.08 fs^{-2}.

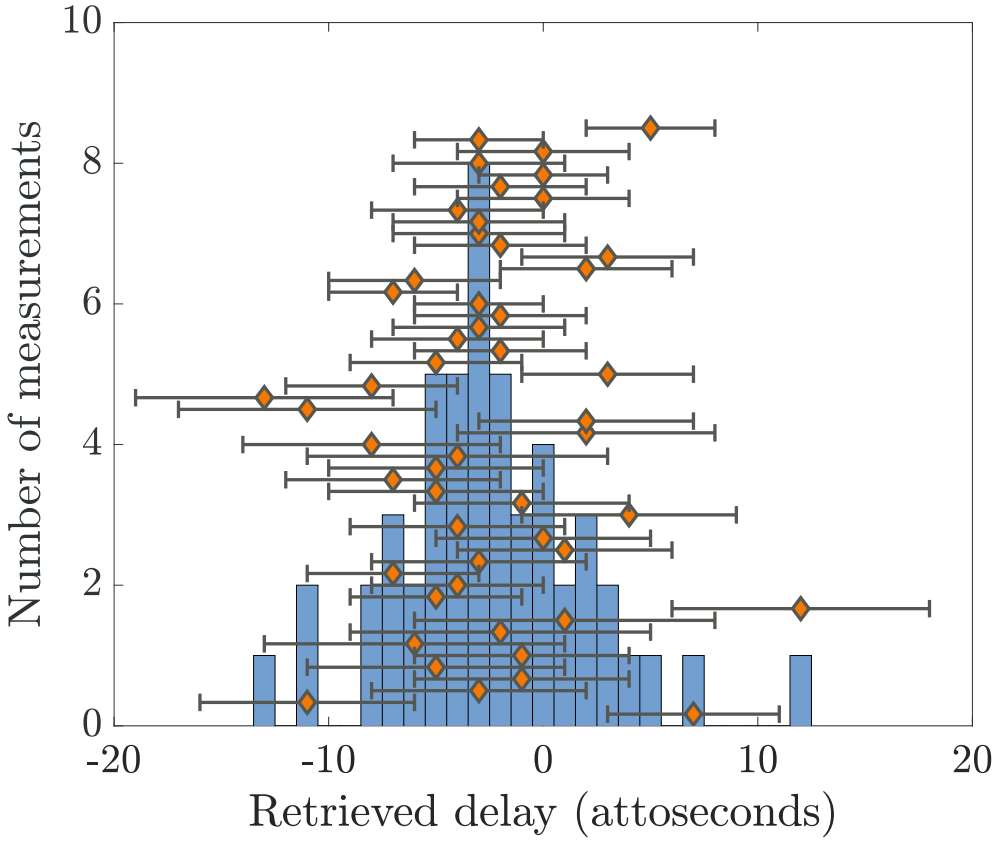

Figure 3.8: **Retrieved photoemission delay.** Plot and histogram of the retrieved delays from 51 streaking measurements. The horizontal axis represents the time that elapsed between 2s and 2p emission, so that a negative value corresponds to the case where the 2p electrons were emitted prior to the 2s electrons. The orange diamonds and error bars indicate each of the individual measurements and their uncertainties, whilst the blue histogram shows the overall trend.

After eliminating the one outlier in Figure 3.8 at 12 attoseconds, the mean delay is -3 attoseconds and the standard deviation is 4 attoseconds. The retrieved streaking laser intensity varied between 100 GW/cm^2 and 500 GW/cm^2, with no correlation between laser intensity and retrieved photoemission delay. It is notable that the average delay is negative, meaning that

our results indicate that neon 2p electrons are emitted earlier than 2s electrons; this is the reverse of the results obtained in other experiments [57, 80]. The present work employs a significantly higher photon energy than that used in the past, and photoemission delays are dependent upon ionising photon energy [74, 79, 84, 85]. However, current theoretical models do not predict a delay with this sign, even at the present XUV wavelength.

Consensus between theory and experiment for this value has been difficult to achieve since the first measurement in 2010, and this chapter contains yet another result that cannot be reconciled with present theoretical models. Notably, unlike the 2010 result, the delay measured here has a magnitude close to that expected from theory - the discrepancy is only in the sign of the result. Extensive checks and tests have been performed to ascertain whether the unexpected sign might be explained by computational, apparatus-related, or even human error during the experiment or analysis, yet no evidence has been found. In the near future, the experiment will be repeated to conclusively establish the veracity of the result. These upcoming experiments will also be performed at several different XUV wavelengths, which will establish a general trend in attosecond streaking measurements of neon 2s-2p delays, and perhaps help to uncover why streaking experiments have thus far diverged from theoretical predictions.

There are very few experimental benchmarks for the neon 2s-2p photoemission delay, and none have employed photon energies as high as that used here. Figure 3.9 illustrates the measurements that have been made to date and compares them with theoretical expectations. At lower photon energies, good agreement with theory has been achieved using the RABBIT technique, shown by the green squares in Figure 3.9. Thus far, similar agreement has not been achieved in attosecond streaking experiments; neither the 2010 result (orange circles) nor the present measurement (blue diamond) appear to match theoretical predictions. It is not yet clear whether these discrepancies are due to the higher photon energy in these studies or to effects inherent to attosecond streaking methodology, but future streaking experiments at a wider range of XUV photon energies will provide further insight.

New theoretical modelling may be able to elucidate the reason for the unexpected sign of the results presented here. According to current models, there are multiple effects that contribute to the measured delay, including correlated inter-electron phenomena and the changes wrought by the streaking field on photoemission processes [85]. Though shake-up effects are expected to have an impact on these investigations, the present spectral resolution is

sufficient to avoid satellite peaks obfuscating the ordinary 2s emission peak, due to the relatively narrow XUV bandwidth. The satellite peak nearest the direct 2s emission peak occurs due to 2p shake-up and is centred around 5 eV from the centre of the 2s peak; further, at higher photon energies the cross section of the 2p peak decreases relative to that of the 2s peak, which should reduce the intensity of this satellite peak compared to previous experiments at lower photon energies [87].

As the time resolution available to experimentalists improves by orders of magnitude, it will become ever more important to understand and measure the exact timing of the photoelectric effect. Since there is some nonzero delay τ_{PE} between an attosecond pulse hitting a sample and photoelectrons emerging, systematic errors will appear in the measurement of all attosecond electron dynamics, which will appear to be occurring τ_{PE} later than in reality. Moreover, the fact that electrons in different orbitals are ejected at different times must be accounted for in future attosecond time-resolved studies of intra-atomic electron dynamics.

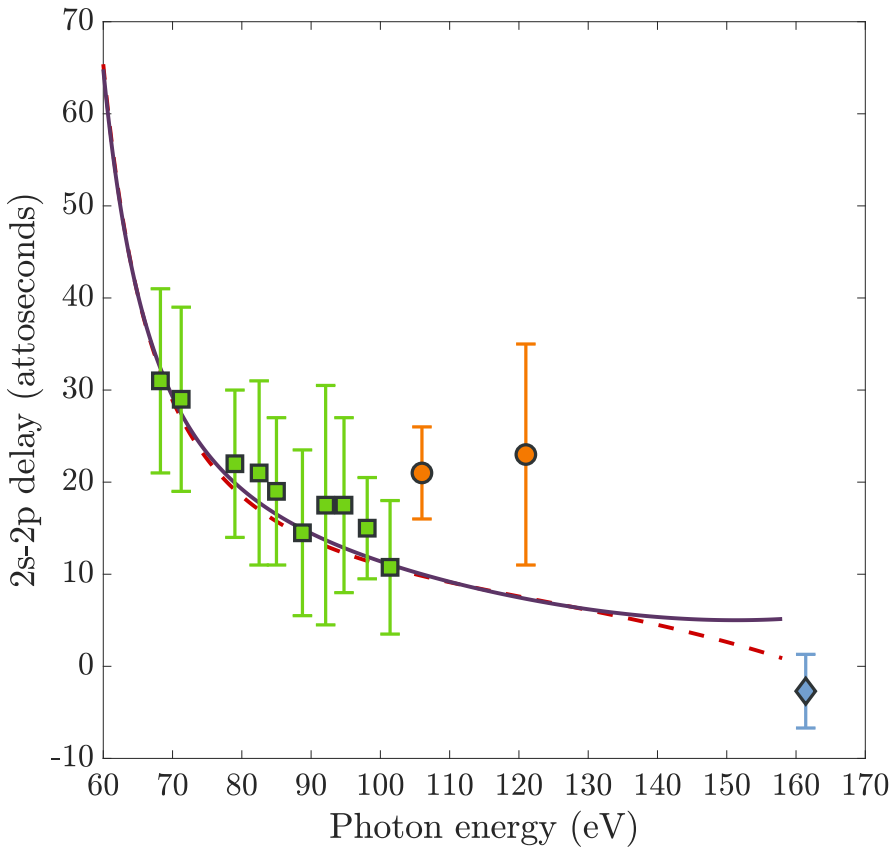

Figure 3.9: **Comparison between theory and experiment.** Delays between 2s and 2p photoemission in neon from two theoretical calculations are shown, along with experimental measurements, as a function of photon energy. The two lines are from the paper *"Time delays for attosecond streaking in photoionization of neon"* by J. Feist *et al.* [85]; the dashed red line shows calculations made using a model with two target states whilst the solid purple line incorporates 38 target states, including shake-up channels. The two orange circles show the photoemission delays measured by Schultze *et al.* using attosecond streaking spectroscopy in 2010 [57], the green squares are the values measured by Isinger *et al.* with RABBIT in 2017 [80], and the blue diamond is the attosecond streaking measurement described in this chapter. Thanks to Johannes Feist for permission to reproduce this figure and for provision of the theoretical data.

Chapter 4

Self-referenced attosecond streaking

XFELs are immensely powerful tools for physical science, with access to truly unique light pulses, as discussed in Chapter 2. And yet, their full potential for attosecond-resolution time-resolved studies has hitherto been difficult to realise. Though the pulses produced at XFEL facilities are presently starting to enter the attosecond regime [11], there are major challenges inherent to any attempt to apply attosecond-resolution techniques such as those described in Chapter 3 at XFELs. Development of new instrumentation, or new methods, is essential so that these light sources can be exploited to their full potential. This chapter will describe the development, application, and future of a technique termed *self-referenced attosecond streaking*, which is able to bring the methods and time resolution from the table-top world to XFEL facilities. Chapter 4 has been adapted from the paper *"Clocking Auger electrons"*, which was published in 2021 [102].

4.1 Requirements and principles

As discussed in Chapter 3, control over the streaking arrival time and CEP is typically essential for attosecond streaking spectroscopy. XFELs, generally, cannot provide control over either of these parameters. If we are to take advantage of the favourable characteristics of XFELs, such as their wavelength flexibility and extreme brilliance, we must seek a route to attosecond streaking that escapes the typical requirements.

4.1.1 Jitter in timing and phase

The fluctuation in streaking parameters is referred to as *jitter*, and we must contend with two forms of it in XFEL-based attosecond streaking experiments. The first, timing jitter, is the uncertainty in the arrival time of the X-ray pulse relative to an external streaking pulse, and is a major inhibitor to attosecond time resolution at XFELs. In contrast to the table-top HHG sources described in section 3.1.2, the generation of XFEL pulses is entirely independent of any streaking laser pulse used as a probe. Timing jitter arises predominantly due to the tremendous difficulty in synchronising these pulses to arrive simultaneously at a target that may be hundreds of metres from the light source, and also due to inevitable fluctuations in the SASE process by which XFEL pulses are typically produced: as described in section 2.2, SASE is initiated by random noise in the electron bunch, introducing a small amount of additional timing jitter dependent on the length of the electron bunch.

If each XFEL pulse arrives at a different relative time, the amplitude of the streaking pulse envelope $E_0(t)$ will differ, and the photoelectrons will interact with a different streaking amplitude. Generally, timing jitter means that the temporal resolution for XFEL-based streaking experiments is limited not by the ionising pulse duration, but by the precision with which pump and probe can be synchronised, which is typically on the scale of tens or hundreds of femtoseconds.

The second form of jitter that must be overcome before attosecond streaking spectroscopy can succeed at an XFEL is phase jitter. Most XFEL facilities do not currently have access to CEP-stable streaking laser pulses, so each successive laser pulse will not generally have the same CEP as its predecessor; the phase of the field with which the electrons interact will vary randomly between each pump-probe measurement. This unstable CEP means that each final electron kinetic energy cannot be straightforwardly mapped to a unique moment in time - even if the two pulses are perfectly synchronised.

In summary, the extension of attosecond streaking spectroscopy is impeded by fluctuation in two laser parameters: timing and phase. If these can be controlled, or measured, XFELs could be used to pump or probe electron dynamics in streaking experiments. In a typical attosecond streaking experiment, both the relative arrival time (via synchronisation) and phase (via CEP stabilisation) of the streaking pulse are tightly controlled and can be modified at will. In an XFEL setting, we cannot exert *control* over these quantities,

but perhaps we can instead *measure* them and simply gather enough data to cover the full parameter space. This is the goal of self-referenced streaking: to accept our lack of control in these experiments, and to mitigate it after the fact by identifying the crucial unknowns - the streaking amplitude and phase - for every individual measurement.

4.1.2 Overcoming jitter

If we are to work around two unknown parameters for each streaked spectrum obtained in our experiment, we must make at least two measurements with each pump-probe pair. For the two measurements to provide meaningful, distinct information, they can be made at different phases of the streaking field.

This could be accomplished by making streaking measurements of two types of electrons simultaneously. Provided that they are well-separated in kinetic energy, so that their spectra do not overlap, both electron emission peaks could be measured with a single TOF detector. Further, if they are emitted at different times, the phase of the streaking field will advance between the first and second emission, and the two types of electrons will interact with two different streaking phases. This phase advance will notably be just as consistent as the time between emission events; if a large amount of measurements are made, each with a different, random combination of pump-probe delay and CEP, a pattern will emerge due to the nonrandom phase advance, which is consistent for every measurement pair.

There is some precedent for this in existing attosecond streaking methodology: the two streaked curves in Figure 3.7 are separated by a phase shift due to their delayed emission times (albeit, in that experiment, the shift is too small to be perceptible from examining the figure alone). Consider a system in which the delay between the two electron emissions, τ_{delay}, is a larger fraction of the streaking period. As a function of pump-probe delay, the sinusoidal curves traced out by the two emission peaks' centres of energy are temporally displaced by the time elapsed between the two events, as illustrated in Figure 4.1a and Figure 4.1b. In effect, each peak in the electron energy spectrum independently samples the oscillation of the streaking vector potential at a different phase. When plotting the two streaked centres of energy against each other, as in Figure 4.1c, the resultant ring has an ellipticity determined by the phase shift between the two sine curves. A phase shift of 0 (i.e. the case where both emissions were simultaneous) would result in a

straight line, as both emissions would experience the same vector potential in each shot. If the shift were $\frac{\pi}{2}$, the graph would be a wide ellipse with major and minor axes parallel to those of the coordinate system, because whenever one emission interacted with a zero-crossing of the streaking field, the other would interact with an extremum. Finally, a phase shift between 0 and $\frac{\pi}{2}$ leads to a sheared ellipse.

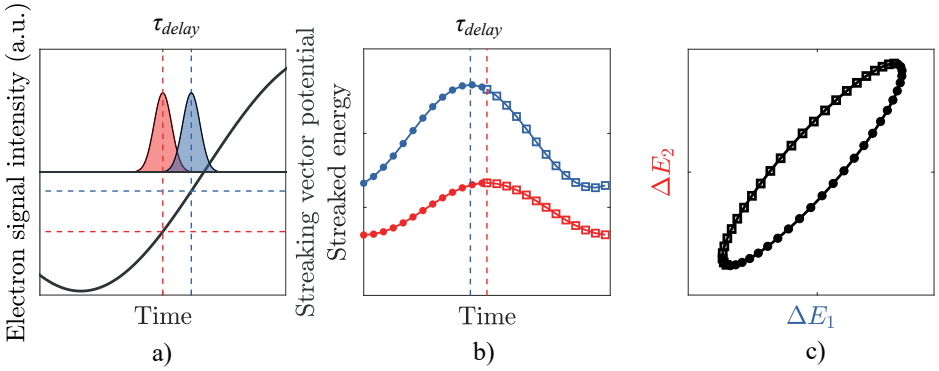

Figure 4.1: **Principle of self-referenced photoionised streaking measurements.** a) The photoelectrons (red) are emitted promptly with the arrival of the X-ray pulse at T_0. A short time later, the second set of electrons (blue) are emitted. The delay between the emission peaks' weighted centres, τ_{delay}, which is highlighted by the distance between the vertical dotted lines, causes each set of electrons to interact with a different phase of the streaking pulse (solid black line). The horizontal dotted lines further highlight the difference in streaking vector potential in each case. b) If the temporal overlap were smoothly varied over one streaking cycle, the changes in kinetic energy felt by the peaks would trace out sinusoidal curves, separated by τ_{delay}. Filled circles represent positive streaking slopes at the moment of ionisation and open squares represent negative slopes. The dotted lines highlight the temporal overlap which results in the largest increase in kinetic energy for each peak, so that the gap between the dotted lines corresponds to the temporal shift between the two sinusoidal curves. c) Plotting each pair of positions against each other results in an ellipse. ΔE_1 on the x-axis represents the delayed (blue) peak, whilst ΔE_2 on the y-axis represents the prompt (red) peak. Filled circles and open squares have the same meaning as in (b). This figure was adapted from Figure 2 in *"Clocking Auger electrons"* [102].

The key concept upon which self-referenced streaking is built is the realisation that, unlike the sine curves in Figure 3.7 or 4.1b, the ellipse in Figure 4.1c does not depend upon timing or phase control, only on the fact that the two peaks interact with a different streaking phase for each measurement. Indeed, one could scramble the data in Figure 4.1b along the x-axis, but as long as each pair of measurements remain associated, plotting one set against the other will always result in the characteristic ellipse. The delay between the two electron emissions determines the shape of the ellipse, and hence that shape will provide the information necessary to calculate τ_{delay}. Therefore, we need only perform the experiment in spite of the jitter, allow the streaking parameters to fluctuate randomly, and accumulate enough data to explore the entire parameter space. For a proof-of-principle experiment, we should select a candidate system with two electron emission peaks displaced by a few femtoseconds, which will demonstrate to what extent self-referenced streaking can enhance the time resolution available at XFELs.

4.2 Auger-Meitner decay

An example of a process involving a delayed electron emission event is Auger-Meitner decay, first discovered by Lise Meitner in 1922 [103, 104] and independently observed by Pierre Auger the following year [105]. Auger-Meitner decay is a fundamental manifestation of correlated electron dynamics: phenomena wherein the action of one electron affects another. The process, illustrated in Figure 4.2, is initiated when a tightly bound electron in an atom or molecule is ejected, either by absorption of an X-ray photon or collision with an energetic particle. When a more weakly bound electron fills the resulting core-hole, the energy released by this relaxation process can induce ejection of another electron, known as an Auger-Meitner electron [106]. Multiple Auger-Meitner decay channels are possible, usually being denoted in terms of the involved energy levels. In the experiment discussed in this chapter, we will examine the KLL decay channel, which involves one core level (K) and two valence levels (LL).

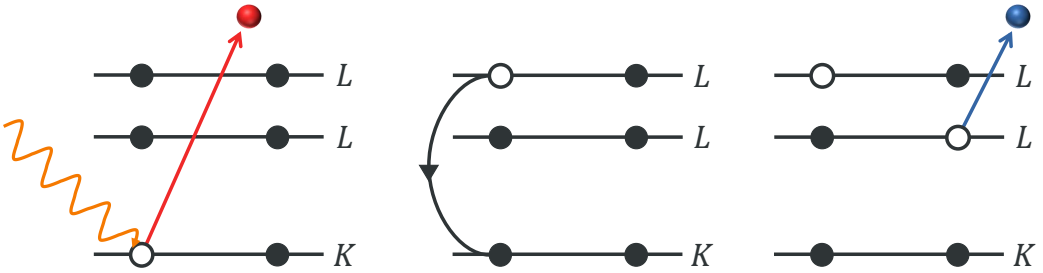

Figure 4.2: **Auger-Meitner decay.** Simple illustration of Auger-Meitner decay with time increasing from left to right. A light pulse (orange) ionises an atom and ejects an electron from a core level (K). The hole left behind by this photoelectron (red) can be filled by an electron from an outer (L) shell, which releases energy as it relaxes. This energy causes emission of another electron, termed an Auger-Meitner electron (blue).

This non-radiative process is the dominant decay mechanism for elements with a low atomic number. In these cases, the core-hole decay lifetime is essentially equivalent to the Auger-Meitner decay lifetime, and on the order of femtoseconds [2, 107, 108]. When the core-hole is created by photoionisation, the Auger-Meitner decay lifetime is related by the uncertainty principle to the spectral linewidth of the photoemission line [108–110]. High-resolution electron spectra, mostly measured using high-brightness synchrotron sources [106, 109, 111] have therefore been used to infer Auger-Meitner decay lifetimes.

4.2.1 Attosecond Auger-Meitner experiments

As an alternative to the aforementioned spectral-domain studies, it is possible to access these dynamics directly in the time domain using ionising pulses with a duration comparable to, or shorter than, the Auger-Meitner decay lifetime. For example, in proof-of-principle experiments in krypton [2] using relatively weak, table-top attosecond XUV pulses [112–114], core-holes were created by photoionisation, and Auger-Meitner decay was time-resolved using attosecond streaking spectroscopy.

There is, therefore, some history of attosecond streaking spectroscopy being used to study Auger-Meitner dynamics, yet the results in this chapter represent the first such study to take place at an XFEL. Compared to table-top HHG sources, XFELs' significantly higher photon energies enable them to

induce Auger-Meitner dynamics involving deeply-bound core-level electrons. Further, the brilliance of XFEL pulses is many orders of magnitude larger than that of XUV pulses produced by HHG, dispensing with the need to average many measurements in order to procure a strong signal. If self-referenced streaking can overcome timing and phase jitter, these advantages can be exploited to make attosecond measurements not just of Auger-Meitner decay, but of a wide range of electron dynamics in highly excited states of matter [42–48, 115–118], many of which are constrained or influenced by Auger-Meitner decay.

4.2.2 Modelling Auger-Meitner decay in streaking experiments

In a number of past attosecond investigations of Auger-Meitner decay [119–122], the temporal profile of Auger-Meitner emission $n(t)$ has been approximated by a convolution of the XUV pulse profile with an exponential decay curve:

$$n(t) = \int_{-\infty}^{t} dt' \exp\left(-\frac{t'^2}{\sigma_X^2} - \frac{(t-t')}{\tau_A}\right), \tag{4.1}$$

where τ_A is the Auger-Meitner decay lifetime. This phenomenological *ad hoc* model is based on a two-step description of Auger-Meitner decay, and treats the ionisation and Auger-Meitner emission as distinct processes. Recently, an alternative fully quantum-mechanical model has been proposed [123, 124], which treats the time-dependent Schrödinger equation within the strong field approximation (SFA). Within this approach, the Auger-Meitner process is considered as a single-step excitation-decay of the vacancy, or Auger-Meitner, state. Both creation of the vacancy and its subsequent decay into the non-stationary wavepacket of the Auger-Meitner electron are considered as a single quantum-mechanical process. A similar approach was developed earlier for resonant Auger-Meitner processes in molecules [125, 126]. The quantum-mechanical model treats Auger-Meitner decay in terms of the amplitudes of the states involved – that is, the vacancy state and the continuum of states of emitted Auger-Meitner electrons – while the *ad hoc* rate-equation approach treats the process in terms of the real-valued populations of those states. The emission profile as a function of time is given in the quantum model [102] by

$$n_q(t) = \frac{1}{2\pi\tau_A} \exp\left(-\frac{t}{\tau_A}\right) \left(\int_{t_0}^{t} dt' \exp\left(\frac{t'}{2\tau_A}\right) \tilde{\varepsilon}_X(t')\right)^2. \tag{4.2}$$

The two models give similar results when the exciting pulse is much shorter than the Auger-Meitner lifetime. However, as the exciting X-ray pulse becomes comparable to or even longer than the Auger-Meitner decay lifetime, a substantial difference appears in the emission profiles predicted by the two models. This is determinative when operating with XFEL pulses, which, like Auger-Meitner decay lifetimes, typically have durations of multiple femtoseconds.

In the context of this experiment, the difference in the emission profiles is manifested in terms of the quantity we intend to measure: the time delay between the centres of mass of the photoemission and Auger-Meitner emission bursts. The profiles predicted by the *ad hoc* two-step model have their centres of mass displaced exactly by the Auger-Meitner decay lifetime, but this is not so in the quantum-mechanical model we used to determine our final results, and we must perform an additional step to retrieve the decay lifetime from the observed time delay, which will be described in section 4.3.5. Further discussion and comparison of the two theoretical models can be found in *"Clocking Auger electrons"* [102], particularly in the Supplementary Information.

4.3 Measuring the Auger-Meitner decay lifetime in neon

This section will present an experimental study of photoinduced Auger-Meitner emission in the time domain, using intense, femtosecond soft X-ray pulses from an XFEL of duration commensurate with the core-hole lifetime. Under these conditions, the *ad hoc* two-step model fails, and a full quantum-mechanical treatment must be used, resulting in an Auger-Meitner decay lifetime that is consistent with past high-resolution spectroscopic measurements. This work, therefore, represents an experimental demonstration of the quantum effect in the delay between photoionisation and Auger-Meitner decay, and emphasises the general importance of treating the Auger-Meitner process as a single-step quantum-mechanical process when performing future XFEL experiments.

4.3.1 Time-resolved electron spectroscopy

A schematic of the experimental apparatus at the LCLS XFEL is shown in Figure 4.3. Core-level 1s photoemission and subsequent Auger-Meitner decay are induced by an XFEL pulse whose photon energy is centred at 1130 eV with 5 eV spectral bandwidth. Based on the average pulse energy, the fluence is estimated to be below 40 J/cm^2. The pulse is directed into a dilute neon gas target, and the photo- and Auger-Meitner electrons are analysed using a time-of-flight spectrometer equipped with an electrostatic lens to increase the collection efficiency. Single-shot measurements of both peaks are performed simultaneously, taking advantage of the fact that the KLL Auger-Meitner spectrum of neon is dominated by the strong emission line associated with the Ne^{2+} $2p^4$ $^1D_2$ final state [127]. Acquiring both peaks simultaneously requires that they be sufficiently close together in energy; indeed, the spectral resolution is lower on the Auger-Meitner peak than the photoelectron peak due to the higher kinetic energy of the former.

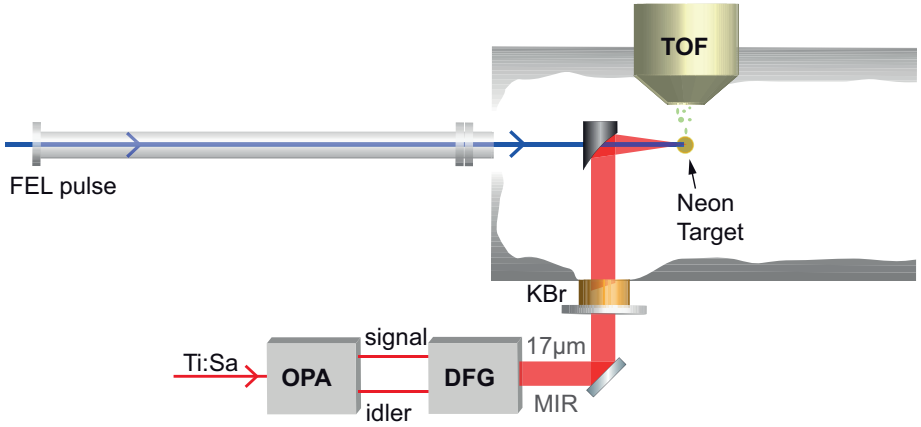

Figure 4.3: **Experimental Apparatus.** 17 μm mid-infrared (MIR) streaking laser pulses are generated by downconversion of a near-IR Ti:sapphire laser pulse, using an optical parametric amplifier (OPA) and difference frequency generation (DFG), and coupled into a chamber through a potassium bromide (KBr) window. The MIR pulses are focused with a 100-mm-focal-length parabola and overlapped with 7 fs, 1130 eV XFEL pulses in a neon gas target. The resultant streaked photo- and Auger-Meitner electron emission is measured using a large-acceptance time-of-flight (TOF) spectrometer. This figure was first published in *"Clocking Auger electrons"* [102].

Based on the peak current in the bunch compressor, the X-ray pulse duration in our experiment was estimated to be under 10 fs FWHM. As discussed in section 3.1.3, attosecond streaking requires a streaking laser whose period is at least twice as long as the dynamics of interest [112, 128]. With X-ray pulses up to 10 fs long, the photoemission and Auger-Meitner decay will occur over a similar duration, so an IR streaking field with a correspondingly long optical cycle is required. To this end, a Ti:sapphire 800 nm femtosecond laser is used as the pump source to generate IR signal and idler pulses in a barium borate crystal via optical parametric amplification. These pulses are mixed in a gallium selenide crystal for difference-frequency generation, producing MIR streaking pulses with a wavelength of 17 µm. The streaking period, therefore, is 57 fs, so we can be confident that the exciting X-ray pulse and the few-femtosecond Auger-Meitner dynamics will be fully encompassed within a half-cycle of the streaking field.

As in a table-top attosecond streaking experiment, we will make use of the equations from section 3.1.3. Recall that, as a function of time t, the linearly polarised streaking laser with angular frequency ω_{IR} has a time-dependent electric field

$$E_{IR}(t) = E_0(t)\cos(\omega_{IR}t + \phi_{CEP}), \tag{4.3}$$

and vector potential

$$A_{IR}(t) = -\frac{E_0(t)}{\omega_{IR}}\sin(\omega_{IR}t + \phi_{CEP}), \tag{4.4}$$

such that $E_{IR}(t) = -\frac{\partial A_{IR}}{\partial t}$. In this experiment the maximum amplitude of the streaking field $E_0(t)$ is around 5.6 MV/m, and the corresponding intensity is 40 GW/cm^2.

Upon interaction with the streaking laser field, the emitted photoelectrons' change in kinetic energy ΔE can be approximated by

$$\Delta E \approx \sin(\phi_i)\sqrt{8E_{el}U_p}, \tag{4.5}$$

where $\phi_i = \omega_{IR}t_i + \phi_{CEP}$ is the overall phase of the sine term at the moment of photoemission t_i and E_{el} is the electrons' field-free kinetic energy [1, 129]. As defined in section 3.1.2, the ponderomotive potential U_p is given by

$$U_p = \frac{e^2E_0^2}{4m_e\omega_{IR}^2}, \tag{4.6}$$

where e and m_e are the charge and mass of the electron respectively. As discussed in Chapter 3, equations (4.4), (4.5), and (4.6) reveal that the change in the final kinetic energy ΔE experienced by the observed electron is proportional to the vector potential $A(t)$ of the streaking field at the moment of interaction. Unlike in the table-top experiment described in Chapter 3, however, we cannot expect intrinsic synchronisation between the two light pulses, and nor will we have access to carrier-envelope-phase-stable streaking pulses. Indeed, we will not generally know which streaking amplitude and phase interacted with the electrons in each measurement, but, as described in the following sections, we will still be able to make time-resolved measurements with high precision.

4.3.2 Experimental results

The streaked kinetic energies of the photoelectron and Auger-Meitner electron peaks are determined by numerically fitting the recorded spectra in each single-shot measurement and calculating the centre of energy of each peak. In addition to the streaked measurements, we also obtained thousands of spectra in the absence of the streaking laser. By comparing the streaked energies to the corresponding streaking-field-free values, we determine the changes in kinetic energy, ΔE_{Auger} and ΔE_{1s}, induced by the streaking field in each single-shot measurement. These field-free kinetic energies can also be used to determine the distribution of photon energy jitter. The central photon energy is not identical for every XFEL pulse, but varies slightly over a small range. In our experiments this jitter follows a distribution with an r.m.s. width of 1.2 eV, which was small in comparison to the total change in the photoelectron kinetic energy induced by the streaking field. This, in conjunction with its normally-distributed nature and the fact that we average over many thousands of shots in the following treatment, allows it to be neglected. In future experiments, if the photon energy jitter were found to be non-negligible, there are multiple approaches that might be taken to mitigate or eliminate its effect. The most straightforward of these would be simultaneous reference measurements of the single-shot X-ray photon energy.

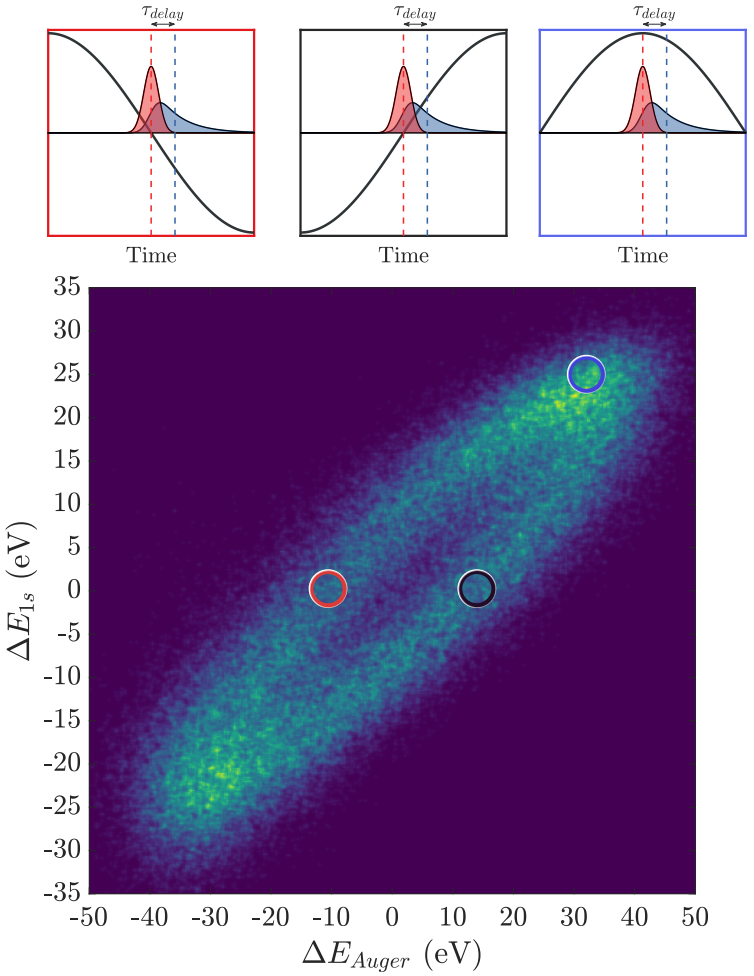

Figure 4.4: **Self-referenced streaking in neon.** Correlation map generated from 80,000 single-shot streaking measurements in neon using a 17 µm streaking field, and 7 fs FWHM, 1130 eV ionising X-ray pulses. The ΔE_{Auger} and ΔE_{1s} coordinates of the individual points in the 2-D histogram are determined by numerically fitting the streaked kinetic energy shift of the photo- and Auger-Meitner electron peaks in each shot and calculating their centres of energy. Above, three sketches are shown, corresponding to three circled regions on the map. The colour of the box around each sketch matches that of the circle in which such measurements would fall. Each sketch shows the photoelectrons (red filled curve) and Auger-Meitner electrons (blue filled curve) along with the streaking vector potential (black curve). The weighted centres of each emission profile are highlighted with vertical dotted lines. This figure is adapted from Figure 3 in *"Clocking Auger electrons"* [102].

Figure 4.4 shows the correlation between ΔE_{Auger} and ΔE_{1s} obtained from tens of thousands of streaked measurements, revealing a characteristic elliptical distribution. Specific regions of the ellipse are highlighted, with sketches of the corresponding measurement conditions shown in the subplots above the main plot. The leftmost subplot shows the photoemission overlapping with a negatively-sloped zero-crossing, so that it experiences no change in its central energy, while the later-emitted Auger-Meitner electrons have their kinetic energy reduced, so that measurements under these conditions will lie on the negative ΔE_{1s}-axis. The central sketch shows the oppositely-sloped zero-crossing, which produces measurements on the positive ΔE_{1s}-axis. The rightmost sketch shows the photoemission peak overlapping with a peak of the vector potential, leading to results at the largest ΔE_{1s} coordinates. The correlation map can be used to navigate to previously inaccessible streaking parameters: the angular coordinate of each point identifies the overall phase ϕ_i for that shot, and its radial coordinate is a function of the streaking field amplitude.

The characteristic elliptical distribution in Figure 4.4 will be used to measure the delay between photo- and Auger-Meitner emission, which itself will be used to calculate the Auger-Meitner decay lifetime. The distribution also provides access to important diagnostics. By analysing the widths of the distributions in our data and given the pulse duration of the MIR laser, which was approximately 300 fs r.m.s., we calculated that the timing jitter has an r.m.s. width of 110 fs. Self-referenced streaking enables resolution that would ordinarily be impossible with jitter this severe; we will use these data to measure a temporal delay with sub-femtosecond precision despite the presence of timing jitter that is orders of magnitude larger.

4.3.3 Calculation of the average pulse duration

The duration of the X-ray pulse is an important parameter in this experiment, as it influences the emission profile of both types of electrons. We will calculate it following the methods described in a 2014 publication by Helml *et al.* [53]. Our method is facilitated by the correlation plot shown in Figure 4.4, and provides similar resolution to established non-invasive measurements of pulse duration [41]. Figure 4.4 makes it simple to identify those shots for which the photoemission burst coincides with a zero-crossing of the streaking vector potential. Such shots appear on the 'equator' of the ellipse, where $\Delta E_{1s} \approx 0$, since the photoelectrons experienced a minimal energy shift. Af-

ter identifying these shots, it is possible to calculate the average duration of the X-ray pulse by comparing the width of the photoemission line in these maximally broadened shots to the width of the field-free photoemission lines.

In streaking experiments, the duration of an X-ray pulse can be calculated using the relation

$$\tau_X = \frac{\sigma_{DC}}{s}, \tag{4.7}$$

where σ_{DC} represents the spectral width of the streaked photoemission peak after deconvolving that of the field-free peak, and $s = \frac{dE_k}{dt}$ is the streaking speed. The latter represents the rate of change of the peak's kinetic energy with respect to the timing of the streaking pulse. Longer X-ray pulses cause photoemission to be stretched over a longer duration, leading to increased broadening in the streaked peak because the photoelectrons interact with a wider range of streaking vector potentials.

Where the X-ray and streaking pulses are well overlapped, the final energy of photoelectrons emitted at time t is given by

$$E_k(t) = \frac{\Delta E_{max-min}}{2} \sin(\omega_{IR} t) + E_{1s} \tag{4.8}$$

where $\Delta E_{max-min}$ is the difference between the most positive and most negative changes in photoelectron energy throughout the experiment, ω_{IR} is the angular frequency of the streaking field, and E_{1s} is the field-free kinetic energy of the photoelectrons. Therefore, at the zero-crossing of the streaking field,

$$s = \frac{\Delta E_{max-min} \cdot \pi}{T_{IR}}, \tag{4.9}$$

where we have used the relation $T_{IR} = \frac{2\pi}{\omega_{IR}}$ and set $t = 0$.

The value of $\Delta E_{max-min}$ is calculated from angular sectors corresponding to the maxima and minima of the streaking phase. All shots within a given angular sector interacted with the same streaking phase, but the final kinetic energy of the electrons will still vary according to the streaking field amplitude – which will itself vary due to timing jitter. The largest possible change in kinetic energy will occur when the streaking amplitude is maximal and the phase causes the electrons to interact with a peak of the streaking vector potential. Because timing jitter results in a normal distribution of streaking amplitudes, it is most likely that a given shot will intersect with the centre of

the streaking pulse envelope. These conditions are identified by numerically fitting the distribution of absolute photoelectron kinetic energies within both sectors and extracting its peak, as shown in Figure 4.5. Using this method, we determine that $\Delta E_{max-min} = 48 \pm 1$ eV.

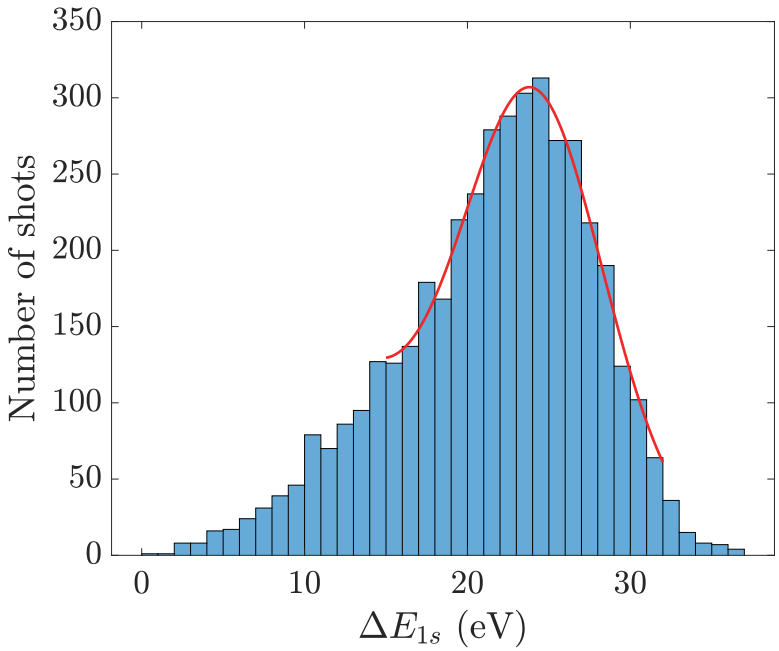

Figure 4.5: **Distribution of maximally streaked kinetic energies.** The changes in photoelectron kinetic energy in the sectors corresponding to maximal absolute streaking phase are plotted in the histogram. The red line shows the numerically determined least-square fit, from which we extract the peak of the distribution. By the normally distributed nature of timing jitter, the highest number of shots will overlap at or near the peak of the pulse envelope, so that the peak of the histogram ought to correspond to those conditions. This figure is adapted from the Extended Data of *"Clocking Auger electrons"* [102].

The first step towards finding σ_{DC} is to calculate the spectral width of the photoemission peak at the zero-crossing of the streaking field. These shots lie near to the line $\Delta E_{1s} = 0$, where the kinetic energy of the photoelectrons was largely unchanged. Further, the shots closest to the edge of the

ellipse interacted with the peak of the streaking pulse envelope, resulting in a maximised change in Auger-Meitner electron kinetic energy.

Therefore, we restrict our consideration to shots for which the final photoelectron kinetic energy was within 1 eV of its field-free value. Within this group, we take the 300 outermost shots on each side of the ellipse, corresponding to the strongest streaking effect. Recall that, as illustrated in Figure 4.4, the left and right sides of the ellipse correspond to zero-crossings of the streaking pulse with opposite slopes. Since the shots do not display any irregular structure, they can each be fit using Gaussian functions, and the width of these functions can be computed. The average spectral width of the 300 shots on the left of the ellipse is $\sigma_L = 8.9 \pm 0.2$ eV and that of the 300 on the right is $\sigma_R = 9.8 \pm 0.2$ eV. Here and in the following, we have used the standard error on the mean value of N repeated measurements, given by

$$\alpha_M = \frac{\delta}{\sqrt{N}}, \tag{4.10}$$

where δ is the statistical width of the distribution. We must deconvolve the bandwidth of the field-free photoemission peak σ_{FF} from that of the peak at a zero-crossing using the relation

$$\sigma_{DC} = \sqrt{\sigma_S^2 - \sigma_{FF}^2} = 7.9 \pm 0.2 \text{ eV}. \tag{4.11}$$

Here, $\sigma_S^2 = \frac{\sigma_L^2 + \sigma_R^2}{2}$ represents the average of the squares of the mean bandwidth at each zero-crossing. The average field-free photoemission bandwidth is $\sigma_{FF} = 4.95 \pm 0.01$ eV. The uncertainty on σ_{FF} is much smaller than that on σ_S, because there are many more unstreaked shots available to use in the calculation. The average XFEL pulse duration can be calculated using these quantities, propagating the uncertainties on each one using a standard functional approach. The average full width at half maximum (FWHM) duration of the X-ray pulse is given by

$$\tau_X = 2\sqrt{2\ln(2)}\frac{\sigma_{DC}}{s} = 7 \pm 1\text{fs}, \tag{4.12}$$

where the factor $2\sqrt{2\ln(2)}$ is used to convert from r.m.s. width to FWHM.

4.3.4 The delay in Auger-Meitner emission

As an alternative to examining features in the individual or averaged streaked Auger-Meitner spectra, which is not possible here due to limited energy resolution, the degree of ellipticity in Figure 4.4 can provide information about the delay between the two emission bursts. Any ellipse can be described using the pair of parametric equations

$$x(\theta) = A\sin(\theta + \phi_A), \quad y(\theta) = B\sin(\theta) \tag{4.13}$$

with appropriate constants A, B, and ϕ_A.

In this case, x and y correspond to the changes in kinetic energy ΔE_{Auger} and ΔE_{1s} of the Auger-Meitner and photoelectrons respectively. The angle ϕ_A is the overall phase advance that occurs between the two instants of electron emission, which will inform us about the corresponding time delay.

For the ellipse described by equations (4.13), define y_1 to be the ellipse's y-intercept and y_2 its maximum value of y, so that

$$y_1 = B\sin(-\phi_A), \quad y_2 = B. \tag{4.14}$$

It follows that

$$\phi_A = \sin^{-1}\left(\frac{y_1}{y_2}\right). \tag{4.15}$$

By examining the sectors of the ellipse corresponding to y_1 and y_2 we can calculate them, obtaining values of 8.0 ± 0.1 eV and 20.9 ± 0.1 eV respectively. Using these values in equation (4.15) enables us to calculate the phase advance ϕ_A to be 0.39 ± 0.01 radians. Details of the selection of the sectors containing the points, and the calculation of the uncertainty on these values, can be found in the Methods section of *"Clocking Auger electrons"* [102]. The corresponding time-delay, τ_{delay}, between the photo- and Auger-Meitner emission bursts can then be calculated using the observed phase shift ϕ_A and $T_{IR} = 56^{+3}_{-7}$ fs, the period of the streaking pulse:

$$\tau_{delay} = \frac{\phi_A}{2\pi} T_{IR}. \tag{4.16}$$

Applying this procedure to the distribution shown in Figure 4.4, we obtain a delay of $3.5^{+0.3}_{-0.5}$ fs. The sub-femtosecond uncertainty on this value was obtained by propagating the uncertainties on ϕ_A and T_{IR} using a standard functional approach, as detailed further in the Methods section of *"Clocking Auger electrons"* [102]. Notably, by extracting information from a large

amount of individual shots, our technique enables us to measure this delay despite using an X-ray pulse whose duration is longer. However, in this case, we must avoid using a theoretical model of Auger-Meitner decay which assumes a very short ionising pulse.

4.3.5 Evaluation of the Auger-Meitner decay lifetime

As discussed in section 4.2.2, we will apply a fully quantum-mechanical theoretical model of the Auger-Meitner emission process to interpret our measurement of the delay between photo- and Auger-Meitner emission bursts. This model of laser-assisted Auger-Meitner decay was originally developed by Kazansky, Sazhina, and Kabachnik [124], and is based on the solution of the time-dependent Schrödinger equation describing atomic ionisation by an X-ray pulse and corresponding Auger-Meitner decay in the presence of a strong laser field. A complete mathematical description can be found in the Supplementary Information of *"Clocking Auger electrons"* [102].

By calculating the delays τ_{delay} associated with a variety of possible Auger-Meitner decay lifetimes τ_A and accounting for the 7±1 fs X-ray pulse duration measured in this experiment, the quantum-mechanical model allows us to map between τ_{delay} and τ_A. This procedure led to the conclusion that the observed delay $\tau_{delay} = 3.5^{+0.3}_{-0.5}$ fs between the emission bursts corresponds to an Auger-Meitner decay lifetime $\tau_A = 2.2^{+0.2}_{-0.3}$ fs. The uncertainty on this value incorporates that on τ_{delay} and the X-ray pulse duration, which were propagated using a functional approach. Our final result for the Auger-Meitner decay lifetime is in agreement with measurements reported from spectral linewidth studies, which have found values between 2 and 2.6 fs [108, 111, 130, 131].

To illustrate the importance of the theoretical model, we have performed additional simulations with variable X-ray pulse duration. Keeping the Auger-Meitner decay lifetime fixed at the retrieved value of 2.2 fs, we increased the X-ray pulse duration from 100 attoseconds to 12 fs. The results are shown in Figure 4.6. While the observed delay is close to the Auger-Meitner decay lifetime for attosecond pulses, a significant difference appears as the ionising pulse duration increases. This difference between τ_{delay} and τ_A demonstrates the necessity of a full quantum-mechanical treatment for experiments such as this, where the exciting X-ray pulse duration is comparable to or longer than the Auger-Meitner decay lifetime.

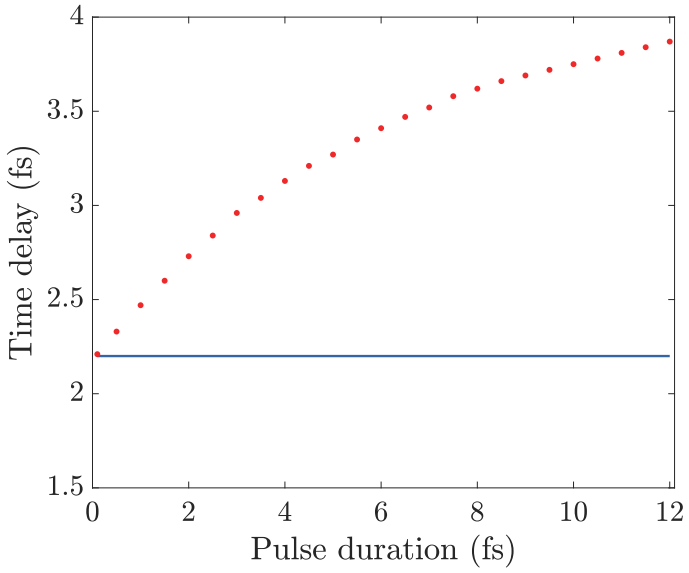

Figure 4.6: **Results of simulations showing the dependence of τ_{delay} (red points) on the exciting X-ray pulse duration (FWHM).** Each point was obtained by simulating the experiment using a comprehensive quantum-mechanical treatment. The blue solid line shows the Auger-Meitner decay lifetime $\tau_A = 2.2$ fs that was used for every simulation in this figure. This figure was adapted from Figure 4 in *"Clocking Auger electrons"* [102].

4.3.6 Conclusion and outlook

This measurement of few-femtosecond Auger-Meitner decay, which notably was performed at an XFEL, was made possible via self-referenced attosecond streaking. Following this successful demonstration of its efficacy, self-referenced streaking will enable experimentalists to take advantage of the extreme-intensity X-ray pulses at XFELs while simultaneously exploiting the unrivalled time resolution provided by attosecond streaking spectroscopy.

In conjunction with the technique, the measurement was made possible via the application of a consistent quantum model of Auger-Meitner decay [124]. The application of this more advanced model demonstrated that the older *ad hoc* two-step model significantly overestimates the extracted lifetime under the present experimental conditions. This will have major ramifications for future studies of Auger-Meitner decay, especially those applying

self-referenced streaking to make the measurement at XFELs.

Because so many highly excited states of matter relax via Auger-Meitner decay, this result may also help to inform future studies on double-core-hole spectroscopy [43–48], XFEL-pumped X-ray lasers [116, 117], and other innovative techniques dependent upon the timescales of Auger-Meitner processes. Beyond simple atomic systems, our self-referenced Auger-Meitner measurements could pave the way for investigations into the effect of a system's chemical environment on Auger-Meitner decay [132]; a comparison could, for example, be made between decay rates of carbon [107] in CF_4 and CO. Studies of Auger-Meitner decay in molecules would require high energy resolution in order to resolve structures in more complicated Auger-Meitner spectra, and the quantum model used for the interpretation of the data would need to be expanded to encompass molecular structures. Nevertheless, this is a promising avenue for future experiments. Furthermore, we expect that precise temporal characterisation of Auger-Meitner decay processes in complex systems will be crucial in interpreting diffraction and scattering patterns in single-molecule imaging experiments, where a significant proportion of Auger-Meitner electrons are known to deposit energy into molecular samples after emission [49, 133]. For example, the theoretical model verified by this experiment shows that Auger-Meitner emission is stretched over a longer duration if the exciting X-ray pulse is longer, as shown in Figure 4.6. This could mean that the onset of the majority of Auger-Meitner-induced damage during XFEL experiments with longer pulses is not as early as previously thought - it may not always be necessary to employ XFEL pulses with a duration shorter than the Auger-Meitner decay lifetime in order to outrun radiation damage.

There remains a limitation on SRAS as presented by this chapter. It employs two simultaneous streaking measurements that are made with two different phases of the streaking field; here, this phase shift was caused by the delay between the emission of photo- and Auger-Meitner electrons, during which the streaking phase advances. This form of SRAS is therefore limited to studies of phenomena involving two electron emission events, well-separated in kinetic energy and with one occurring some nonzero amount of time after the other. However, time delays are not the only source of streaking phase shifts. The next chapter will explore an alternate method of SRAS, one in which the experiment can be designed in such a way as to induce a specific desired phase shift between two streaking measurements - even when those electron emissions occur simultaneously and with the same kinetic energy.

Chapter 5

Generalising SRAS

The measurements described in Chapter 4 represent a major step forward in what can be achieved with XFELs, overcoming the limitations imposed by timing and phase jitter to make attosecond measurements using a large ensemble of individual spectra. In that first demonstration, SRAS relied upon an inherent time delay in the system of interest - the time delay between electron emissions caused them to interact with different streaking phases, and provided the constant that enables us to calculate the delay. Whilst this makes attosecond streaking spectroscopy feasible at XFELs, it is still restricted to the study of systems with two distinct electron emissions separated in time. The next step in the evolution of SRAS is to fully generalise the technique, by freeing it from these remaining constraints. This will be achieved by exploiting a position-dependent phase shift experienced by the streaking laser. In this way it will be possible to apply SRAS and its high precision to the study of any system at all existing and future XFEL facilities.

5.1 The Gouy phase shift

The Gouy phase shift is a phenomenon encountered when non-planar waves pass through their focus. As a beam of light travels along the z-axis towards its focus, it is spatially confined in the transverse x and y dimensions. According to the uncertainty principle, as its transverse position becomes more and more confined, the beam's transverse momentum must become more spread out. The Gouy phase shift was first observed by the physicist of the same name in 1890: noticing spatially-dependent changes in the diffrac-

tion pattern produced by the interference between two beams of light as one approached its focus, Louis George Gouy realised that the focusing beam's phase was changing [134]. The phase shift is relatively simple to observe and calculate, yet many competing theoretical explanations have emerged in the dozen decades since Gouy's experiment [134–137]. In 2001, an intuitive physical explanation was outlined by Feng and Winful [137], which will be the interpretation followed here. They introduce the notion of an *effective axial propagation constant*

$$\bar{k}_z = \frac{\langle k_z^2 \rangle}{k} = k - \frac{\langle k_x^2 \rangle}{k} - \frac{\langle k_y^2 \rangle}{k}, \tag{5.1}$$

where k is the wavenumber, and k_x, k_y and k_z are the wavevector components along the matching axes such that $k^2 = k_x^2 + k_y^2 + k_z^2$. Angular brackets here denote their contents' expectation value as follows, with $f(\delta)$ representing the distribution of some variable δ:

$$\langle \delta \rangle = \frac{\int_{-\infty}^{\infty} \delta \left| f(\delta) \right|^2 d\delta}{\int_{-\infty}^{\infty} \left| f(\delta) \right|^2 d\delta}. \tag{5.2}$$

The effective axial propagation constant $\bar{k}_z$ determines the rate of change of the light field's phase according to

$$\bar{k}_z = \frac{\partial \phi(z)}{\partial z}. \tag{5.3}$$

Any spread in the transverse momenta - such as in the case of a Gaussian beam - reduces $\bar{k}_z$, so that the axial rate of phase change is lower. Note that for a plane wave, the transverse momentum components are zero; according to equation (5.1), $\bar{k}_z = k$ in this case, and hence equation (5.3) collapses to the simple definition of the wavenumber $k = \frac{\partial \phi(z)}{\partial z}$: plane waves do not undergo a Gouy phase shift. Indeed, the shift can be considered as the reduction in phase advance of a non-planar wave compared to a planar one. As such, Feng and Winful define the Gouy phase shift as

$$\phi_G = -\frac{1}{k} \int^{z} \left(\langle k_x^2 \rangle + \langle k_y^2 \rangle \right) dz. \tag{5.4}$$

Evaluating the integral for a Gaussian beam leads to an expression for the Gouy phase shift as a function of distance along the z-axis. It is equal to

$$\phi_G(z) = -\arctan\left(\frac{z - z_0}{z_R}\right), \tag{5.5}$$

where z_0 and z_R are the transverse position of the beam's focus and its Rayleigh length, respectively. The latter is given by

$$z_R = \frac{\pi w_0^2}{\lambda}, \tag{5.6}$$

where λ is the wavelength of the light, and w_0 is the beam's radius at the focus, referred to as the beam waist. Knowing equation (5.5) and the relevant beam parameters, we can calculate the phase shift at any position along the z-axis, as shown in Figure 5.1.

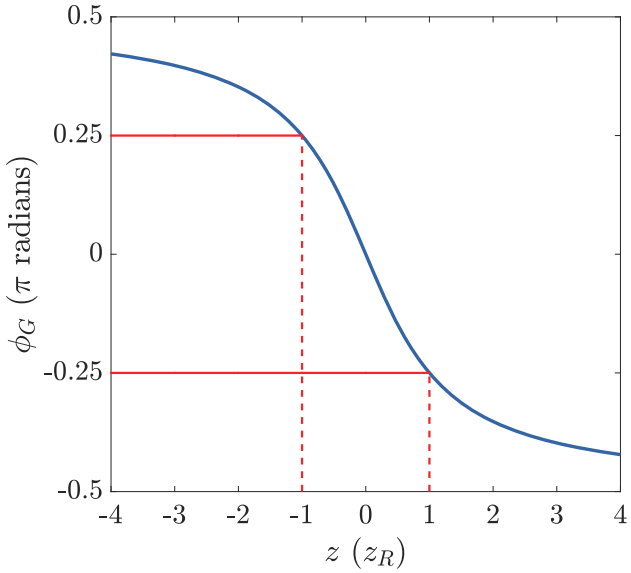

Figure 5.1: **The Gouy phase shift.** The blue curve is the Gouy phase shift ϕ_G as a function of position z, for a Gaussian beam focused at $z = 0$. The vertical red dotted lines highlight the z-positions one Rayleigh length z_R from the focus, whilst the horizontal red lines highlight the Gouy phase shift at each of these positions.

In effect, the Gouy phase shift provides a means for the manipulation and control of the phase of the light field depending where on the z-axis we make our measurements. This is extremely useful for the broader application

of SRAS, which requires a light phase shift to occur between two distinct streaking measurements. In section 4.3, this phase shift occurred due to the delay between the emission of photo- and Auger-Meitner electrons, which were measured with a single TOF detector. Due to the light phase's evolution over time, the two types of electrons interacted with a different streaking phase. The delay time, however, is a fundamental property of the system being studied, and is therefore not something we can control in order to optimise our experiment.

The Gouy phase shift, in contrast, is a function not of time but of position, and hence we can exploit it by making our measurements at different points along the z-axis. If we perform an experiment with two TOF detectors, streaking and measuring electrons at two positions with the same XFEL-streaking pulse pair, we will observe a streaking phase shift between each pair of measurements, as for the photo- and Auger-Meitner electrons in section 4.3. And because we know the Gouy phase shift ϕ_G from equation (5.5), we can precisely calculate how much the phase advanced due to a time delay in the system - even where that delay is much shorter than those required for single-TOF SRAS. The Gouy phase shift will even allow SRAS to be applied to two distinct measurements of the same type of electrons; for example, streaking photoelectrons at two positions along the z-axis could enable SRAS to be used for precise and non-invasive XFEL pulse characterisation.

5.2 Two-TOF SRAS in neon gas

The first proof-of-principle two-TOF SRAS experiments have been performed and will be described in this section. A schematic diagram of the experimental setup is shown in Figure 5.2. It is not dissimilar to that used for the single-TOF SRAS experiments of section 4.3, differing only in select aspects. The most immediately apparent difference is the addition of a second TOF detector. The approach also necessitates a unique gas injection needle with an output for each measurement position. The detectors and gas samples are positioned such that each lies approximately one Rayleigh length from the beam's focus; according to equation (5.5), the resultant Gouy phase shift will be around $\frac{\pi}{2}$ radians.

X-ray FEL pulses with 1030 eV photon energy ionise the neon gas as it emerges from the dual gas needles. Upon escaping their parent atoms, photoelectrons are streaked by an MIR streaking pulse with 14 µm wavelength.

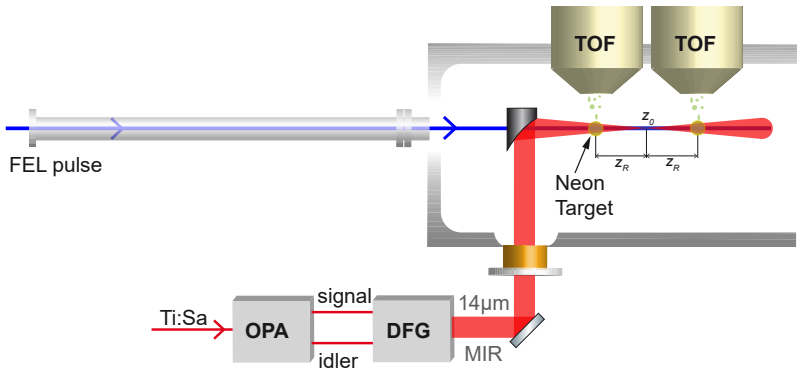

Figure 5.2: **Two-TOF SRAS apparatus.** 14-μm MIR and 1030-eV FEL pulses are directed into a neon gas target in a setup resembling that of Figure 4.3. Unlike in that experiment, this apparatus features two target interaction regions and two TOF detectors, each positioned approximately one Rayleigh length z_R from the MIR focus at z_0. Thus, two distinct measurements are recorded for each FEL-MIR pulse pair.

The kinetic energies of the photoelectrons are measured by each detector as in section 4.3, except that in this case two photoemission measurements are performed simultaneously with each FEL-streaking pulse pair. Because the two target regions lie at different positions along the z-axis, the Gouy phase shift differs between them, and the two detectors collect sets of electrons that interacted with a different streaking phase - analogous to how the photo- and Auger-Meitner electrons in section 4.3 interacted with different streaking phases.

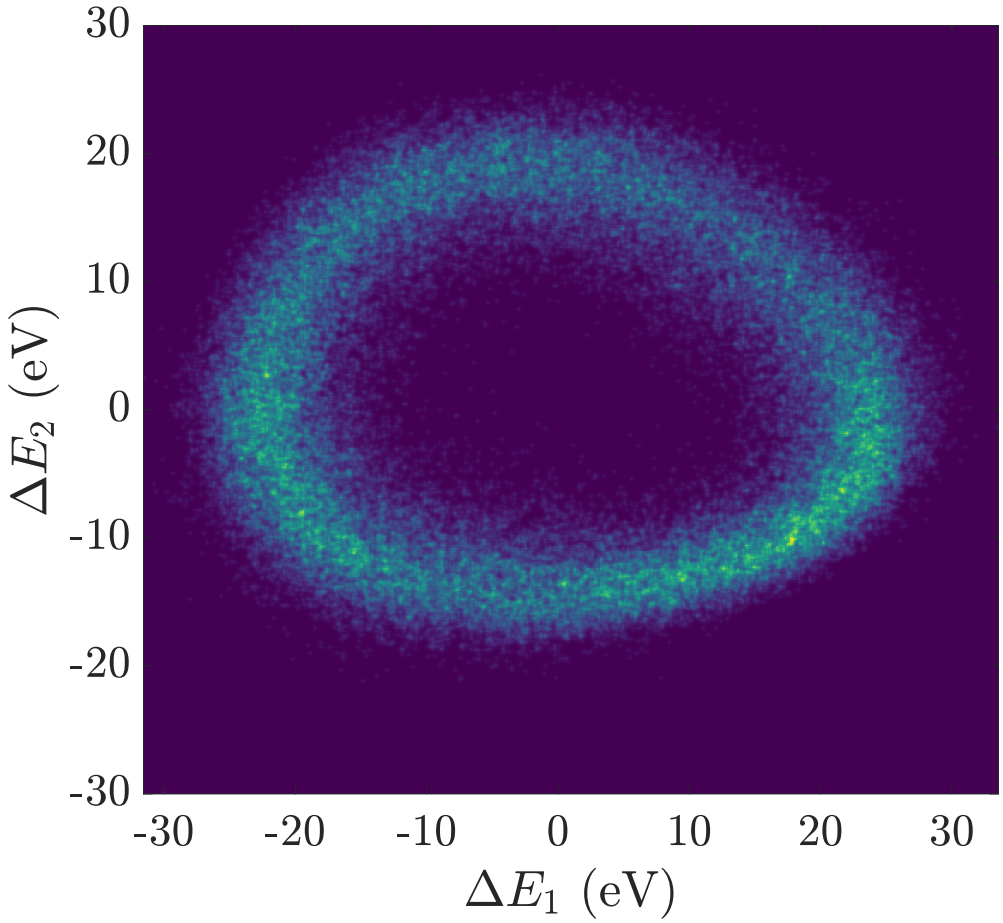

Figure 5.3: **Two-TOF self-referenced attosecond streaking.** Photoemission is induced in neon gas by 1030-eV XFEL pulses and the photoelectrons are streaked by a 14-µm laser pulse. Two electron TOF detectors measure the final kinetic energy of the streaked electrons, which differs along the beam's axis of propagation due to the Gouy phase shift. The coordinate axes ΔE_1 and ΔE_2 are the kinetic energy measured by the upstream and downstream detectors respectively.

Figure 5.3 shows the distribution of final kinetic energies of photoelectrons collected by each detector. It bears a strong resemblance to Figure 4.4, but in this case the phase shift is significantly larger. For each pair of measurements, these photoelectrons were emitted as a result of interaction with the same FEL pulse, and streaked by the same laser pulse, so it is remarkable that we

can perform SRAS as if they occurred at different times.

5.2.1 Global analysis

Before examining individual measurements out of the thousands in Figure 5.3, there are some experimental parameters that can be calculated using the entire ensemble of data points. This section will employ some techniques similar to those used in section 4.3, and some additional methods that are adapted to the two-detector case.

5.2.1.1 X-ray pulse duration

The correlation plot in Figure 5.3 can straightforwardly be used to calculate the X-ray pulse duration and other diagnostic parameters following a similar procedure to the one described in section 4.3.2. Once again, it is simple to identify those measurements which were made using a zero-crossing of the streaking vector potential; for the upstream detector 1, these lie near the line $\Delta E_1 = 0$, and for the downstream detector 2 they lie near $\Delta E_2 = 0$. For this calculation, zero-crossing measurements were defined as those within 0.75 eV of the relevant axis, which is sufficient to include enough data for the calculation without beginning to include measurements made far from the zero-crossing.

The average field-free width of the photoemission peak is 5.0 ± 0.6 eV and 6.9 ± 0.9 eV on detectors 1 and 2 respectively, and when broadened by the zero-crossing of the streaking field, these peak widths increase to 12 ± 2 eV and 10 ± 2 eV. The quantities used in the pulse duration calculation are normally-distributed and these and the following uncertainties are the standard deviations of each quantity. The larger measured field-free bandwidth on detector 2 is likely due to its poorer resolution, whilst the increased broadening on detector 1 may be due to its position along the z-axis, which will be discussed further in section 5.2.1.4. The zero-crossing streaking speeds are 3.0 ± 0.2 eV/fs on detector 1 and 2.3 ± 0.2 eV/fs on detector 2; the difference in magnitude will also be addressed in section 5.2.1.4. The average FWHM pulse duration is 8 ± 2 fs and 8^{+4}_{-5} fs on detectors 1 and 2 respectively, and therefore the overall average is 8^{+2}_{-3} fs.

5.2.1.2 X-ray pulse chirp

It is also possible to quantify chirp in the X-ray pulse. If the X-ray pulse is chirped, the resultant burst of photoelectrons will have initial kinetic energies that depend on their time of emission. Thus, the photoemission peak will experience different amounts of broadening when exposed to streaking vector potentials with differently-signed slopes, which can be verified by looking at opposite sides of the oval in Figure 5.3.

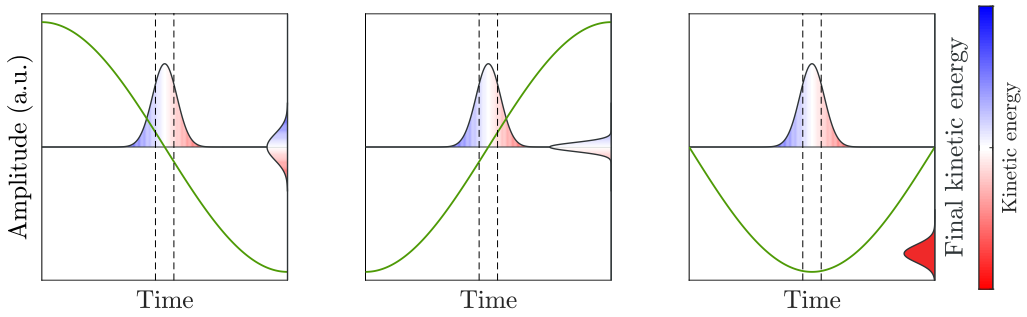

Figure 5.4: **The effect of chirp in streaking experiments.** Each plot shows a stylised depiction of a streaking experiment with different streaking phase. The central peaks in each plot represent the X-ray pulse which induces photoemission. The colourmap shows the initial kinetic energy of the electrons emitted by each part of the X-ray pulse, with lower kinetic energies in red and higher in blue, and the green line represents the streaking vector potential with which these electrons interact – the left, centre, and right panels show the result of negative-sloped, positive-sloped, and minimal vector potentials respectively. The black dotted lines highlight the parts of the streaking vector potential with which the photoelectrons interact. On the right-hand axis, the final distribution of kinetic energies is shown.

The concept is illustrated in Figure 5.4. The panels of the figure show the effects of different streaking vector potentials upon photoelectrons released by a negatively-chirped X-ray pulse – the early part of the X-ray pulse has a higher photon energy than the latter, and this is reflected in the initial kinetic energy distribution of the photoelectrons. The left-hand panel shows a zero-crossing of the streaking vector potential with a negative slope. Upon interaction with the streaking pulse, the early higher-energy electrons have their kinetic energy increased, whilst the later-emitted slower electrons

are decelerated by a negative streaking vector potential. The final result is shown on the vertical axis: in this case, there is significant broadening induced by the streaking laser, which only exacerbates the existing distribution of photoelectron kinetic energies. Conversely, when interacting with a positively-sloped streaking vector potential as in the centre panel, the measured peak may instead be narrowed. The right-hand panel shows the result of interaction with a trough in the streaking vector potential: the peak is somewhat broadened, but most noticeably, it experiences a large change in its central kinetic energy.

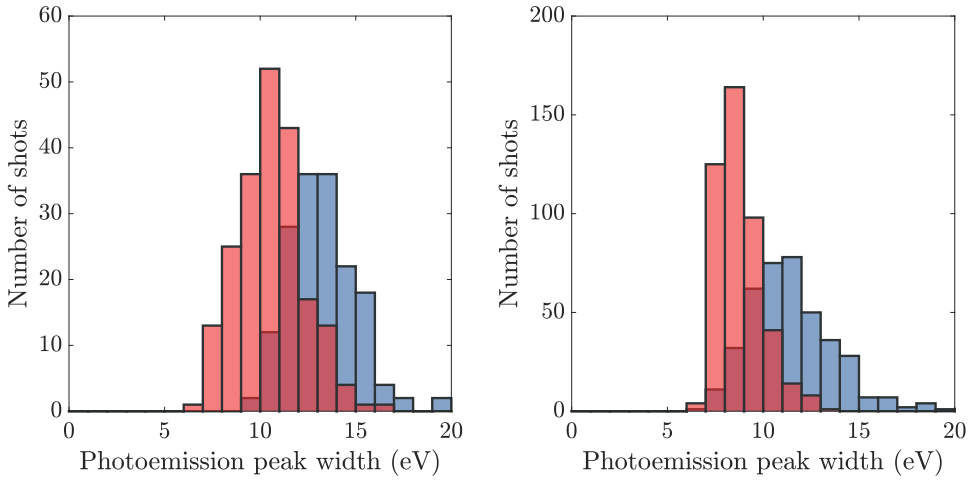

Figure 5.5: **Broadening due to a chirped photoelectron distribution.** Histograms of the photoemission peak r.m.s. widths at positively (red) and negatively (blue) sloped zero-crossings of the streaking field. The left and right panels correspond to detector 1 and 2 respectively.

Comparing the result of interaction with different zero-crossings, therefore, can provide insight regarding the average chirp in the FEL pulse. The negatively-sloped zero-crossings correspond to measurements at the top and left of Figure 5.3 for detector 1 and 2 respectively, and measurements made with the corresponding positively-sloped zero-crossings are located on the opposite sides. The distribution of bandwidths at each zero-crossing is shown in Figure 5.5. The photoemission peak was broader at negatively sloped zero-crossings, an indicator of negative chirp in the X-ray pulse. The FEL

chirp, assuming it is linear, is given by

$$c = \frac{\sigma_+^2 - \sigma_-^2}{4s\tau_X^2}, \tag{5.7}$$

where σ_+ and σ_- correspond to the average broadened peak widths at positive- and negatively sloped zero-crossings respectively. For these data, using the same zero-crossing measurements as in section 5.2.1.1, the average chirp is $-0.1^{+0.2}_{-0.3}$ eV/fs on detector 1. The uncertainty on this measurement is sensitive to detector resolution, and the calculated chirp from detector 2 has too large an uncertainty to be useful.

5.2.1.3 Calculating the Gouy phase shift

We can use the thousands of pairs of measurements shown in Figure 5.3 to directly measure the Gouy phase shift between the two detectors. It is given, as a function of position z along the beam's axis of propagation, by equation (5.5):

$$\phi_G(z) = -\tan^{-1}\left(\frac{z - z_0}{z_R}\right).$$

With two detectors making measurements simultaneously, we will measure the difference in Gouy phase shift between them, given by

$$\Delta\phi_G(z_1, z_2) = \phi_G(z_1) - \phi_G(z_2), \tag{5.8}$$

where indices 1 and 2 refer to upstream and downstream detectors respectively, so that detector n is at position z_n.

It is clear that equation (5.8) is not injective; there are a wide variety of combinations of TOF positions that can lead to a given difference in phase shifts $\Delta\phi_G$. However, with an asymmetric set-up, the streaking field amplitude will be higher beneath the TOF that is closer to the beam focus, resulting in a larger streaking effect. Under typical experimental conditions, therefore, the positions of the detectors can be tuned to induce a specific desired phase shift and relative streak strength.

We aim to set up the two detectors such that the streaking laser experiences a Gouy phase shift $\Delta\phi_G$ of approximately $\frac{\pi}{2}$ as it passes from one TOF to the next. This parametric shift in the x and y components of the distribution in Figure 5.3 results in the widest ellipse and will give our measurements the highest sensitivity.

The sine argument ϕ_i in equation (3.9) will be reduced by $\Delta\phi_G$ for the second set of electrons, so the spectrum acquired further downstream will be shifted in kinetic energy by a different amount compared the spectrum from the upstream detector. According to equation (3.9), the change in kinetic energy felt by each burst of photoelectrons is proportional to the factor $\sqrt{8W_{el}U_p}$. The ponderomotive potential U_p is proportional to the square of the streaking laser's electric field strength, which itself is dependent upon each TOF's proximity to the beam focus - so U_p may differ at each TOF. Explicitly,

$$\begin{aligned} \Delta E_1 &\approx \sin(\phi_i)\sqrt{8W_1U_1}, \\ \Delta E_2 &\approx \sin(\phi_i - \Delta\phi_G)\sqrt{8W_2U_2}, \end{aligned} \tag{5.9}$$

where the subscripts in W_n and U_n refer to the field-free kinetic energy and ponderomotive potential respectively at detector n. In this experiment, we measure 1s photoelectrons at both detectors, and therefore $W_1 = W_2$, but the forthcoming analysis remains simple even in the general case where $W_1 \neq W_2$. Our goal is to calculate the value of $\Delta\phi_G$ from these equations and our measured quantities ΔE_n. We begin by defining the ratio

$$F(\phi_i, \Delta\phi_G) = \frac{\Delta E_2\sqrt{W_1}}{\Delta E_1\sqrt{W_2}}, \tag{5.10}$$

which, substituting equations (5.9), is equal to

$$F(\phi_i, \Delta\phi_G) = \sqrt{\frac{U_2}{U_1}}\frac{\sin(\phi_i - \Delta\phi_G)}{\sin(\phi_i)} = \sqrt{\frac{U_2}{U_1}}\left[\cos(\Delta\phi_G) - \sin(\Delta\phi_G)\cot(\phi_i)\right] \tag{5.11}$$

using the trigonometric identity

$$\sin(\phi_i - \Delta\phi_G) \equiv \sin(\phi_i)\cos(\Delta\phi_G) - \cos(\phi_i)\sin(\Delta\phi_G). \tag{5.12}$$

The formulation in equation (5.10) can be calculated directly from the data for every pair of measurements ΔE_1 and ΔE_2, resulting in a characteristic distribution that is dependent upon the phase shift $\Delta\phi_G$. Equation (5.11) is a function of this phase shift and also of the randomly-varying streaking phase ϕ_i. Because ϕ_i varies randomly, across thousands of shots its entire range will be included in the experiment, which enables us to calculate the

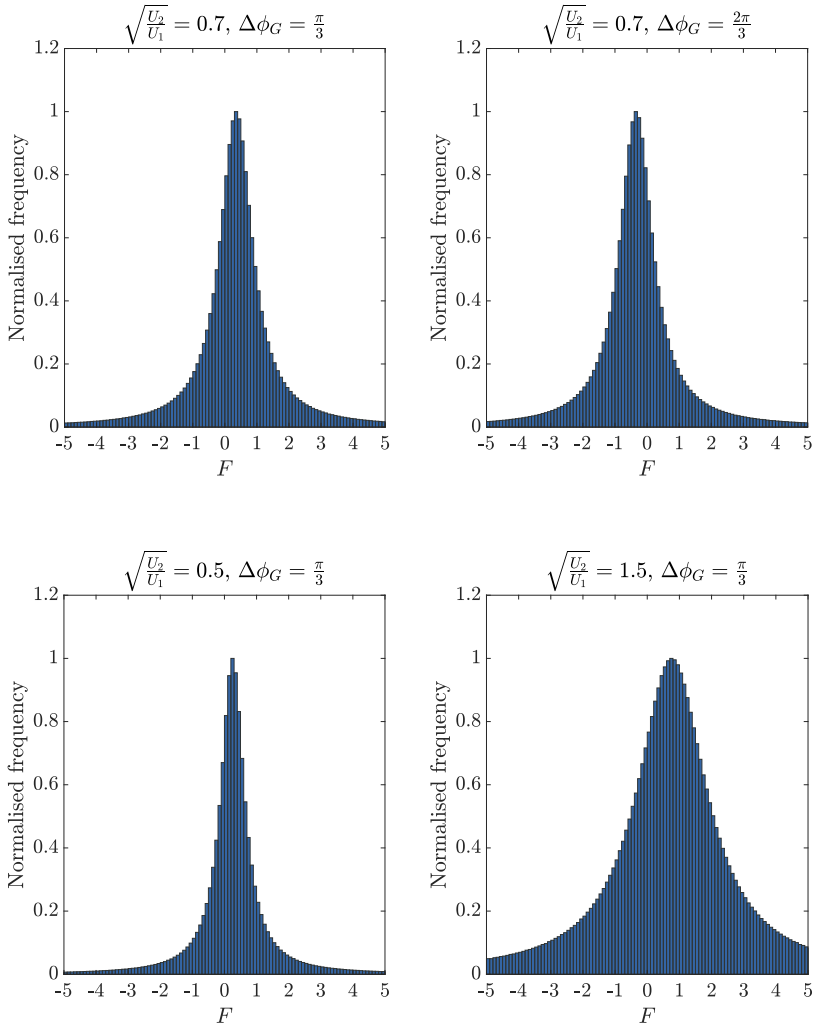

Figure 5.6: **Simulated distributions of F.** Four example distributions of the quantity F in equation (5.11), simulated with different combinations of the parameters $\sqrt{\frac{U_2}{U_1}}$ and $\Delta\phi_G$. In the top row, $\sqrt{\frac{U_2}{U_1}}$ is held constant, with examples shown for two values of $\Delta\phi_G$; the converse is true in the bottom row.

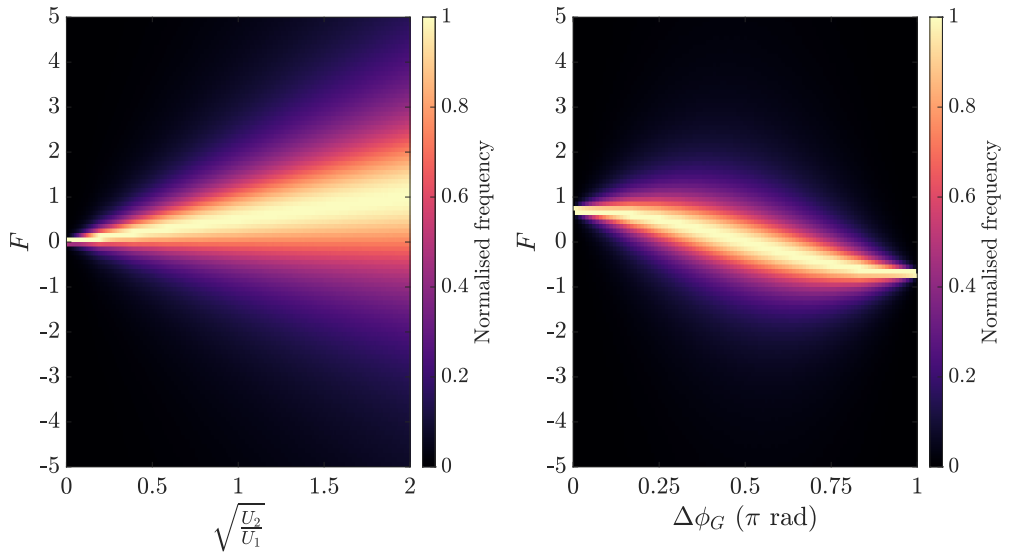

Figure 5.7: F **as a function of** $\sqrt{\frac{U_2}{U_1}}$ **and** $\Delta\phi_G$**.** The left-hand panel shows the change in F as a function of $\sqrt{\frac{U_2}{U_1}}$ for a fixed value of $\Delta\phi_G = \frac{\pi}{3}$, whilst the right-hand panel shows F as a function of $\Delta\phi_G$ for a fixed $\sqrt{\frac{U_2}{U_1}} = 0.7$.

expected shape of the distribution computationally. Some example distributions for different values of $\Delta\phi_G$ and $\sqrt{\frac{U_2}{U_1}}$ are shown in Figure 5.6.

The $\cot(\phi_i)$ term in equation (5.11) will, when ϕ_i varies randomly, have a Lorentzian distribution centred at zero. The other terms will modify the distribution's shape: the centre will shift to $\sqrt{\frac{U_2}{U_1}}\cos(\Delta\phi_G)$, whilst the width will be multiplied by a factor of $\left|\sqrt{\frac{U_2}{U_1}}\sin(\Delta\phi_G)\right|$. Indeed, the specific combination of $\Delta\phi_G$ and $\sqrt{\frac{U_2}{U_1}}$ will uniquely determine the shape and position of the distribution. This is illustrated in Figure 5.7; the left-hand panel shows that both the width and the centre of the distribution increase linearly with $\sqrt{\frac{U_2}{U_1}}$, while the right-hand panel shows the more complicated relationship between the distribution's shape and $\Delta\phi_G$.

Here, it is important to note that $\sqrt{\frac{U_2}{U_1}}$ is a function of the positions of the two TOFs. If the experiment is set up with exact symmetry, this factor

will be equal to 1. In other cases, we can measure it and the Gouy phase shift by measuring the centre and width of the distribution.

Based on Figure 5.7 and equation (5.11), we can see that a distribution centred around 0 is only possible under one of three circumstances: either $\sqrt{\frac{U_2}{U_1}} \approx 0$, $\Delta\phi_G \approx \frac{\pi}{2}$, or both[1]. Since $\sqrt{\frac{U_2}{U_1}} \approx 0$ is unphysical, implying one detector situated an infinite distance from the laser focus, a measured distribution of F that is centred at 0 is a strong indicator of a $\frac{\pi}{2}$ Gouy phase shift between the two detectors.

In order to identify $\sqrt{\frac{U_2}{U_1}}\cos(\Delta\phi_G)$ and $\left|\sqrt{\frac{U_2}{U_1}}\sin(\Delta\phi_G)\right|$, we can numerically fit a function to the distribution calculated from the data and compare it to a fit of the distribution of $\cot(\phi_i)$. Figure 5.8 shows both these distributions, overlaid with the numerically-determined fits. The unmodified distribution of $\cot(\phi_i)$ is identical to the case where $\sqrt{\frac{U_2}{U_1}} = 1$ and $\Delta\phi_G = \frac{\pi}{2}$, which can be seen from equation (5.11).

The two datasets are sorted into uniform bins and the number of points in each bin is extracted as a function of F. This provides two curves, one for the calculated values of F from the experiment, and one for the values in the $\sqrt{\frac{U_2}{U_1}} = 1$ and $\Delta\phi_G = \frac{\pi}{2}$ case. A standard nonlinear least-squares fitting algorithm is applied, optimising the parameters a, b, and c in the following function:

$$f(x) = \frac{a}{\pi}\left(\frac{\frac{1}{2}b}{(x-c)^2 + \left(\frac{1}{2}b\right)^2}\right). \tag{5.13}$$

Equation (5.13) is the probability density function of a Lorentzian distribution, with a, b, and c together determining its amplitude, width, and centre. The amplitude of this function is equal to $\frac{2a}{\pi b}$; since this is determined by two of the fitting parameters, we first normalise both curves by dividing both by the peak of the $\cot(\phi_i)$ curve. In this way the scaling parameter a can be fixed and the widths b of each distribution can be directly compared. The parameters for both fits, along with their 95% confidence intervals, are summarised in the table below.

[1]There are actually infinite solutions with $\Delta\phi_G \approx (2n+1)\frac{\pi}{2}, n \in \mathbb{Z}$, but even if the detectors were placed at $z_1 = -\infty$ and $z_2 = \infty$, the maximum possible difference in Gouy phase shift between them is $\Delta\phi_G(-\infty, \infty) = \pi$. This can be seen from equations (5.5) and (5.8). We also know that $\Delta\phi_G > 0$ since $z_2 > z_1$, so the only value of $\Delta\phi_G$ that can result in a distribution of F centred around 0 is $\Delta\phi_G \approx \frac{\pi}{2}$.

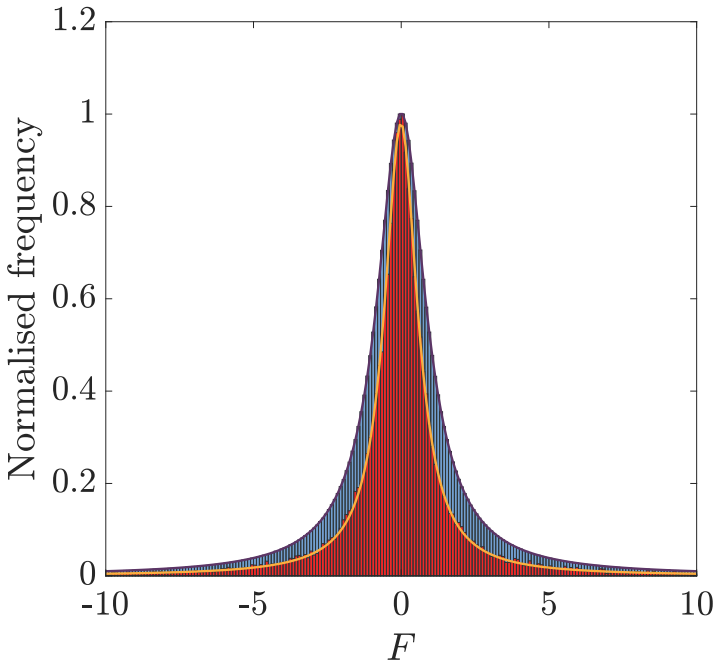

Figure 5.8: **Lorentzian fits of F.** The red and blue histograms correspond respectively to the measured distribution of F, and an unmodified distribution of $\cot(\phi_i)$. The orange and purple lines show the corresponding Lorentzian least-square fits.

	$\cot(\phi_i)$		$\frac{\Delta E_2\sqrt{W_1}}{\Delta E_1\sqrt{W_2}}$	
	Value	Interval	Value	Interval
a	3.152	$(3.151, 3.153)$	3.152 (fixed)	N/A
b	2.002	$(2.001, 2.002)$	1.38	$(1.376, 1.384)$
c	0	$(-0.2255, 0.2078)\times10^{-3}$	-8.817×10^{-3}	$(-10.81, -6.828)\times10^{-3}$

The fit of the measured (red) distribution in Figure 5.8 has a width equal to $\left|\sqrt{\frac{U_2}{U_1}}\sin(\Delta\phi_G)\right| = 0.69$ times the width of the unmodified (blue) distribution, and it is centred at $\sqrt{\frac{U_2}{U_1}}\cos(\Delta\phi_G) = -9\times10^{-3}$. Despite the width being determined by the absolute value of $\sqrt{\frac{U_2}{U_1}}\sin(\Delta\phi_G)$, we also know from equations (5.5) and (5.8) that $\Delta\phi_G > 0$, because $z_2 > z_1$. The solution to

these equations is therefore $\sqrt{\frac{U_2}{U_1}} = 0.690 \pm 0.002, \Delta\phi_G = 1.558 \pm 0.003$ rad, where the uncertainties have been calculated using the 95% confidence intervals of b and c.

These results have extremely low uncertainty because of the many thousands of measurements used to generate the distribution of F, averaging out some single-measurement errors and enabling the least-squares fitting algorithm to converge to an accurate solution. Nevertheless, it should be noted that there are additional sources of uncertainty, most notably photon energy jitter, which add errors to each individual measurement $(\Delta E_1, \Delta E_2)$, and have not been accounted for in this estimate. Since energy jitter is normally-distributed, calculating F from many thousands of measurements for these calculations should alleviate its impact; however, more experiments will be required to unequivocally quantify the impact of energy jitter and other single-measurement errors on the accuracy of this result. As will be discussed later, it is expected that future experiments can account and even correct for energy jitter, perhaps entirely negating the need to incorporate it into error analysis. The rest of the calculations in this section will proceed using the present error analysis, but these values should be thought of as lower bounds for the achievable uncertainty.

5.2.1.4 Determining the TOF positions

Knowing the phase shift and scaling factor enables us to precisely confirm the position of the two TOFs. The experiment was designed to have each detector one Rayleigh length from the streaking laser focus, but there are significant experimental challenges involved with arranging the detectors so precisely. Instead, it is relatively simple to arrange the detectors such that the Gouy phase shift is close to $\frac{\pi}{2}$ - which can be swiftly confirmed with online analysis using a plot like Figure 5.3 - and calculate the exact positions after the experiment.

As the streaking laser pulse passes through and beyond its focus, its intensity - and therefore electric field strength - changes with the spot size of the beam. The beam radius is given by

$$w(z) = w_0 \sqrt{1 + \left(\frac{z}{z_R}\right)^2}, \tag{5.14}$$

where w_0 is the beam radius at the focus, z is the position along its axis of

propagation, and z_R is the beam's Rayleigh range. The intensity of the laser evolves along the z-axis according to

$$I(z) = I_0 \left(\frac{w_0}{w(z)} \right)^2 = \frac{I_0}{1 + \left(\frac{z}{z_R} \right)^2}, \tag{5.15}$$

where I_0 is the maximal laser intensity at its focus. The electric field amplitude $E_0(t)$ at position z is proportional to $\sqrt{I(z)}$; the ponderomotive potential is therefore directly proportional to $I(z)$, which can be seen from equation (3.3):

$$U_p = \frac{e^2 E_0^2}{4 m_e \omega^2}.$$

Let z_n, W_n and U_n be the position, field-free kinetic energy, and ponderomotive potential at detector n respectively. Expressing the known ratio $\sqrt{\frac{U_2}{U_1}}$ in terms of the intensity from equation (5.15):

$$\sqrt{\frac{U_2}{U_1}} = \sqrt{\frac{I(z_2)}{I(z_1)}} = \sqrt{\frac{I_0 \left(1 + \left(\frac{z_1}{z_R} \right)^2 \right)}{I_0 \left(1 + \left(\frac{z_2}{z_R} \right)^2 \right)}}. \tag{5.16}$$

We can simplify this expression by expressing the detector positions z_n as multiples of z_R. Define a pair of constants d_n such that

$$z_n \equiv d_n z_R \tag{5.17}$$

and substitute them into equation (5.16), so that

$$\sqrt{\frac{U_2}{U_1}} = \sqrt{\frac{I_0 \left(1 + \left(\frac{d_1 z_R}{z_R} \right)^2 \right)}{I_0 \left(1 + \left(\frac{d_2 z_R}{z_R} \right)^2 \right)}} \tag{5.18}$$

$$\iff \sqrt{\frac{U_2}{U_1}} = \sqrt{\frac{1 + d_1^2}{1 + d_2^2}} \tag{5.19}$$

$$\implies \|d_1\| = \sqrt{\frac{U_2}{U_1}(1 + d_2^2) - 1}. \tag{5.20}$$

Equation (5.17) and equation (5.20) will allow us to identify the position of one detector provided we know that of the other. We can therefore identify a pair of detector positions that satisfy both our known constraints: the ratio $\sqrt{\frac{U_2}{U_1}}$ in equation (5.20) must equal 0.690, and the Gouy phase shift $\Delta\phi_G$ occurring between these two positions must equal 1.558 radians according to equation (5.8).

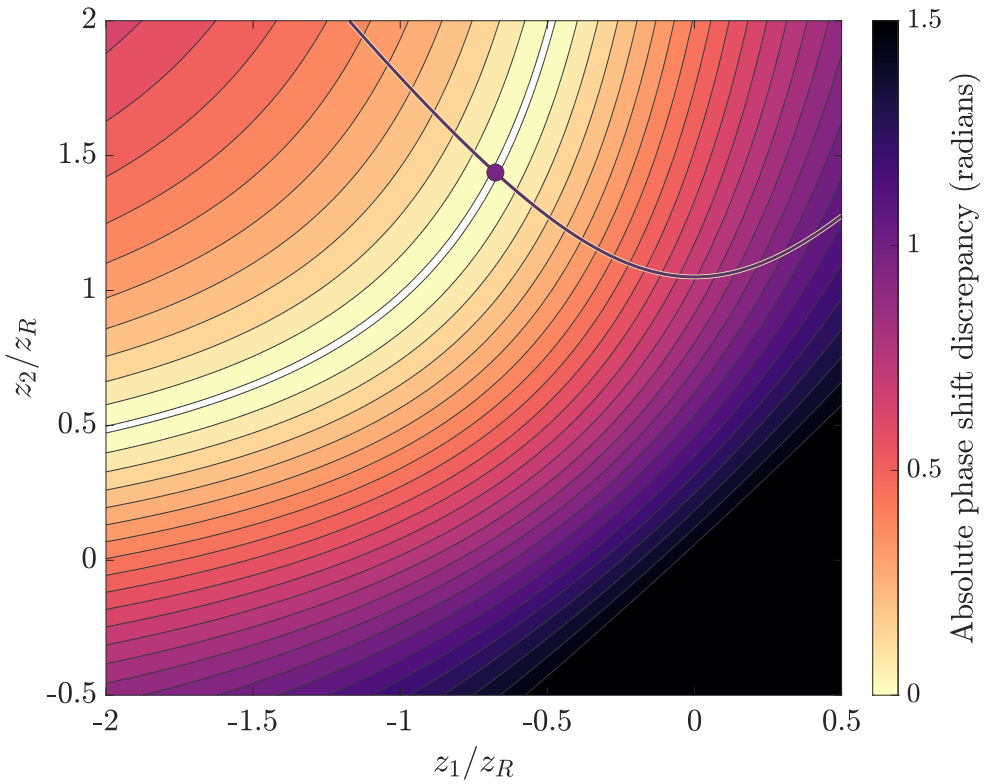

Figure 5.9: **Experimental Geometry.** The contour plot displays, as a function of TOF positions z_1 and z_2, the absolute discrepancy between the induced Gouy phase shift and that measured from our data. Pairs of positions leading to discrepancies less than 0.01 radians are shown in white, and pairs with discrepancies greater than or equal to 1.5 radians are shown in black. The purple line shows the (z_1, z_2) combinations that are compatible with the streaking ratio $\sqrt{\frac{U_2}{U_1}}$ measured in the experiment, and the purple circle highlights the single pair of positions that satisfies both criteria.

Whilst there are infinite combinations of detector positions that can lead to any particular phase shift *or* scaling factor, the specific combination of *both* values can only be achieved with a specific arrangements of detectors. This is illustrated in Figure 5.9. The regions of (z_1, z_2)-space that result in the measured Gouy phase shift are shown in white on the contour plot. The purple line shows the (z_1, z_2) pairs that would satisfy equation (5.20) with the measured value of $\sqrt{\frac{U_2}{U_1}}$. The point at which the line intersects the white region is, therefore, the only combination of z_1 and z_2 that can lead to the parameters recorded in the experiment.

We can thus determine that the first TOF was $d_1 = 0.677 \pm 0.005$ Rayleigh lengths upstream of the focus, whilst the second was $d_2 = 1.438 \pm 0.008$ Rayleigh lengths downstream of it. The uncertainties on these values have been calculated using a functional approach, propagating the uncertainties on $\sqrt{\frac{U_2}{U_1}}$ and $\Delta\phi_G$. It is notable that self-referenced streaking is not dependent on an idealised symmetric experimental set-up with $|z_1| = |z_2|$; in fact, the two simultaneous measurements enable the experimental geometry to be precisely measured and accounted for, as demonstrated here.

5.2.2 Single-shot streaking parameters

The XFEL experiments described in this thesis consist of thousands of individual measurements, each one associated with a single X-ray-streaking pulse pair, or 'shot'. In addition to the foregoing calculations, which are made using many averaged measurements, an ideal two-TOF SRAS setup enables single-shot parameters to be identified. This section will detail how SRAS could advance further, using the correlation plot to obtain the streaking amplitude and phase for every shot in the experiment. The experiment performed in this thesis can already provide a wealth of single-shot information, limited only by a lack of diagnostic measurements and metadata that will be straightforward to include in future experiments.

5.2.2.1 Streaking phase

We can begin by identifying the carrier-envelope phase ϕ_{CEP} of each streaking laser pulse. First of all, we transform the data to polar coordinates:

$$r = \sqrt{\Delta E_1^2 + \Delta E_2^2}, \qquad \theta = \tan^{-1}\left(\frac{\Delta E_2}{\Delta E_1}\right). \tag{5.21}$$

Substituting equations (5.9) for ΔE_1 and ΔE_2 into the equation for θ shows that

$$\tan(\theta) = \sqrt{\frac{W_2 U_2}{W_1 U_1}}\left[\frac{\sin(\phi_i)\cos(\Delta\phi_G) - \cos(\phi_i)\sin(\Delta\phi_G)}{\sin(\phi_i)}\right] \tag{5.22}$$

$$\implies \tan(\phi_i) = \frac{-\sin(\Delta\phi_G)}{\sqrt{\frac{W_1 U_1}{W_2 U_2}}\tan(\theta) - \cos(\Delta\phi_G)} \tag{5.23}$$

$$\implies \phi_i = \tan^{-1}\left(\frac{-\sin(\Delta\phi_G)\Delta E_1}{\sqrt{\frac{W_1 U_1}{W_2 U_2}}\Delta E_2 - \cos(\Delta\phi_G)\Delta E_1}\right), \tag{5.24}$$

where for the final expression we have made use of the definition of $\tan(\theta)$ from equation (5.21). A four-quadrant inverse tangent function will take into account the signs of the numerator and denominator in equation (5.24), which together place each data point $(\Delta E_1, \Delta E_2)$ in a specific quadrant.

This measured phase ϕ_i represents the argument of the sine term in equation (5.9). This parameter is not only a function of the randomly-varying streaking CEP, but also of the relative arrival times of the two pulses. The arrival time directly determines the amplitude of the streaking pulse with which the photoelectrons interact; since the oscillating electric field is also time-dependent, arrival time also has an effect on the phase of the field that interacts with the electrons. The quantity ϕ_i, therefore, satisfies

$$\phi_i = \omega t_i + \phi_{CEP}, \tag{5.25}$$

where $\phi_{CEP} \in [0, 2\pi)$ represents the random modulation of the streaking laser's CEP. To fully ascertain the streaking laser parameters, we must additionally calculate t_i, which will allow us to identify ϕ_{CEP} using equation (5.25), and uniquely describe the streaking conditions for every measurement in the experiment.

5.2.2.2 Arrival time

The radial coordinate r is related to the streaking pulse amplitude - and hence, the relative arrival time of the XFEL pulse. From equations (5.9) and

(5.21) we can see that

$$r = \sqrt{8W_1U_1\sin^2(\phi_i) + 8W_2U_2\sin^2(\phi_i - \Delta\phi_G)} \tag{5.26}$$

$$\implies r^2 = 8W_1U_1\sin^2(\phi_i) + 8W_2U_1\sqrt{\frac{U_2}{U_1}}^2\sin^2(\phi_i - \Delta\phi_G), \tag{5.27}$$

where we have substituted the unknown U_2 for $U_1\sqrt{\frac{U_2}{U_1}}^2$, since the ratio $\sqrt{\frac{U_2}{U_1}}$ is already known. Solving for U_1,

$$r^2 = 8U_1\left(W_1\sin^2(\phi_i) + W_2\sqrt{\frac{U_2}{U_1}}^2\sin^2(\phi_i - \Delta\phi_G)\right) \tag{5.28}$$

$$\implies U_1 = \frac{r^2}{8\left(W_1\sin^2(\phi_i) + W_2\sqrt{\frac{U_2}{U_1}}^2\sin^2(\phi_i - \Delta\phi_G)\right)}. \tag{5.29}$$

Equation (5.29), in conjunction with equations (5.21) and (5.24), allows us to calculate U_1 for every measurement. Since the detector and focus positions are fixed, we need only multiply U_1 by the known ratio $\frac{U_2}{U_1}$ - which was identified in section 5.2.1.3 - to find U_2, the ponderomotive potential at the other detector. Recalling the definition of U_p in equation (3.3),

$$U_p = \frac{e^2E_0^2}{4m_e\omega^2},$$

it is simple to use these calculated ponderomotive potentials to find the electric field amplitude

$$E_0 = \sqrt{\frac{4m_e\omega^2U_p}{e^2}}, \tag{5.30}$$

which is dependent on the degree of temporal overlap between the X-ray and streaking pulses.

Assume the streaking laser pulse has a Gaussian envelope E_0 with some r.m.s. duration σ_{IR}:

$$E_0(t_i) = E_{max}\exp\left[-\frac{(t_i - t_0)^2}{2\sigma_{IR}^2}\right] \tag{5.31}$$

$$\implies t_i = t_0 \pm \sqrt{-2\sigma_{IR}^2 \log\left(\frac{E_0(t)}{E_{max}}\right)}, \tag{5.32}$$

where E_{max} refers to the peak electric field amplitude occurring at the centre of the streaking pulse. Because of the $\pm$ sign in equation (5.32), it is not yet possible to determine whether a particular measurement overlapped with the early or late part of the streaking pulse - the Gaussian envelope is symmetric and there are two possible arrival times that correspond to any given amplitude. For simplicity, we will henceforth define the time axis such that $t_0 = 0$, and assume that $t_i \geq 0$.

The distribution of arrival times obtained from equation (5.32) is shown in the histogram in Figure 5.10. For these data, there are two assumptions needed to complete this calculation. Firstly, the streaking pulse duration was estimated to be 300 fs (FWHM) based on the typical OPA operation at the time of the experiment. Secondly, it was assumed that the single measurement out of all those in Figure 5.3 which experienced the largest streaking field amplitude was made exactly at the peak of the streaking pulse envelope, when $E(t) = E_{max}$. This is challenging to verify without improved streaking pulse diagnostics - we can only infer that that measurement was made with a larger streaking field amplitude than all the others, not necessarily that it was made with the maximum possible field amplitude, and it is also possible that that measurement appears to have experienced the largest amplitude due to experimental error. In future experiments, better laser diagnostics would render these assumptions unnecessary.

Another problem to consider is energy jitter in the XFEL pulse, because generally each X-ray pulse may have a slightly different photon energy. This means that the photoelectron emission peaks will not always be emitted with the same kinetic energy, essentially adding or subtracting a small amount from each measurement ΔE. Inspecting the central kinetic energy of the unstreaked photoemission peaks, as in section 4.3.2, shows that the energy jitter had a standard deviation of 1.6 eV. This is small compared to the total changes in kinetic energy measured in the experiment, and does not preclude calculations made using many averaged measurements such as those in sections 4.3 and 5.2.1, but even a small amount of energy jitter becomes significantly more impactful when dealing with individual measurements.

Future experiments must account for energy jitter in order to take full advantage of the precision afforded by SRAS. In the present experiment, the

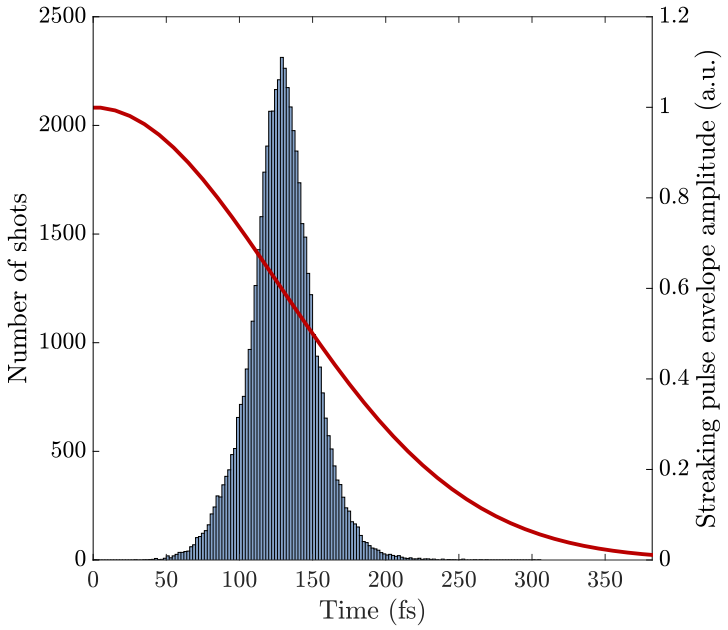

Figure 5.10: **Temporal overlap.** Histogram of the arrival times of the many individual measurements, assuming a streaking pulse with a FWHM duration of 300 fs and such that $t = 0$ corresponds to the photoemission perfectly overlapping with the peak of the streaking pulse envelope. The red line shows the Gaussian envelope of the streaking pulse.

streaked and unstreaked spectra were obtained with separate XFEL pulses. One way in which energy jitter could be corrected for is by measuring streaked and unstreaked spectra for *every* XFEL pulse. A third TOF and sample could be arranged far from the streaking laser focus to measure the streaking-field-free photoemission spectrum, which would reveal the photon energy of each XFEL pulse. The final kinetic energy of the streaked photoelectron peaks downstream could then be corrected by simply adding or subtracting the discrepancy in XFEL photon energy. Another option, depending on the experiment in question, might be to perform two-TOF SRAS using one or more Auger-Meitner emission peaks, whose initial kinetic energy is not dependent on the photon energy of the ionising light pulse.

In the present work, the lack of such metadata will limit our discussion to qualitative single-shot characteristics, but these diagnostic measurements

are simple to implement in the future, and only superficial barriers to full quantitative results remain. For a proof of concept and a glimpse into the future of SRAS, we will proceed using the aforementioned assumptions.

5.2.2.3 Mapping between measurements and parameters

With the relatively simple calculations in sections 5.2.2.1 and 5.2.2.2, we can now access the single-shot streaking parameters. Figure 5.11 displays the data from Figure 5.3 with the single-shot parameters indicated by colourmaps. Those shots arriving closer to the peak of the streaking pulse envelope experience a larger streaking vector potential, and a larger change in kinetic energy. The CEP varies across the ring, but is constant along spiral lines.

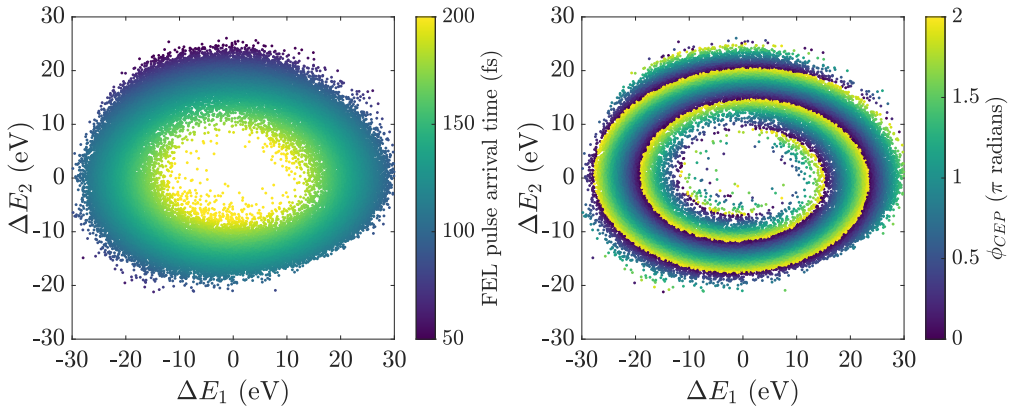

Figure 5.11: **Single-shot streaking parameters.** Data from the correlation plot in Figure 5.3 are reproduced, with a colourmap indicating the arrival time and CEP in the left and right panels respectively. The arrival time here refers to the magnitude of the delay between the centres of X-ray and MIR pulses.

The correlation plot gives us enough data to calculate a mapping between $(\Delta E_1, \Delta E_2)$ positions and time-phase parameter pairs. Indeed, we can apply this mapping to the rest of the parameter space, such that all incoming data can be converted to self-referenced coordinates. The three-dimensional surface in Figure 5.12 is a complete mapping between measured kinetic energy shifts and streaking parameters. For any given pair of measurements

$(\Delta E_1, \Delta E_2)$, we can use this surface to identify the pump-probe delay (the z-coordinate) and the streaking CEP ϕ_{CEP} (the colour of the surface).

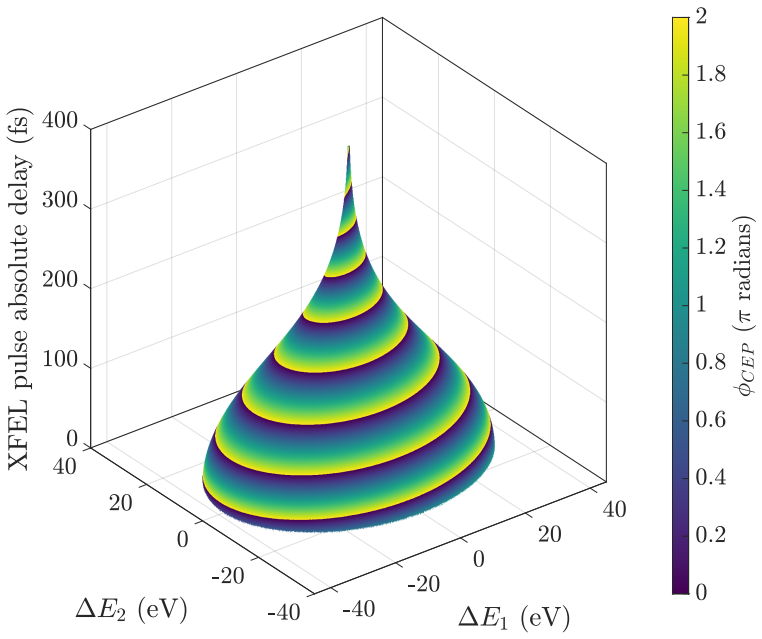

Figure 5.12: **Time-phase mapping surface.** For each pair of coordinates $(\Delta E_1, \Delta E_2)$, the X-ray pulse delay is shown by the vertical coordinate of the surface. There are two possible delays for each $(\Delta E_1, \Delta E_2)$ pair, because the streaking pulse envelope is symmetrical; the absolute values are shown here. The colour of the surface at each point corresponds, according to the colourmap, to the carrier-envelope phase ϕ_{CEP} for that combination of ΔE_1 and ΔE_2.

The shape of the surface in Figure 5.12 is determined by the streaking ratio $\sqrt{\frac{U_2}{U_1}}$ and the Gouy phase shift $\Delta\phi_G$ for this experiment, as well as the duration of the streaking pulse σ_{IR}. Once $\sqrt{\frac{U_2}{U_1}}$ and $\Delta\phi_G$ have been calculated using the methods discussed in section 5.2.1.3, this surface can be generated and used to map the timing and phase of every subsequent measurement. A future experiment could produce this mapping surface using the first ten thousand measurements, for example, and thereafter use it to

record the streaking conditions in real time for every incoming data point. Though such an experiment would not have control over those parameters, it would be able to study systems that typically demand this control, since measurements could be sorted and filtered as they were made. In all practical senses, self-referenced calculations can grant precise control over FEL pulse arrival time and streaking CEP.

5.2.2.4 Single-CEP spectrograms

Attosecond streaking experiments like the one discussed in Chapter 3 use a fixed carrier-envelope phase and vary the relative arrival time of the two pulses; SRAS experiments have control over neither of these parameters, but they can be calculated after the experiment based on their context in a correlation plot, as described in the preceding sections. It is possible, therefore, to select only the measurements made with a single CEP, sort them by arrival time, and produce a spectrogram comparable to Figure 3.7 from section 3.2.2.

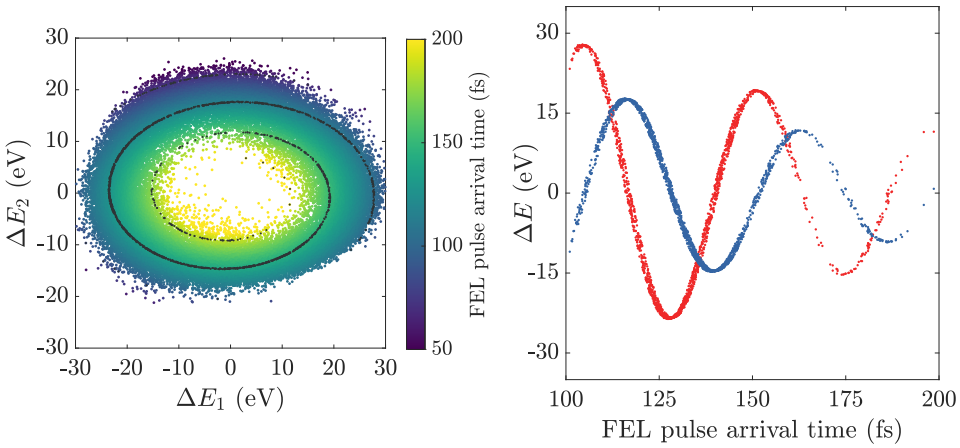

Figure 5.13: **Selection of shots with a single CEP.** The left-hand panel shows the data from Figure 5.3 with an overlaid colourmap corresponding to FEL pulse arrival time. The points highlighted in black are those for which the CEP is within 0.1 radians of π, which are the only measurements included in the other panel and in Figures 5.14 and 5.15. The right-hand panel shows these selected points' change in kinetic energy as a function of arrival time, with red and blue points corresponding to upstream and downstream detectors respectively.

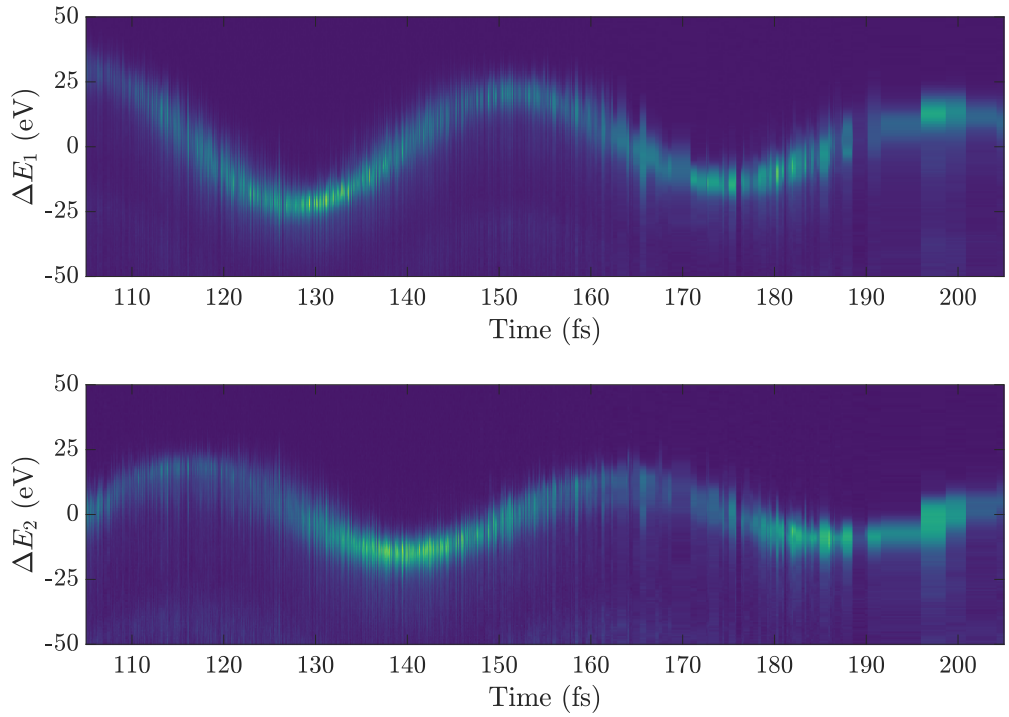

Figure 5.14: **Fixed-CEP SRAS spectrogram.** The full kinetic energy spectra of the points selected in Figure 5.13 are plotted and combined into a single-CEP spectrogram. The upper and lower panels correspond to upstream and downstream detectors respectively.

Figures 5.13 and 5.14 illustrate the process by which we can extract these spectrograms. Restricting our consideration to points within a narrow CEP range, the peak positions and even full raw spectra can be plotted as a function of arrival time. Not only is the oscillation of the streaking pulse's light field clearly visible, one can also see the sloping shape of the streaking pulse envelope. Unlike in Figure 3.7, the pump-probe delay steps are not - and cannot be - uniform. As we examine shots arriving further from the average arrival time, the data become more sparse, resulting in the wider bins towards the right of the spectrogram in Figure 5.14. Nevertheless, there are many measurements for which the XFEL pulse arrived with 105-160 fs delay with respect to the peak of the streaking pulse, which is a sufficiently wide range to encompass one full oscillation of the streaking laser field. Figure 5.15 shows the data within this range after averaging all spectra that fall within

1-fs bins, fixing the delay step size to produce a spectrogram comparable to those obtained in table-top attosecond streaking experiments without timing or phase jitter. Future experiments might use the tools and methods of section 3.2.2 with data processed in this way to make attosecond measurements at XFELs. If required, data could be collected over multiple cycles of the streaking field by either reducing the laser wavelength or increasing the range of the pump-probe delay. The latter could be achieved using a delay stage to adjust the path length of the streaking laser and gathering many measurements for each stage position. Due to timing jitter, each delay stage position can be used to make measurements with a range of pump-probe delays.

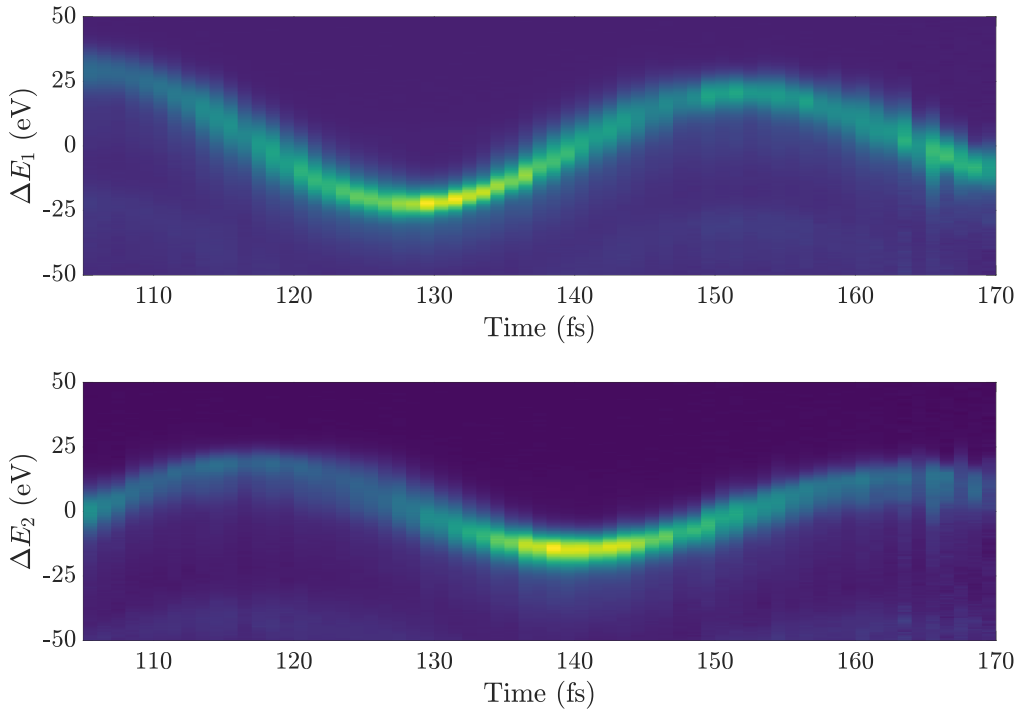

Figure 5.15: **Time-binned spectrogram.** Spectrograms similar to those shown in Figure 5.14, after additional smoothing by sorting the data into 1-femtosecond-wide bins and averaging the spectra within each bin.

Note that, as highlighted by the left-hand panel in Figure 5.13, each of these spectrograms uses only a fraction of the data in Figure 5.3: the shots within the selected CEP range. The full correlation plot contains enough data to produce many different spectrograms, each with a different CEP. This

makes two-TOF SRAS a fast and efficient method of collecting enough data to verify a measurement. The experiment described in Chapter 3 comprised around 50 spectrograms, each one taking around one hour to measure. The 50,000 shots in Figure 5.3 - enough to produce over a dozen spectrograms like those in Figures 5.14 and 5.15 - took only around 30 minutes to measure, potentially making two-TOF SRAS at least 20 times faster than table-top attosecond streaking. This is important in making the technique viable for XFEL experiments, which typically operate under strict time constraints.

5.3 Future opportunities

The two-TOF generalisation of self-referenced attosecond streaking spectroscopy holds tremendous potential for future time-resolved experiments at XFELs. The natural next step for the technique as a diagnostic tool may involve the construction of a permanent two-TOF SRAS setup on an XFEL beamline, where it might provide non-invasive X-ray and streaking pulse characterisation upstream of a variety of time-resolved experiments. This could lead to SRAS measurements of a wide range of ultrafast phenomena, with time resolution unhindered by jitter. For example, the technique might enable laser-driven electron dynamics in solid-state samples to be time-resolved at XFELs. It could also be used to make even more precise measurements of non-radiative decay processes such as Auger-Meitner decay, perhaps even reconstructing the temporal profile of emitted Auger-Meitner electrons. Coupled with the wider range of photon energies available to XFELs as compared to HHG sources, this type of apparatus might illuminate correlated electron dynamics that have hitherto been inaccessible.

Chapter 6

Summary and outlook

In the 21st century, XFELs have rapidly established themselves as cornerstones of ultrafast science. Across a multitude of disciplines, these remarkable devices have provided new insights into processes and structures on atomic time and length scales. The work presented in this thesis is intended to help cement the position of XFELs within and beyond attosecond science, bringing the study of subatomic systems and dynamics within reach.

Attosecond streaking spectroscopy has evolved in parallel with advances in XFEL technology, facilitating some of the most precise time-resolved experiments to date. The results presented in Chapter 3, and the other recent experiments discussed therein, illustrate how powerful this technique has become since its nascence just twenty years ago. And yet, XFELs' innate timing and phase jitter have largely prohibited their usage in attosecond streaking experiments, though substantial efforts have been made in recent years to improve XFEL pulse timing and characterisation. As demonstrated in Chapter 4, these obstacles are no longer insurmountable.

Self-referenced attosecond streaking provides a straightforward route to attosecond time resolution at XFELs and, using the relatively simple setup described in Chapter 5, can be applied to almost any system or phenomenon of interest. SRAS does not require significant adjustments to the experimental apparatus typical for streaking experiments, and can be used either for direct measurements or as a non-invasive diagnostic tool.

In its first demonstration, presented in Chapter 4, SRAS was used to measure the Auger-Meitner decay lifetime in neon, which was found to be 2.2 fs. Measuring the duration of such a short process would ordinarily be impossible given the 100-fs timing jitter between the pump and probe pulses

during this experiment. Not only did this experiment verify the viability of SRAS, it also showcased the necessity of a comprehensive theoretical model of Auger-Meitner decay in XFEL streaking experiments.

The latest experiments with SRAS, presented in Chapter 5, illustrate how far this technique can be taken. It is now possible to measure full spectrograms, each with a single carrier-envelope phase (Figures 5.14 and 5.15), equivalent to those acquired in table-top attosecond streaking experiments (Figure 3.7); these SRAS-enabled spectrograms could be used to measure attosecond dynamics via the retrieval procedures discussed in section 3.2.2.1. Equipped with these new methods, it is expected that the achievable time resolution in future XFEL SRAS experiments will be limited only by the available X-ray pulse durations, as is the case for table-top attosecond streaking.

Attoscience remains an exciting and rapidly-evolving field of research. With new and ever more advanced XFEL facilities on the horizon, the rapid progress in the field this century is sure to continue. Traditional attosecond streaking experiments such as the one described in Chapter 3 are likely to remain vital to attoscience. For the time being, it is still HHG sources that produce the shortest light pulses, ideal for measuring few-attosecond dynamics such as the photoelectric effect. XFELs and table-top systems will continue to complement each other as attoscience grows and matures.

Bibliography

1. Itatani, J. *et al.* Attosecond Streak Camera. *Physical Review Letters* **88.** https://doi.org/10.1103/physrevlett.88.173903 (Apr. 2002).
2. Drescher, M. *et al.* Time-resolved atomic inner-shell spectroscopy. *Nature* **419,** 803–807. https://doi.org/10.1038/nature01143 (Oct. 2002).
3. Remacle, F. & Levine, R. D. An electronic time scale in chemistry. *Proceedings of the National Academy of Sciences* **103,** 6793–6798. https://doi.org/10.1073/pnas.0601855103 (Apr. 2006).
4. Cavalieri, A. L. *et al.* Attosecond spectroscopy in condensed matter. *Nature* **449,** 1029–1032. https://doi.org/10.1038/nature06229 (Oct. 2007).
5. Ayvazyan, V. *et al.* First operation of a free-electron laser generating GW power radiation at 32 nm wavelength. *The European Physical Journal D* **37,** 297–303. https://doi.org/10.1140/epjd/e2005-00308-1 (Nov. 2005).
6. McNeil, B. W. J. & Thompson, N. R. X-ray free-electron lasers. *Nature Photonics* **4,** 814–821. https://doi.org/10.1038/nphoton.2010.239 (Nov. 2010).
7. Behrens, C. *Characterization and control of femtosecond electron and X-ray beams at free-electron lasers.* en. PhD thesis (2012), 2012, DESY Thesis (2012). doi:10.3204/DESY–THESIS. http://bib-pubdb1.desy.de/record/139966.
8. Schmüser, P., Dohlus, M., Rossbach, J. & Behrens, C. *Free-Electron Lasers in the Ultraviolet and X-Ray Regime* https://doi.org/10.1007/978-3-319-04081-3 (Springer International Publishing, 2014).

9. Bostedt, C. *et al.* Linac Coherent Light Source: The first five years. *Reviews of Modern Physics* **88.** https://doi.org/10.1103/revmodphys.88.015007 (Mar. 2016).

10. Mak, A. *et al.* Attosecond single-cycle undulator light: a review. *Reports on Progress in Physics* **82,** 025901. https://doi.org/10.1088/1361-6633/aafa35 (Jan. 2019).

11. Duris, J. *et al.* Tunable isolated attosecond X-ray pulses with gigawatt peak power from a free-electron laser. *Nature Photonics* **14,** 30–36. https://doi.org/10.1038/s41566-019-0549-5 (Dec. 2019).

12. Hargrove, L. E., Fork, R. L. & Pollack, M. A. LOCKING OF He–Ne LASER MODES INDUCED BY SYNCHRONOUS INTRACAVITY MODULATION. *Applied Physics Letters* **5,** 4–5. https://doi.org/10.1063/1.1754025 (July 1964).

13. DiDomenico, M. Small-Signal Analysis of Internal (Coupling-Type) Modulation of Lasers. *Journal of Applied Physics* **35,** 2870–2876. https://doi.org/10.1063/1.1713121 (Oct. 1964).

14. Yariv, A. Internal Modulation in Multimode Laser Oscillators. *Journal of Applied Physics* **36,** 388–391. https://doi.org/10.1063/1.1713999 (Feb. 1965).

15. Haus, H. Mode-locking of lasers. *IEEE Journal of Selected Topics in Quantum Electronics* **6,** 1173–1185. https://doi.org/10.1109/2944.902165 (Nov. 2000).

16. Zewail, A. H. Laser Femtochemistry. *Science* **242,** 1645–1653. https://doi.org/10.1126/science.242.4886.1645 (Dec. 1988).

17. Zewail, A. H. Femtochemistry. Past, present, and future. *Pure and Applied Chemistry* **72,** 2219–2231. https://doi.org/10.1351/pac200072122219 (Jan. 2000).

18. Corkum, P. B. & Krausz, F. Attosecond science. *Nature Physics* **3,** 381–387. https://doi.org/10.1038/nphys620 (June 2007).

19. Krausz, F. & Ivanov, M. Attosecond physics. *Reviews of Modern Physics* **81,** 163–234. https://doi.org/10.1103/revmodphys.81.163 (Feb. 2009).

20. Calegari, F., Sansone, G., Stagira, S., Vozzi, C. & Nisoli, M. Advances in attosecond science. *Journal of Physics B: Atomic, Molecular and Optical Physics* **49,** 062001. https://doi.org/10.1088/0953-4075/49/6/062001 (Feb. 2016).

21. Röntgen, W. C. On a New Kind of Rays. *Nature* **53,** 274–276. https://doi.org/10.1038/053274b0 (Jan. 1896).

22. Walker, S. M. *et al.* In Vivo Time-Resolved Microtomography Reveals the Mechanics of the Blowfly Flight Motor. *PLoS Biology* **12** (ed Hedenström, A.) e1001823. https://doi.org/10.1371/journal.pbio.1001823 (Mar. 2014).

23. Giacconi, R., Gursky, H., Paolini, F. R. & Rossi, B. B. Evidence for x Rays From Sources Outside the Solar System. *Physical Review Letters* **9,** 439–443. https://doi.org/10.1103/physrevlett.9.439 (Dec. 1962).

24. Abbe, E. Beiträge zur Theorie des Mikroskops und der mikroskopischen Wahrnehmung. *Archiv für Mikroskopische Anatomie* **9,** 413–468. https://doi.org/10.1007/bf02956173 (Dec. 1873).

25. Smyth, M. S. x Ray crystallography. *Molecular Pathology* **53,** 8–14. https://doi.org/10.1136/mp.53.1.8 (Feb. 2000).

26. Zheng, H. *et al.* X-ray crystallography over the past decade for novel drug discovery – where are we heading next? *Expert Opinion on Drug Discovery* **10,** 975–989. https://doi.org/10.1517/17460441.2015.1061991 (July 2015).

27. Clegg, W. The development and exploitation of synchrotron single-crystal diffraction for chemistry and materials. *Philosophical Transactions of the Royal Society A: Mathematical, Physical and Engineering Sciences* **377,** 20180239. https://doi.org/10.1098/rsta.2018.0239 (Apr. 2019).

28. Khan, S. in *Synchrotron Light Sources and Free-Electron Lasers* 51–81 (Springer International Publishing, 2016). https://doi.org/10.1007/978-3-319-14394-1_5.

29. Madey, J. M. J. Stimulated Emission of Bremsstrahlung in a Periodic Magnetic Field. *Journal of Applied Physics* **42,** 1906–1913. https://doi.org/10.1063/1.1660466 (Apr. 1971).

30. Elias, L. R., Fairbank, W. M., Madey, J. M. J., Schwettman, H. A. & Smith, T. I. Observation of Stimulated Emission of Radiation by Relativistic Electrons in a Spatially Periodic Transverse Magnetic Field. *Physical Review Letters* **36,** 717–720. https://doi.org/10.1103/physrevlett.36.717 (Mar. 1976).

31. Deacon, D. A. G. *et al.* First Operation of a Free-Electron Laser. *Physical Review Letters* **38,** 892–894. https://doi.org/10.1103/physrevlett.38.892 (Apr. 1977).

32. Emma, P. *et al.* First lasing and operation of an ångstrom-wavelength free-electron laser. *Nature Photonics* **4,** 641–647. https://doi.org/10.1038/nphoton.2010.176 (Aug. 2010).

33. Huang, Z. & Kim, K.-J. Review of x-ray free-electron laser theory. *Physical Review Special Topics - Accelerators and Beams* **10.** https://doi.org/10.1103/physrevstab.10.034801 (Mar. 2007).

34. Larmor, J. On the theory of the magnetic influence on spectra; and on the radiation from moving ions. *The London, Edinburgh, and Dublin Philosophical Magazine and Journal of Science* **44,** 503–512. https://doi.org/10.1080/14786449708621095 (Dec. 1897).

35. Saldin, E. L., Schneidmiller, E. A. & Yurkov, M. V. *The Physics of Free Electron Lasers* https://doi.org/10.1007/978-3-662-04066-9 (Springer Berlin Heidelberg, 2000).

36. Barletta, W. *et al.* Free electron lasers: Present status and future challenges. *Nuclear Instruments and Methods in Physics Research Section A: Accelerators, Spectrometers, Detectors and Associated Equipment* **618,** 69–96. https://doi.org/10.1016/j.nima.2010.02.274 (June 2010).

37. Bonifacio, R., Pellegrini, C. & Narducci, L. Collective instabilities and high-gain regime in a free electron laser. *Optics Communications* **50,** 373–378. https://doi.org/10.1016/0030-4018(84)90105-6 (July 1984).

38. Ackermann, W. *et al.* Operation of a free-electron laser from the extreme ultraviolet to the water window. *Nature Photonics* **1,** 336–342. https://doi.org/10.1038/nphoton.2007.76 (June 2007).

39. Ayvazyan, V. *et al.* Generation of GW Radiation Pulses from a VUV Free-Electron Laser Operating in the Femtosecond Regime. *Physical Review Letters* **88.** https://doi.org/10.1103/physrevlett.88.104802 (Feb. 2002).

40. Ayvazyan, V. *et al.* A new powerful source for coherent VUV radiation: Demonstration of exponential growth and saturation at the TTF free-electron laser. *The European Physical Journal D - Atomic, Molecular and Optical Physics* **20,** 149–156. https://doi.org/10.1140/epjd/e2002-00121-4 (July 2002).

41. Behrens, C. *et al.* Few-femtosecond time-resolved measurements of X-ray free-electron lasers. *Nature Communications* **5.** https://doi.org/10.1038/ncomms4762 (Apr. 2014).

42. Young, L. *et al.* Femtosecond electronic response of atoms to ultra-intense X-rays. *Nature* **466,** 56–61. https://doi.org/10.1038/nature09177 (July 2010).

43. Fang, L. *et al.* Double Core-Hole Production inN2: Beating the Auger Clock. *Physical Review Letters* **105.** https://doi.org/10.1103/physrevlett.105.083005 (Aug. 2010).

44. Cederbaum, L. S., Tarantelli, F., Sgamellotti, A. & Schirmer, J. On double vacancies in the core. *The Journal of Chemical Physics* **85,** 6513–6523. https://doi.org/10.1063/1.451432 (Dec. 1986).

45. Cederbaum, L. S., Tarantelli, F., Sgamellotti, A. & Schirmer, J. Double vacancies in the core of benzene. *The Journal of Chemical Physics* **86,** 2168–2175. https://doi.org/10.1063/1.452756 (Feb. 1987).

46. Santra, R., Kryzhevoi, N. V. & Cederbaum, L. S. X-Ray Two-Photon Photoelectron Spectroscopy: A Theoretical Study of Inner-Shell Spectra of the Organic Para-Aminophenol Molecule. *Physical Review Letters* **103.** https://doi.org/10.1103/physrevlett.103.013002 (July 2009).

47. Tashiro, M. *et al.* Molecular double core hole electron spectroscopy for chemical analysis. *The Journal of Chemical Physics* **132,** 184302. https://doi.org/10.1063/1.3408251 (May 2010).

48. Salén, P. *et al.* Experimental Verification of the Chemical Sensitivity of Two-Site Double Core-Hole States Formed by an X-Ray Free-Electron Laser. *Physical Review Letters* **108.** https://doi.org/10.1103/physrevlett.108.153003 (Apr. 2012).

49. Neutze, R., Wouts, R., van der Spoel, D., Weckert, E. & Hajdu, J. Potential for biomolecular imaging with femtosecond X-ray pulses. *Nature* **406,** 752–757. https://doi.org/10.1038/35021099 (Aug. 2000).

50. Hellmann, S. *et al.* Ultrafast Melting of a Charge-Density Wave in the Mott Insulator 1T-TaS_2. *Physical Review Letters* **105.** https://doi.org/10.1103/physrevlett.105.187401 (Oct. 2010).

51. Erk, B. *et al.* Imaging charge transfer in iodomethane upon x-ray photoabsorption. *Science* **345,** 288–291. https://doi.org/10.1126/science.1253607 (July 2014).

52. Düsterer, S. *et al.* Femtosecond x-ray pulse length characterization at the Linac Coherent Light Source free-electron laser. *New Journal of Physics* **13,** 093024. https://doi.org/10.1088/1367-2630/13/9/093024 (Sept. 2011).

53. Helml, W. *et al.* Measuring the temporal structure of few-femtosecond free-electron laser X-ray pulses directly in the time domain. *Nature Photonics* **8,** 950–957. https://doi.org/10.1038/nphoton.2014.278 (Nov. 2014).

54. Mottershead, C. T. A Tomographic Streak Camera for Ultrahigh-Speed Movies. *IEEE Transactions on Nuclear Science* **29,** 900–903. https://doi.org/10.1109/tns.1982.4335986 (1982).

55. Takahashi, A., Nishizawa, M., Inagaki, Y., Koishi, M. & Kinoshita, K. *New femtosecond streak camera* in *SPIE Proceedings* (ed Roehrenbeck, P. W.) (SPIE, Oct. 1993). https://doi.org/10.1117/12.161367.

56. Goulielmakis, E. *et al.* Direct Measurement of Light Waves. *Science* **305,** 1267–1269. https://doi.org/10.1126/science.1100866 (Aug. 2004).

57. Schultze, M. *et al.* Delay in Photoemission. *Science* **328,** 1658–1662. https://doi.org/10.1126/science.1189401 (June 2010).

58. Telle, H. *et al.* Carrier-envelope offset phase control: A novel concept for absolute optical frequency measurement and ultrashort pulse generation. *Applied Physics B* **69,** 327–332. https://doi.org/10.1007/s003400050813 (Oct. 1999).

59. Apolonski, A. *et al.* Controlling the Phase Evolution of Few-Cycle Light Pulses. *Physical Review Letters* **85,** 740–743. https://doi.org/10.1103/physrevlett.85.740 (July 2000).

60. Jones, D. J. *et al.* Carrier-Envelope Phase Control of Femtosecond Mode-Locked Lasers and Direct Optical Frequency Synthesis. *Science* **288,** 635–639. https://doi.org/10.1126/science.288.5466.635 (Apr. 2000).

61. Baltuška, A. *et al.* Attosecond control of electronic processes by intense light fields. *Nature* **421,** 611–615. https://doi.org/10.1038/nature01414 (Feb. 2003).

62. Paulus, G. G. *et al.* Measurement of the Phase of Few-Cycle Laser Pulses. *Physical Review Letters* **91.** https://doi.org/10.1103/physrevlett.91.253004 (Dec. 2003).

63. Corkum, P. B. Plasma perspective on strong field multiphoton ionization. *Physical Review Letters* **71,** 1994–1997. https://doi.org/10.1103/physrevlett.71.1994 (Sept. 1993).

64. Kojima, T. *et al.* 20-W ultraviolet-beam generation by fourth-harmonic generation of an all-solid-state laser. *Optics Letters* **25,** 58. https://doi.org/10.1364/ol.25.000058 (Jan. 2000).

65. Mu, X. *et al. High efficiency fourth-harmonic generation from nanosecond fiber master oscillator power amplifier* in *Nonlinear Frequency Generation and Conversion: Materials, Devices, and Applications XV* (eds Vodopyanov, K. L. & Schepler, K. L.) (SPIE, Mar. 2016). https://doi.org/10.1117/12.2208946.

66. Krause, J. L., Schafer, K. J. & Kulander, K. C. High-order harmonic generation from atoms and ions in the high intensity regime. *Physical Review Letters* **68,** 3535–3538. https://doi.org/10.1103/physrevlett.68.3535 (June 1992).

67. Neppl, S. *Attosecond Time-Resolved Photoemission from Surfaces and Interfaces.* en. PhD thesis (2012). https://mediatum.ub.tum.de/download/1093402/1093402.pdf.

68. Wiza, J. L. Microchannel plate detectors. *Nuclear Instruments and Methods* **162,** 587–601. https://doi.org/10.1016/0029-554x(79)90734-1 (June 1979).

69. Li, J. *et al.* Attosecond science based on high harmonic generation from gases and solids. *Nature Communications* **11.** https://doi.org/10.1038/s41467-020-16480-6 (June 2020).

70. Hui, D. *et al.* Attosecond electron motion control in dielectric. *Nature Photonics* **16,** 33–37. https://doi.org/10.1038/s41566-021-00918-4 (Dec. 2021).

71. Einstein, A. Über einen die Erzeugung und Verwandlung des Lichtes betreffenden heuristischen Gesichtspunkt. *Annalen der Physik* **322,** 132–148. https://doi.org/10.1002/andp.19053220607 (1905).

72. Ossiander, M. *Absolute Photoemission Timing* (Technische Universität München, 2018).

73. Parker, J. S., Doherty, B. J. S., Meharg, K. J. & Taylor, K. T. Time delay between singly and doubly ionizing wavepackets in laser-driven helium. *Journal of Physics B: Atomic, Molecular and Optical Physics* **36,** L393–L400. https://doi.org/10.1088/0953-4075/36/21/l04 (Oct. 2003).

74. Ossiander, M. *et al.* Attosecond correlation dynamics. *Nature Physics* **13,** 280–285. https://doi.org/10.1038/nphys3941 (Nov. 2016).

75. Eckle, P. *et al.* Attosecond angular streaking. *Nature Physics* **4,** 565–570. https://doi.org/10.1038/nphys982 (May 2008).

76. Eckle, P. *et al.* Attosecond Ionization and Tunneling Delay Time Measurements in Helium. *Science* **322,** 1525–1529. https://doi.org/10.1126/science.1163439 (Dec. 2008).

77. Pfeiffer, A. N. *et al.* Attoclock reveals natural coordinates of the laser-induced tunnelling current flow in atoms. *Nature Physics* **8,** 76–80. https://doi.org/10.1038/nphys2125 (Oct. 2011).

78. Klünder, K. *et al.* Probing Single-Photon Ionization on the Attosecond Time Scale. *Physical Review Letters* **106.** https://doi.org/10.1103/physrevlett.106.143002 (Apr. 2011).

79. Palatchi, C. *et al.* Atomic delay in helium, neon, argon and krypton. *Journal of Physics B: Atomic, Molecular and Optical Physics* **47,** 245003. https://doi.org/10.1088/0953-4075/47/24/245003 (Dec. 2014).

80. Isinger, M. *et al.* Photoionization in the time and frequency domain. *Science* **358,** 893–896. https://doi.org/10.1126/science.aao7043 (Nov. 2017).

81. Kheifets, A. S. & Ivanov, I. A. Delay in Atomic Photoionization. *Physical Review Letters* **105.** https://doi.org/10.1103/physrevlett.105.233002 (Dec. 2010).

82. Moore, L. R., Lysaght, M. A., Parker, J. S., van der Hart, H. W. & Taylor, K. T. Time delay between photoemission from the 2p and 2s subshells of neon. *Physical Review A* **84.** https://doi.org/10.1103/physreva.84.061404 (Dec. 2011).

83. Nagele, S., Pazourek, R., Feist, J. & Burgdörfer, J. Time shifts in photoemission from a fully correlated two-electron model system. *Physical Review A* **85.** https://doi.org/10.1103/physreva.85.033401 (Mar. 2012).

84. Kheifets, A. S. Time delay in valence-shell photoionization of noble-gas atoms. *Physical Review A* **87.** https://doi.org/10.1103/physreva.87.063404 (June 2013).

85. Feist, J. *et al.* Time delays for attosecond streaking in photoionization of neon. *Physical Review A* **89.** https://doi.org/10.1103/physreva.89.033417 (Mar. 2014).

86. Pazourek, R., Feist, J., Nagele, S. & Burgdörfer, J. Attosecond Streaking of Correlated Two-Electron Transitions in Helium. *Physical Review Letters* **108.** https://doi.org/10.1103/physrevlett.108.163001 (Apr. 2012).

87. Wuilleumier, F. & Krause, M. O. Photoionization of neon between 100 and 2000 eV: Single and multiple processes, angular distributions, and subshell cross sections. *Physical Review A* **10,** 242–258. https://doi.org/10.1103/physreva.10.242 (July 1974).

88. Strickland, D. & Mourou, G. Compression of amplified chirped optical pulses. *Optics Communications* **56,** 219–221. https://doi.org/10.1016/0030-4018(85)90120-8 (Dec. 1985).

89. Kerr, J. A new relation between electricity and light: Dielectrified media birefringent. *The London, Edinburgh, and Dublin Philosophical Magazine and Journal of Science* **50,** 337–348. https://doi.org/10.1080/14786447508641302 (Nov. 1875).

90. Kerr, J. A new relation between electricity and light: Dielectrified media birefringent (Second paper). *The London, Edinburgh, and Dublin Philosophical Magazine and Journal of Science* **50,** 446–458. https://doi.org/10.1080/14786447508641319 (Dec. 1875).

91. Shimizu, F. Frequency Broadening in Liquids by a Short Light Pulse. *Physical Review Letters* **19,** 1097–1100. https://doi.org/10.1103/physrevlett.19.1097 (Nov. 1967).

92. Alfano, R. R. & Shapiro, S. L. Observation of Self-Phase Modulation and Small-Scale Filaments in Crystals and Glasses. *Physical Review Letters* **24,** 592–594. https://doi.org/10.1103/physrevlett.24.592 (Mar. 1970).

93. Stolen, R. H. & Lin, C. Self-phase-modulation in silica optical fibers. *Physical Review A* **17,** 1448–1453. https://doi.org/10.1103/physreva.17.1448 (Apr. 1978).

94. Planas, S. A., Mansur, N. L. P., Cruz, C. H. B. & Fragnito, H. L. Spectral narrowing in the propagation of chirped pulses in single-mode fibers. *Optics Letters* **18,** 699. https://doi.org/10.1364/ol.18.000699 (May 1993).

95. Cavalieri, A. L. *et al.* Intense 1.5-cycle near infrared laser waveforms and their use for the generation of ultra-broadband soft-x-ray harmonic continua. *New Journal of Physics* **9,** 242–242. https://doi.org/10.1088/1367-2630/9/7/242 (July 2007).

96. Bajt, S. *et al. Multilayers for next-generation x-ray sources* in *SPIE Proceedings* (eds Juha, L., Sobierajski, R. H. & Wabnitz, H.) (SPIE, May 2007). https://doi.org/10.1117/12.724786.

97. Soufli, R., Bajt, S., Hudyma, R. & Taylor, J. in *EUV Lithography* 133–134 (SPIE). https://doi.org/10.1117/3.769214.ch4a.

98. Li, H. *et al.* Zr/Mg multilayer mirror for extreme ultraviolet application and its thermal stability. *Applied Physics Letters* **102,** 111103. https://doi.org/10.1063/1.4794399 (Mar. 2013).

99. Chen, J. *et al. Fabrication of a two-dimensional graded periodic Mo/Si multilayer mirror using magnetron sputtering technology* in *EUV and X-ray Optics: Synergy between Laboratory and Space VI* (eds Hudec, R. & Pina, L.) (SPIE, Apr. 2019). https://doi.org/10.1117/12.2520849.

100. Riemensberger, J. *Time-Frequency-Resolved Absolute Time Delay of the Photoelectric Effect* (Technische Universität München, 2018).

101. Wolkow, D. M. Über eine Klasse von Lösungen der Diracschen Gleichung. *Zeitschrift für Physik* **94,** 250–260. https://doi.org/10.1007/bf01331022 (Mar. 1935).

102. Haynes, D. C. *et al.* Clocking Auger electrons. *Nature Physics* **17,** 512–518. https://doi.org/10.1038/s41567-020-01111-0 (Jan. 2021).

103. Meitner, L. Über die Entstehung der ß-Strahl-Spektren radioaktiver Substanzen. *Zeitschrift für Physik* **9,** 131–144. https://doi.org/10.1007/bf01326962 (Dec. 1922).

104. Meitner, L. Über den Zusammenhang zwischen β- und γ-Strahlen. *Zeitschrift für Physik* **9,** 145–152. https://doi.org/10.1007/bf01326963 (Dec. 1922).

105. Auger, P. Sur les rayons β secondaires produits dans un gaz par des rayons X. *CR Acad. Sci.(F)* **177,** 169 (1923).

106. Mehlhorn, W. 70 years of Auger spectroscopy, a historical perspective. *Journal of Electron Spectroscopy and Related Phenomena* **93,** 1–15. https://doi.org/10.1016/s0368-2048(98)00153-4 (June 1998).

107. Carroll, T. X. *et al.* Carbon 1s photoelectron spectroscopy of CF4 and CO: Search for chemical effects on the carbon 1s hole-state lifetime. *The Journal of Chemical Physics* **116,** 10221–10228. https://doi.org/10.1063/1.1476933 (June 2002).

108. Coreno, M. *et al.* Measurement andab initiocalculation of the Ne photoabsorption spectrum in the region of theKedge. *Physical Review A* **59,** 2494–2497. https://doi.org/10.1103/physreva.59.2494 (Mar. 1999).

109. Jurvansuu, M., Kivimäki, A. & Aksela, S. Inherent lifetime widths of Ar2p-1, Kr3d-1, Xe3d-1, and Xe4d-1states. *Physical Review A* **64.** https://doi.org/10.1103/physreva.64.012502 (June 2001).

110. Krause, M. O. Atomic radiative and radiationless yields for K and L shells. *Journal of Physical and Chemical Reference Data* **8,** 307–327. https://doi.org/10.1063/1.555594 (Apr. 1979).

111. Schmidt, V. *Electron Spectrometry of Atoms using Synchrotron Radiation* https://doi.org/10.1017/cbo9780511524561 (Cambridge University Press, May 1997).

112. Kienberger, R. *et al.* Atomic transient recorder. *Nature* **427,** 817–821. https://doi.org/10.1038/nature02277 (Feb. 2004).

113. Goulielmakis, E. *et al.* Single-Cycle Nonlinear Optics. *Science* **320,** 1614–1617. https://doi.org/10.1126/science.1157846 (June 2008).

114. Hentschel, M. *et al.* Attosecond metrology. *Nature* **414,** 509–513. https://doi.org/10.1038/35107000 (Nov. 2001).

115. Ott, C. *et al.* Strong-Field Extreme-Ultraviolet Dressing of Atomic Double Excitation. *Physical Review Letters* **123.** https://doi.org/10.1103/physrevlett.123.163201 (Oct. 2019).

116. Rohringer, N. An atomic inner-shell laser pumped with an x-ray free-electron laser. *Journal of Physics: Conference Series* **194,** 012012. https://doi.org/10.1088/1742-6596/194/1/012012 (Nov. 2009).

117. Rohringer, N. *et al.* Atomic inner-shell X-ray laser at 1.46 nanometres pumped by an X-ray free-electron laser. *Nature* **481,** 488–491. https://doi.org/10.1038/nature10721 (Jan. 2012).

118. Yoneda, H. *et al.* Atomic inner-shell laser at 1.5-ångström wavelength pumped by an X-ray free-electron laser. *Nature* **524,** 446–449. https://doi.org/10.1038/nature14894 (Aug. 2015).

119. Uiberacker, M. *et al.* Attosecond real-time observation of electron tunnelling in atoms. *Nature* **446,** 627–632. https://doi.org/10.1038/nature05648 (Apr. 2007).

120. Uphues, T. *et al.* Ion-charge-state chronoscopy of cascaded atomic Auger decay. *New Journal of Physics* **10,** 025009. https://doi.org/10.1088/1367-2630/10/2/025009 (Feb. 2008).

121. Krikunova, M. *et al.* Time-resolved ion spectrometry on xenon with the jitter-compensated soft x-ray pulses of a free-electron laser. *New Journal of Physics* **11,** 123019. https://doi.org/10.1088/1367-2630/11/12/123019 (Dec. 2009).

122. Verhoef, A. J. *et al.* Time-and-energy-resolved measurement of Auger cascades following Kr 3d excitation by attosecond pulses. *New Journal of Physics* **13,** 113003. https://doi.org/10.1088/1367-2630/13/11/113003 (Nov. 2011).

123. Smirnova, O., Yakovlev, V. S. & Scrinzi, A. Quantum Coherence in the Time-Resolved Auger Measurement. *Physical Review Letters* **91.** https://doi.org/10.1103/physrevlett.91.253001 (Dec. 2003).

124. Kazansky, A. K., Sazhina, I. P. & Kabachnik, N. M. Time-dependent theory of Auger decay induced by ultra-short pulses in a strong laser field. *Journal of Physics B: Atomic, Molecular and Optical Physics* **42,** 245601. https://doi.org/10.1088/0953-4075/42/24/245601 (Dec. 2009).

125. Pahl, E., Meyer, H.-D. & Cederbaum, L. S. Competition between excitation and electronic decay of short-lived molecular states. *Zeitschrift für Physik D Atoms, Molecules and Clusters* **38,** 215–232. https://doi.org/10.1007/s004600050086 (Oct. 1996).

126. Pahl, E., Cederbaum, L. S., Meyer, H.-D. & Tarantelli, F. Controlled Interplay between Decay and Fragmentation in Resonant Auger Processes. *Physical Review Letters* **80,** 1865–1868. https://doi.org/10.1103/physrevlett.80.1865 (Mar. 1998).

127. Krause, M., Stevie, F., Lewis, L., Carlson, T. & Moddeman, W. Multiple excitation of neon by photon and electron impact. *Physics Letters A* **31,** 81–82. https://doi.org/10.1016/0375-9601(70)91039-x (Jan. 1970).

128. Frühling, U. *et al.* Single-shot terahertz-field-driven X-ray streak camera. *Nature Photonics* **3,** 523–528. https://doi.org/10.1038/nphoton.2009.160 (Aug. 2009).

129. Mazza, T. *et al.* Sensitivity of nonlinear photoionization to resonance substructure in collective excitation. *Nature Communications* **6.** https://doi.org/10.1038/ncomms7799 (Apr. 2015).

130. Svensson, S. *et al.* Lifetime Broadening and CI-Resonances Observed in ESCA. *Physica Scripta* **14,** 141–147. https://doi.org/10.1088/0031-8949/14/4/004 (Oct. 1976).

131. Southworth, S. H. *et al.* DoubleK-shell photoionization of neon. *Physical Review A* **67.** https://doi.org/10.1103/physreva.67.062712 (June 2003).

132. Cutler, J. N., Bancroft, G. M., Sutherland, D. G. & Tan, K. H. Chemical dependence of core-level linewidths and ligand-field splittings: High-resolution core-level photoelectron spectra of I 4dlevels. *Physical Review Letters* **67,** 1531–1534. https://doi.org/10.1103/physrevlett.67.1531 (Sept. 1991).

133. Gorobtsov, O. Y., Lorenz, U., Kabachnik, N. M. & Vartanyants, I. A. Theoretical study of electronic damage in single-particle imaging experiments at x-ray free-electron lasers for pulse durations from 0.1 to 10 fs. *Physical Review E* **91.** https://doi.org/10.1103/physreve.91.062712 (June 2015).

134. Kim, M.-S., Scharf, T., Rockstuhl, C. & Herzig, H. P. in *Progress in Optics* 115–197 (Elsevier, 2013). https://doi.org/10.1016/b978-0-444-62644-8.00003-0.

135. Boyd, R. W. Intuitive explanation of the phase anomaly of focused light beams. *Journal of the Optical Society of America* **70,** 877. https://doi.org/10.1364/josa.70.000877 (July 1980).

136. Hariharan, P. & Robinson, P. A. The gouy phase shift as a geometrical quantum effect. *Journal of Modern Optics* **43,** 219–221. https://doi.org/10.1080/09500349608232735 (Feb. 1996).

137. Feng, S. & Winful, H. G. Physical origin of the Gouy phase shift. *Optics Letters* **26,** 485. https://doi.org/10.1364/ol.26.000485 (Apr. 2001).

Acknowledgements

There are many people to whom I am indebted for enriching my work and life during this degree, and without whom this thesis would not exist in its present form. Of course, I must first thank my supervisor, Adrian, for this opportunity to work at the forefront of ultrafast science. Thank you for your patience, advice, and support, for everything you have taught me, and for ensuring our work is always the best it can be.

Chris, thanks for always being available to answer my questions and guide my programming efforts, and especially thank you for the invaluable advice and lessons on XFEL physics. Thank you, Rashmi, for easing my journey from mathematical physics into the cutting-edge of experimental physics, by patiently teaching me so much about the operation of the lab during the early years of my degree. Stefan, thank you for your support and expertise in our photoemission delay experiments - I look forward to the next surprising result! Matthias, I appreciate your unfailing alacrity to advise, discuss, and search through decade-old files to solve a problem. Many thanks, too, to Franz, for the ever friendly and prudent counsel as my co-advisor. Ivette, thank you for all your advice and help on writing my thesis and over the years. Robin, thanks for advising me on writing about XFELs, and for helping me translate my abstract into German. And I am grateful to everyone at CFEL for the discussions, chats, and congenial atmosphere that I remember from that distant pre-pandemic era. Julia, Charlotte, and Neda: thank you for running the IMPRS graduate school and making it such a welcoming experience.

I must thank Christoph, Andre, John, Markus, Albert, Wolfi, and all the other collaborators involved with our 2021 paper. Thank you all for your patience and continued effort to enable the publication of our work, and for making our beamtime such a memorable experience. And thanks to Nikolay and Andrey, not only for making the paper a success with your unmatched

theory expertise, but also for always making time to clarify things to me.

I am thankful to all five members of my doctoral commission, for giving your time to read and hear about my work. I hope you find this thesis interesting, and that you - and perhaps, I - will enjoy my defence!

It seems improbable that I would ever have ended up where I am now without each of the earlier stepping stones in my scientific career. I must therefore acknowledge Dongfang and the rest of the Kärtner group at CFEL, Nicholas and Neil at the Met Office, and Graeme at Diamond Light Source, all of whom welcomed me for different scientific summer jobs throughout my undergraduate degree. Thanks to Dr. Bowcock and Prof. Hughes, my erstwhile advisors at Durham University, for helping to guide me along my early steps into scientific research. And thanks to my first-year lab partner, whose name escapes me, for helping to make our simple X-ray diffraction experiment a success - and perhaps thus securing the rest of my career in photon science.

I doubt that any doctoral degree could be completed without the support and camaraderie of good friends, and I am lucky to have spent much of the past few years in the company of some great people. Kostja, Masha, Ivette, Stefan, Nina, Robin, Diksha, and Gayatri: thank you for the many enjoyable days and evenings spent together, for countless game nights, barbecues, picnics, and more. Thanks to Katja, Tae, Simon, Daniel, and Luisa, for the joy of creating music with you and for the lively discussions on jazz, blues, or whatever else we felt like playing. Pragya, thank you for all your support, for inspiring me to work through every step of this thesis, and for your company, which is always appreciated.

Finally, thanks to my parents for instilling in me the curiosity that motivates all of my work. To my sister Alex, thank you for being my oldest friend. I am always grateful to my family for their unwavering belief in me.

Eidesstattliche Versicherung / Declaration on oath

Hiermit versichere ich an Eides statt, die vorliegende Dissertationsschrift selbst verfasst und keine anderen als die angegebenen Hilfsmittel und Quellen benutzt zu haben.

Ich versichere, dass dieses gebundene Exemplar der Dissertation und das in elektronischer Form eingereichte Dissertationsexemplar (über den Docata-Upload) und das bei der Fakultät (zuständiges Studienbüro bzw. Promotionsbüro Physik) zur Archivierung eingereichte gedruckte gebundene Exemplar der Dissertationsschrift identisch sind.

Hamburg, 2023

Unterschrift des Doktoranden